DESIGN AND OPTIMISATION OF ULTRA-COMPACT, HIGH-RESOLUTION 3D X-RAY IMAGING SYSTEMS

Thesis submitted in accordance with the requirements of
the University of Liverpool for the degree of Doctor in Philosophy by

Thomas Primidis

August 2022

Contents

Illustrations

List of Figures

List of Tables

Notations

The following notations and abbreviations are found throughout this thesis:

DBT	Digital Breast Tomosynthesis
DT	Digital Tomosynthesis
CNT	Carbon Nanotube
CT	Computed Tomography
CXR	Chest X-ray
FPS	Flat Panel Source
HPC	High-Performance Computing
HU	Hounsfield Units
ICU	Intensive Care Unit
MC	Monte Carlo
MRI	Magnetic Resonance Imaging
NHS	National Health System
PCB	Printed Circuit Board
PET	Positron Emission Tomography
SID	Source to Image Distance
SPECT	Single Photon Emission Computed Tomography
SPR	Scatter-to-Primary Ratio

Preface

This thesis is primarily my own work. The sources of other materials are identifed.

Abstract

This thesis presents design and optimisation studies of novel 3D X-ray imaging systems using Monte Carlo simulations, computer programming and experiments. The imaging systems are made by Adaptix Ltd and are used for dental, veterinary and extremity 3D imaging as well as for 3D non-destructive testing.

Instead of a rotating X-ray tube, the imaging systems by Adaptix use a square, stationary, flat panel X-ray source array and a stationary flat panel detector. The X-ray source array is made of a silicon wafer with multiple cold-cathode electron field emitters etched on it in rows and columns. The emitters are activated individually, in a rapid and sequential manner, to send electron beams on a transmissive X-ray target. Due to the different positions of the emitters on the wafer, the respective electron beams arrive at different positions on the X-ray target so the produced X-ray cone beams originate from different points in space. Thus, the X-ray beams irradiate the stationary imaging detector from different projection angles and the end result is that 3D imaging is achieved without movements or rotations like with conventional X-ray tubes. The benefits of this technological novelty is the shorter image acquisition time and the fewer mechanical vibrations which ultimately improve image quality, patient throughput and their experience. Also, the flat panel source arrays are much smaller and lighter than conventional X-ray tubes which makes the Adaptix 3D imaging systems cheaper, truly portable and deployable on the desktop.

Adaptix systems generate 3D images using the method of digital tomosynthesis. Digital tomosynthesis is a method similar to computed tomography but requires far fewer 2D projections and over a shorter angular range. Therefore, a much lower patient dose is one more benefit gained with the Adaptix technology. The output of a digital tomosynthesis reconstruction is a stack of 2D images, parallel to the flat panel detector and distributed along its normal, offering depth resolution. Specifically, each image corresponds to a different depth in the patient and when tissues lie on that depth, they appear in focus on the respective image whereas tissues below or above that height are blurred out and disappear. Digital tomosynthesis has seen a recent spark of interest as a low dose alternative to CT and as a 3D but similar dose alternative to 2D radiography and it has also shown potential as a 4D modality. Literature is also gradually enriched with new studies that thoroughly characterise the performance of commercial and experimental tomosynthesis systems and reveal a promising future for this low dose 3D X-ray imaging modality.

This thesis comprises a detailed characterisation of the Adaptix digital tomosynthesis technology. The FLUKA and Geant4 Monte Carlo codes are used to study the performance of the imaging systems including X-ray source efficiency, beam quality, image quality and patient dose. Results from both codes are compared with each other and with experiments in order to benchmark the two codes between them and to validate the accuracy of the models. The Monte Carlo models are also compared to alternative versions that have higher levels of realism but also increased complexity and they are all found equally accurate. This proves that general purpose Monte Carlo codes can deliver accurate digital tomosynthesis simulations as they are without any explicitly added realism and complexity. The simulation frameworks developed in this thesis are among the first that have been used to study the 2D X-ray imaging capabilities and patient dose of such systems and are the first that further characterised them in detail in terms of 3D image quality. The results from the Monte Carlo simulations have accelerated the development of Adaptix's technology by providing insight that is either costly or impossible to get experimentally. This has highly boosted R&D efficiency at an early stage and at a reduced cost. Also, the end-to-end detailed simulation frameworks have laid the foundations for both industrial and academic research on an innovative technology that has the potential to replace X-ray tubes in many if not all their applications.

Furthermore, this thesis includes simulations of a concept, chest 3D X-ray imaging system. This system is a conceptual upgrade of the existing Adaptix machines at a higher input power, better suited for the larger and more attenuating human chest. The upgraded system is simulated with Monte Carlo methods based on the Monte Carlo models mentioned before. End-to-end chest tomosynthesis procedures are simulated using a single flat panel source array of the upgraded imaging system, a flat panel detector and a highly realistic virtual human phantom. This provides detailed insight of source efficiency, image quality and patient dose under different X-ray source array designs which would be impossible to achieve experimentally since the upgrade is still at a conceptual stage. The results show that an Adaptix chest tomosynthesis system could operate at a lower voltage than conventionally practiced and this would result in lower dose without sacrificing image quality. Also, the results suggest that patient dose is low enough to allow multiple flat panel sources on a single tomosynthesis device. This would improve the irradiation geometry and ultimately result in superior image quality. These results have strongly confirmed Adaptix's vision for a portable chest tomosynthesis system with multiple flat panel sources and the company is using the simulation framework to design their first chest tomosynthesis prototype.

Finally, this thesis introduces Ipioni, a Python application which has been developed to automatically design chest tomosynthesis prototypes with multiple flat panel sources given only limited input by the user. During the design process, Ipioni performs a parameter scan over a vast range of specifications such as number and size of panels, number of emitters and X-ray cone beam angle and finds those combinations that produce designs which are acceptable in terms of various criteria. These criteria

include total device size, total stray radiation, available space for patient positioning and available space for multiple flat panel sources. For each design, Ipioni also calculates irradiation geometry metrics such as the angular range of projections and the level of beam overlap which are used to identify those designs that can deliver the best image quality. The role of Ipioni is to rapidly shortlist candidate designs according to geometrical specifications for these designs to then be pipelined into more detailed but slow or expensive studies like Monte Carlo simulations and laboratory experiments. Two examples of the usefulness of Ipioni are demonstrated where it is used to inexpensively and rapidly scan across tens of thousands of potential system designs and identify a handful of high-performing ones that can then be used in Monte Carlo physics simulations and experiments to characterise them in detail. Ipioni is currently being used by Adaptix to identify potential design specifications for their chest tomosynthesis prototype and has accelerated the introduction of this new product in a simple and cost-effective way.

In conclusion, this thesis presents a comprehensive approach to the design and optimisation of a novel, compact and portable 3D X-ray imaging technology with medical imaging, veterinary imaging and non-destructive testing applications. This technology has the potential to replace X-ray tubes and is being used to deliver low dose and low cost 3D imaging through digital tomosynthesis, a modality which is currently thoroughly studied due to its potential to become an alternative to both 2D radiography and 3D CT on a number of applications. Thus, the multi-layered and detailed simulation framework developed in this thesis can act as the foundation for both industrial and academic research on a technology with demonstrated clinical benefits and a broad spectrum of applications. It is also expected to largely advance both early and mature stages of R&D and has already helped Adaptix optimise the prioritisation of time and resources, essentially shortening the time to commercialisation and bringing down device cost. Ultimately, the results of this thesis will help deliver affordable, low dose and truly portable 3D X-ray imaging solutions globally and will allow us to overcome many of the limitations of the more than a century old X-ray tube technology.

Acknowledgements

This work has been done in close collaboration with Adaptix Ltd. Dr. Gil Travish, co-founder of Adaptix, Dr. Steve Wells, vice president of technology of Adaptix and Prof. Keith Bowen, chief science advisor of Adaptix, have provided exceptional feedback and useful supervision during this project. Dr. Vadim Soloviev, software developer at Adaptix has developed the digital tomosynthesis reconstruction algorithms used extensively in this thesis. Dr. Aquila Mavalankar, principal systems scientist at Adaptix, has offered important feedback during the backlog prioritisation of Ipioni. Dr. Conrad Dirckx, director of product management at Adaptix and Mr. James Cameron, experimental physicist at Adaptix, have delivered the experiments included in this report. Dr. Eleftherios Skordis, former member of my research group, the QUASAR group, at the University of Liverpool, has guided me during the initial steep learning curve of Monte Carlo simulations. Prof. Carsten Welsch and Dr. Javier Resta López have been my academic supervisors, offering essential feedback on the planning and delivery of my project. I wish to thank all of them for their great contribution. I would also like to thank all the members of the QUASAR group for offering a stimulating environment in which to do science, the whole Adaptix team for the warm welcome in the company and also the people at the Cockcroft Institute for my training in accelerator science.

This work was performed on Barkla, part of the High-Performance Computing facilities at the University of Liverpool.

The project has been an industrial collaboration between the University of Liverpool and Adaptix Ltd. It was funded by the Accelerators for Security, Healthcare and Environment Centre for Doctoral Training by the United Kingdom Research and Innovation, Science and Technology Facilities Council with reference number ST/R002142/1.

Chapter 1

Introduction

X-ray radiation has been used to diagnose diseases for more than one hundred years. According to the National Health Service in England, more than 23 million scans [1] were taken between 2020 and 2021 with various X-ray imaging modalities in England alone. This number had been increasing from more than 26 million between 2012 and 2013 to a peak of almost 31 million between 2018 and 2019 and started to decline at the start of the COVID-19 pandemic between 2019 and 2020. These numbers include 2D, 3D and 4D X-ray imaging modalities with the radiation used being produced by either an externally irradiating machine such as an X-ray tube or by internally inserted X-ray emitting radiopharmaceuticals.

However, X-rays belong to the ionising region of the electromagnetic spectrum which means they can damage patient tissue and cause deterministic (skin burns) or stochastic effects (cancer). Therefore, doctors must justify their choice of diagnostic modality prior to referring a patient for a scan, following the principle of as-low-as-reasonably-achievable (ALARA), in order for the diagnosis to offer more benefits than it causes harm. As such, the characteristics of the various X-ray imaging modalities such as their dose and the diagnostic information they generate make them justifiable for different types of diseases and different kinds of patients. The cost to deliver a particular scan also affects the availability of different modalities in clinics, an important factor during comparison further to the imparted dose and the clinical information that is generated. Therefore, to understand the potential impact of the work presented in this thesis, it is important to first understand the basics of X-ray imaging, the different modalities in which it is available and how modalities compare to each other in terms of diagnostic information, dose and cost.

This thesis presents the design and optimisation of a medical diagnosis system that uses the imaging modality of digital tomosynthesis (DT). DT is a modality similar to computed tomography (CT), which offers 3D anatomical information by reconstructing a 3D representation of the patient with multiple 2D X-ray projections from different angles. DT has been around for decades and precedes CT but due to the higher image quality of CT [2] and practical issues with slow flat panel detector technology [3] necessary for DT, CT has been more popular in clinical practice. CT is the gold standard for

anatomical diagnosis using ionising radiation [4–7] and is also used to produce the patient data upon which radiation treatment plans are designed. [8] However, the much larger dose of CT compared to DT and improvements in flat panel detector technology has sparked interest in DT once again as either a low-dose alternative to CT [9,10] or even as a 3D alternative to 2D radiography [11] given that these two modalities have comparable patient dose. Furthermore, the emergence of cold-cathode electron field emitters has allowed the replacement of the large and heavy X-ray tube by laptop-sized X-ray source arrays. [12] Just like the transition from tube to flat screen TVs, this flat panel X-ray source technology has the potential to revolutionise all applications for which the X-ray tube has been the workhorse and this of course includes medical applications. The DT systems under investigation in this thesis are all made of such arrays, manufactured by the company Adaptix Ltd, [13] who have been the industrial partners of this PhD project.

DT and the rest of the modalities that will be compared below use an external X-ray source to irradiate the patient and are best fit to show patient anatomy rather than function. Modalities that are best fit for functional X-ray imaging such as Gamma Scans, Single Photon Emission Computed Tomography (SPECT) and Positron Emission Tomography (PET) will not be included in the comparison. Gamma Scans, SPECT and PET are nuclear imaging modalities that are performed with the use of radiopharmaceuticals which are inserted in the patient to monitor metabolic activity. [14–16] Also, hybrid modalities such as PET-CT, SPECT-CT or MR-CT will not be compared with DT and the use of a contrast agent will not be treated as a separate modality for the scope of this thesis. [14–16] In other words, DT will be compared to the most elemental version of the competing X-ray imaging modalities that use externally irradiating X-ray sources and a detector on the opposite side of the imaging subject that collects the radiation and creates an image. These modalities may also be referred to as X-ray projection imaging modalities. The terms X-ray imaging and X-ray projection imaging will be used interchangeably in this thesis.

So in what follows, DT and competing X-ray projection imaging modalities will be described, including the features that make them best fit for some patients and diseases and limit or even prohibit their use for some others. This will make clear the potential of DT as a complementary or alternative modality for different diseases and patients and it will highlight the many problems that could be solved after replacing X-ray tubes with cold-cathode, electron field emitters. Since the topic of this thesis is the design and optimisation of DT systems made of compact, cold-cathode emitter arrays, what follows will also determine the importance of the results that were extracted during this PhD project.

1.1 X-ray projection imaging modalities in clinical practice

1.1.1 Planar X-ray imaging

Planar X-ray imaging, also known as plain or 2D radiography, is the simplest and most commonly used X-ray imaging modality available today.[1] It requires a single X-ray tube and a planar imaging detector, spaced from a few cm to almost 2 m apart as shown in Figure 1.1 The patient is positioned between them and a single image is taken by firing the X-ray tube once. The attenuation of the X-ray beam in the patient causes spatial fluctuations in the radiation intensity that reaches the detector. Either film or digital (direct or indirect) detectors are used to record these fluctuations and produce a 2D projection image of the body.

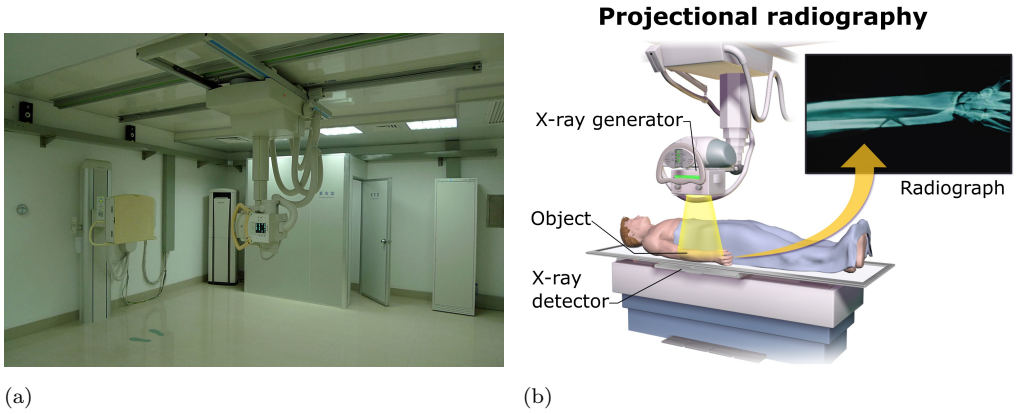

(a) (b)

FIGURE 1.1: a) X-ray room[1], b) Planar radiography components[2]

Hands and feet have different thickness, density and anatomy than the chest or the pelvis and the amount of radiation necessary to create informative images depends on what is being imaged. Thicker and denser parts of the body attenuate the X-ray beam more therefore longer irradiations are needed for enough radiation to pass through them, reach the detector and produce clinically useful images. X-ray beam penetration also depends on the energy spectrum, with lower energies being attenuated faster than higher energies. Therefore, for thicker and denser body parts, higher energies may be used in combination with a longer irradiation time and this applies to all the imaging modalities that will be mentioned later.

Planar X-ray radiography is the workhorse of diagnostic imaging.[1] However, as the name suggests, the images produced are in 2D, showing the tissues overlapped along the beam direction. Therefore, depth information is not available and an experienced radiologist is necessary to infer 3D information from a 2D image. Due to this, diseases that are expressed by either very small or very complex 3D anatomical structures

[1] X-ray room by marco bono is licensed with CC BY-NC-SA 2.0.
[2] Projectional radiography components by Blausen Medical Annotations by Mikael Häggström is licensed with CC BY-SA 4.0.

such as lung nodules and small bone fractures, might be difficult to observe with planar X-ray imaging and have to be diagnosed with more advanced modalities such as CT.[4,17] The same challenges are faced with interventional procedures such as image guided surgeries, removal of ingested foreign objects that can be hidden in 2D and catheterisations or intubations where lack of depth information could lead to a fatally misplaced instrument.[18–20] Visual examples of such limitations of 2D radiography are shown in Figure 1.2 where the position of a tube and anatomical details of the lung are easily identified in the slices from the 3D modality of digital tomosynthesis (described in Section 1.1.4) but are shown overlapping, much less clearly and sometimes not at all in the 2D image.

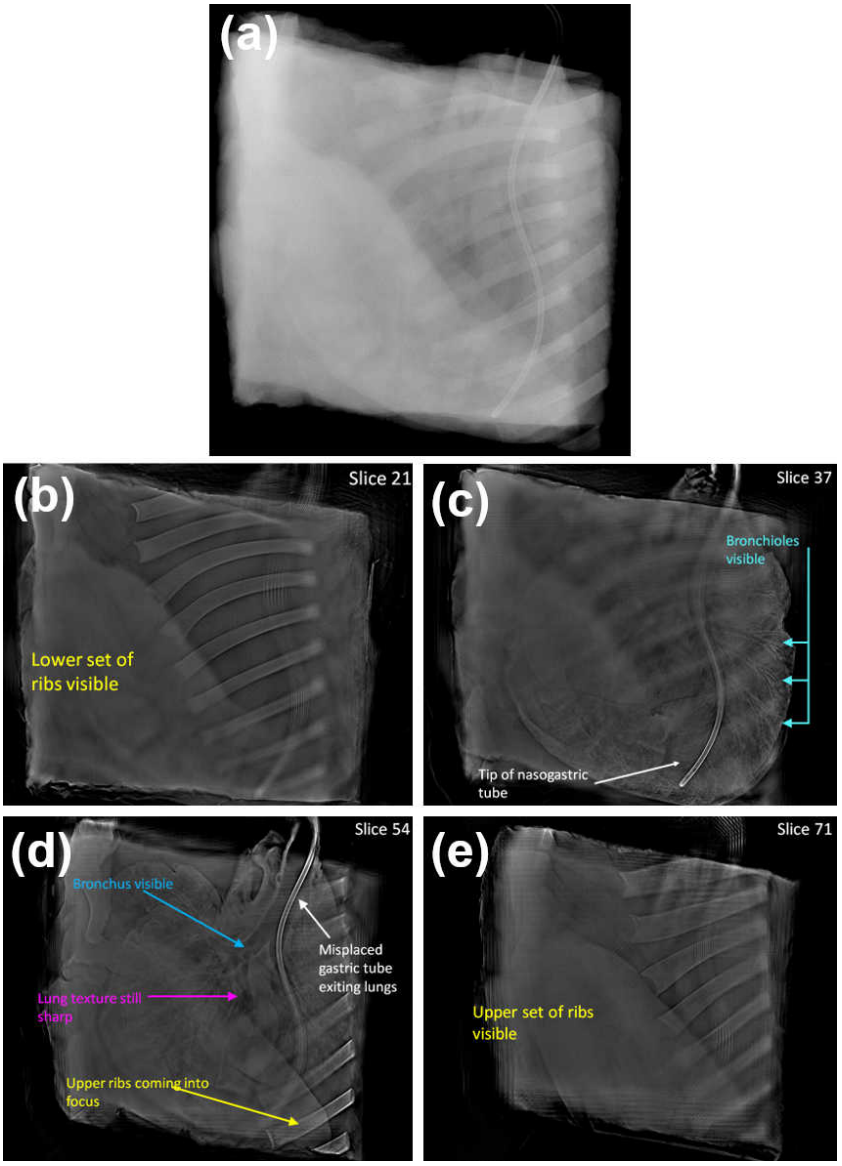

FIGURE 1.2: Images of an intubated chest phantom showing the limited information provided by 2D radiography due to the overlapping tissues (a) versus digital tomosynthesis that offers depth information with its 3D reconstruction of the patient (b-e). See also Figure 2.2. Reproduced with permission from Adaptix Ltd.

Movable 2D X-ray devices have existed since the 1930s[21] and they are frequently used in intensive care units (ICU).[11] However, the inherently large size and weight of the X-ray tube and the voluminous batteries required make these devices large and nearly half a ton heavy.[22–24] Therefore, even if they can be brought to the patient's bedside, this can only happen if they are pushed and pulled on smooth surfaces whereas transporting the device to a patient on a different floor cannot be done without an available escalator. Recently, devices with carbon nanotube (CNT) X-ray sources were made commercially available[25,26] with a source head weight of only 7 kg instead of nearly 75 kg of heads with conventional X-ray tubes.[23] However, this decrease in weight is small compared to the nearly half a ton overall weight of the systems and the same applies to their total size. As such, the use and portability of these new devices is naturally still bound by the same size and weight issues.

1.1.2 Fluoroscopy

Fluoroscopy is an imaging modality where 2D X-ray images are generated continuously, creating a 2D animation of the body, a contrast agent or of a medical instrument inserted into the patient. Fluoroscopy systems comprise an X-ray tube coupled with an imaging detector and a projection monitor. The patient is positioned between the X-ray source and the detector and the X-ray animation is projected on the monitor.

Fluoroscopy is commonly used during procedures that require continuous monitoring of the tissues or of medical equipment within the body such as gastrointestinal examinations, orthopaedic surgery, angiograms, placement of devices in the body or catheterisation.[14–16] As such, fluoroscopy is a lengthy examination and could cause increased patient and staff dose when the monitored procedure is long. This increases cancer risk and can cause deterministic radiation effects such as skin damage. Therefore, the photon flux rate of fluoroscopy systems must be reduced compared to non-animated modalities, inherently limiting the image contrast of the modality. Thus fluoroscopy is usually used with administered contrast agents or when high-contrast medical and surgical equipment is imaged inside the patient.[18,22,27,28]

Fluoroscopy devices can come in portable versions but still suffer from a large footprint and heavy weight,[22] restricting their flexibility to move across different floors and non-smooth surfaces. Representative examples of a fluoroscopy room, a fluoroscopy image and of damaged skin from long exposure are shown in Figure 1.3.

(a)

(b)

(c)

FIGURE 1.3: a) Fluoroscopy room with the operating theatre in the background including the patient bed and the fluoroscopy machine and the control room on the foreground[3], b) Example of a fluoroscopy image used to guide and assess the implantation of surgical equipment[4], c) Damaged skin due to long radiation exposure from fluoroscopy.[5]

1.1.3 Computed tomography

CT is an imaging modality where multiple X-ray images are taken from different projection angles and are then reconstructed into a 3D volume. [14–16] The different projections are taken with the X-ray tube rotating around the patient, performing either a single or multiple full rotations, and with a detector module diametrically opposite to the X-ray source that collects the photon beam and creates the X-ray projection images. CT offers the highest image quality among diagnostic modalities with ionising radiation. For that

[3] Fluoroscopy room with control space by Mikael Häggström, M.D. Reusing images is marked under CC0 1.0.

[4] Fluoroscopy by Yarkob is licensed with CC BY-SA 3.0.

[5] Fluoroscopy burn by LK Wagner, PhD; Vlietstra et al is licensed with CC BY-SA 3.0.

reason, the reconstructed 3D volumes are also used for radiation therapy and brachytherapy treatment planning. However, the large number of scans required to reconstruct the patient volume comes at the cost of increased dose, hindering or even prohibiting CT from being used frequently such as for screening or for regular monitoring of chronic diseases. Also, due to the large size of X-ray tubes, CT systems can accommodate just one or occasionally two X-ray tubes before cost, size and weight become excessive. Also, moving a large and power-hungry X-ray source during imaging can cause source-detector misalignments and vibrations that must be compensated for with additional corrective methods, increasing the cost of purchase and maintenance of CT systems. This limits their use to dedicated radiology rooms and larger hospitals that can accommodate their size and afford their one-off and recurring costs.

Portable CT devices exist such as cone beam CT scanners mounted on portable bases[22] but these are nevertheless large and heavy. They can be pushed and pulled usually by a single person but only on smooth surfaces and a change of hospital floor would require an escalator like when transporting the patient. Moreover, there is the technology of CT-on-rails, where a CT gantry is mounted on a sliding platform on rails so that scanning can be performed interchangeably with other operations like brachytherapy[29] or external beam radiotherapy.[30] The benefit of this technology is that instead of the patient, it is the CT machine that is moved between the different stages of an operation (initial positioning and treatment planning, pre-treatment image verification, treatment, post-treatment imaging). Moving the CT and the therapy machines instead of the patient maintains the patient's position throughout these different stages and avoids any problems with other equipment that might be connected to the patient and must be transported along with them. However, CT on rails is limited by the pre-laid tracks that do not span more than a few metres, making them just a little more flexible than but not a portable competitor to conventional CT scanners. Figure 1.4 includes examples of typical CT scanners as well as an example of an axial CT slice from a patient with respiratory illness.

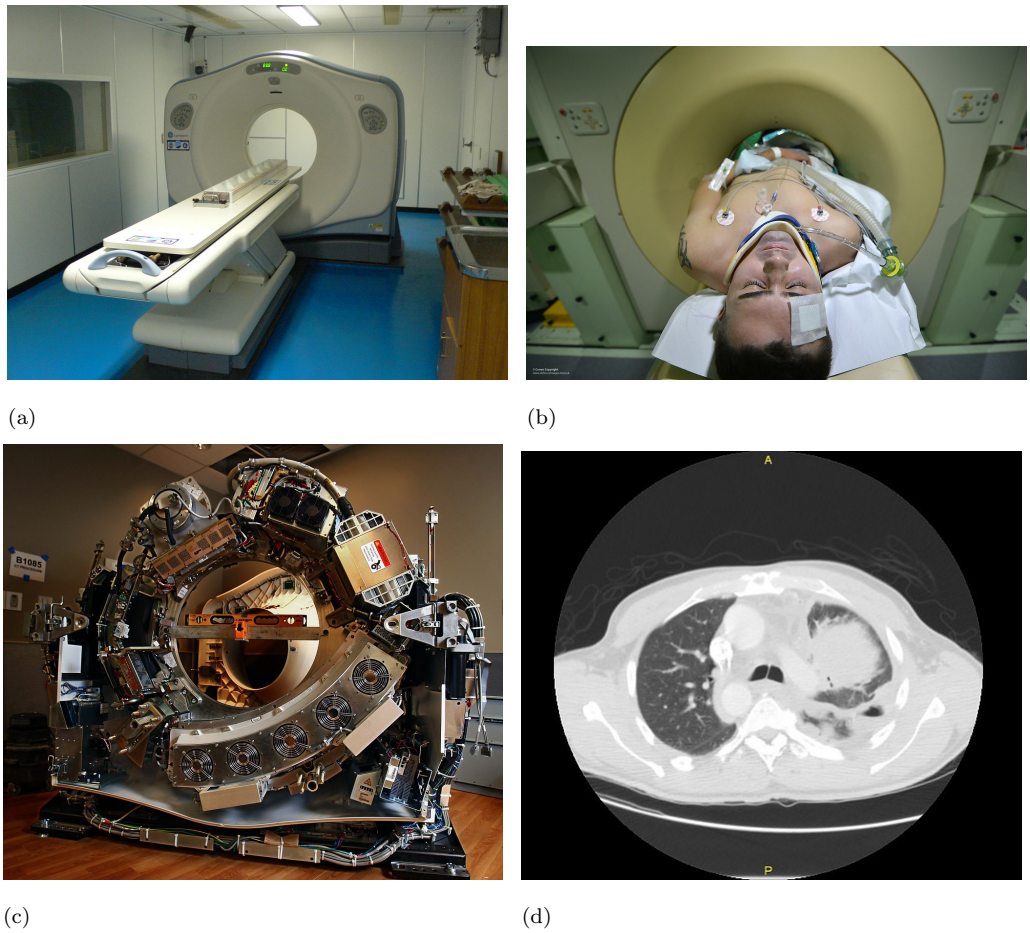

(a) (b)

(c) (d)

FIGURE 1.4: a) A typical CT scanner inside the radiology room[6], b) A patient inside the bore of a CT scanner being prepared for a scan[7], c) CT scanner exposed showing the detector array on the bottom right and the X-ray tube diametrically opposite[8], d) axial CT slice showing opacities in the lungs as a result of pulmonary disease.[9]

1.1.4 Digital tomosynthesis

Digital tomosynthesis (DT) is an imaging modality similar to CT but where fewer images are taken and from a narrower angular range [14,16] as shown in Figure 1.5. The reconstructed volume is presented as an image stack, with the images being parallel to the imaging detector and corresponding to different depths in the patient. Tissues come in focus in an image when they lie at its respective depth in the patient and they are blurred out and disappear otherwise, as shown in Figure 1.2 and Figure 1.6.

[6] X-ray CT scanner by kayakaya is licenced with CC BY-SA 2.0.

[7] RAFPatient Being Prepared for Analysis in a CT Scanner Personnel Returning from Afghanistan by Defence Images is licensed with CC BY-NC 2.0.

[8] scanner by walt74 is licensed with CC BY-NC-SA 2.0.

[9] Adenocarcinoma; vascular invasion demonstrated by immunostains - CT - Case 295 by Pulmonary Pathology is licensed with CC BY-SA 2.0.

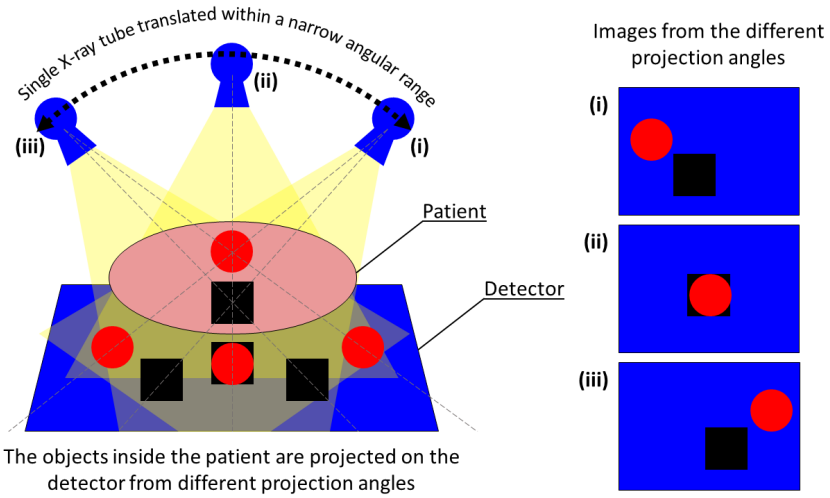

(a)

(b)

FIGURE 1.5: a) The Digital Tomosynthesis principle comprises a narrower angular range than CT, a detector that could be stationary or move in conjunction with the source which results in different projections of the patient on it. Reconstruction of these projections produces a 3D stack of images. b) Hologic Selenia Dimensions digital breast tomosynthesis system with its detector on the bottom, the movable X-ray tube on the top and a breast compression module in the middle.[31] (b) reproduced with permission from John Wiley and Sons.

Because a limited angular range of projections captures less information than a full rotation, the DT reconstruction is an ill-posed inverse problem. Therefore, the reconstructed volume contains less information than CT and this is mainly expressed

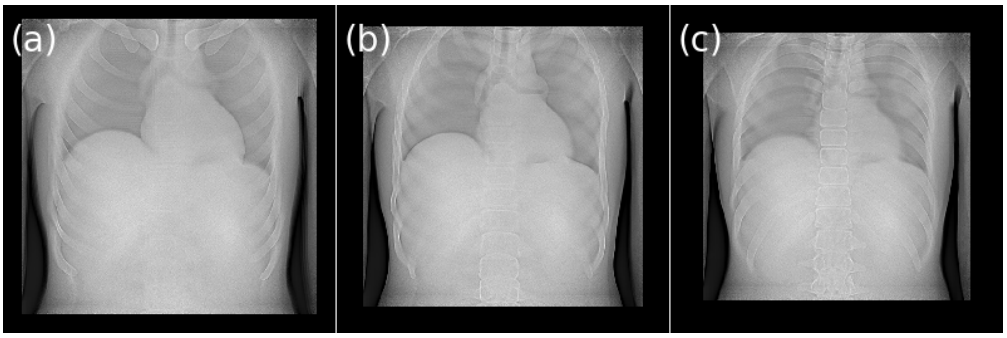

FIGURE 1.6: In DT, the reconstructed images correspond to different depths in the patient and bring in focus the organs that correspond to their depth while blurring out the rest. In these DT images of a human chest, the organs in focus are a) clavicle, b) trachea, c) spine. Figure adapted from results presented in Chapter 5. See also Figure 1.2.

as the residual shadow artefacts in each DT plane from tissues that lie away from that plane.[32] These shadow artefacts overlap with the in-focus tissues, essentially lowering the image quality. However, the limited angular range also comes with fewer projections and that decreases the patient dose while still offering 3D imaging.[33] Nevertheless, CT remains the gold standard for anatomical 3D X-ray imaging[4–7] and DT so far has been adopted mostly as a better alternative to digital mammography through the modality of digital breast tomosynthesis (DBT)[34] although there is a plethora of other applications.[3] A detailed account of DT is given in the next section.

1.2 Current status of digital tomosynthesis

DT provides better images than planar radiography but with comparable dose and also offers 3D information at a lower dose and lower cost than CT.[35] However, the large size of the X-ray tube still means that DT systems require mechanisms to control high temperatures, vibrations and misalignments of the source during the scan. Also, physically moving an X-ray tube can take several seconds[36] which causes problems to patients that have trouble holding their breath.

Regarding clinical workflow, currently available 3D X-ray imaging systems, including DT systems, necessitate patient transportation to the radiology room instead of offering the ability to bring the imaging system to the patient's bedside. Patient transportation poses risks for everyone in the clinic, especially when the patient is contagious or connected to life support equipment. Patient transportation also occupies several staff and increases traffic in hospital aisles and escalators. Thus, portable DT, with machines that could be brought to the patient's bedside could avoid all these issues, improving clinical workflow, patient throughput and making hospitals safer for staff and patients. Taking into account the comparable dose of DT and 2D radiography, bedside DT could also offer improved image quality in ICUs where bedside planar X-ray imaging is quite a common practice. Actually, in a relatively recent study, bedside DT was shown to be better than conventional bedside planar radiography in detecting pneumothorax.[11]

However, this was an experimental proof of concept and bedside DT was in general limited to experimental stages [37] until Adaptix demonstrated portable DT in veterinary clinics. [13] Therefore, the potential of such a portable novelty has been clearly proven and the study and optimisation of the Adaptix technology forms part of this PhD thesis.

From a technical point of view, the X-ray tube and the imaging detector in conventional DT are independent from each other so their alignment is necessary for each projection [37] and precision is not guaranteed. That is because the X-ray tube is rotated and translated accordingly to maintain the X-ray field within the imaging detector limits and this alignment could suffer both systematic and random failures. It is also worth noting that some systems have dynamic apertures that adjust the size of the X-ray field to further tailor it to the patient and the detector for each projection angle [38] but on the other hand increasing the complexity of the rotation, alignment and irradiation process. Stationary source array solutions could thus avoid many engineering and image quality challenges, simplifying manufacturing, driving down cost and offering a faster modality with no mechanical movements and larger patient throughput.

From an operational point of view, DT uses a large space between patient and X-ray source which could be 1-2 metres. This is a remnant from practices in planar radiography [38] where large source to image distances (SID)s are used to reduce magnification effects. Most if not all currently available DT systems are meant to be used for 2D radiography as well as for DT therefore the large SID is still being used. However, large SIDs come at the cost of increased (to the power of 2) necessary input power. Also, heating, cooling and rotating mechanisms for the X-ray tube contribute to the total power footprint, which means current DT systems require a separate high-power generator. This constraints mobile imaging solutions because it makes DT systems demanding in terms of space, weight and input power [22–24] and subsequently cost. Imaging systems exist where the electron emission is done with cold-cathode field emitters made of CNTs that do not require large input power like a thermionic X-ray tube does. [25,39,40] This allows the X-ray source head to be more compact and about ten times lighter [23] but it appears that apart from a dental CNT DT system that has seen clinical applications, [41] CNT DT systems remain experimental. [39,40]

From a physics point of view, the energies used in DT also appear to be a remnant of practices in planar radiography. For example, voltages higher than 100 kV in chest radiography are used to overcome the self-attenuation of the X-ray beam inside the source so that enough flux is produced to pass through the patient's chest. Also, as mentioned before, some planar radiography systems are built to also perform DT so maintaining the same practices in DT is quite natural. However, a recent study showed that in chest DT, 90 kV and 120 kV of a clinically available system produce similar 3D images when the effective dose is kept constant at 0.12 mSv. [42] Also, as it will be shown in Chapter 5, image quality between these two voltages remains the same even for the same output flux which results in 14% effective dose reduction with 90 kV. [43] Also, the observed 28%-50% drop in efficiency due to larger self-attenuation inside the 90 kV

source, could be offset by a shorter SID if the system is tailor made for DT. Therefore, there could be cost, manufacturing and clinical benefits in reducing the accelerating voltage of the X-ray source.

In-plane image resolution of DT is superior to CT. 500 μm pixels are a standard in-slice resolution for CT systems while there are DT machines offering 200 μm in-plane resolution.[44,45] There are also flat panel detectors with even smaller pixels at 160 μm[46] that could be integrated into DT systems and there has been experimental stationary DT with 160 μm detectors.[40] On the other hand, the depth resolution of DT is inferior to CT but can be improved by widening the angular range of the projections. This might come at a cost of reduced contrast if the effective dose is kept constant or at a cost of higher effective dose if contrast is maintained.[47] Nevertheless, in one clinical study, at a fraction of a CT dose, chest DT was able to find 92% of pulmonary nodules that were later confirmed by CT[9] and in another, chest DT avoided the need for CT in 76% of patients with suspected pulmonary nodules from doubtful chest X-ray (CXR) findings.[10] Furthermore, DT suffers less than CT from metal artefacts, an important improvement in post-operative imaging of patients with metallic prosthesis and osteosynthesis materials.[48] However, DT is more prone to motion artefacts.[35]

Moreover, all the clinically available DT systems today have one X-ray source that is rotated around the patient. Recently, novel systems were developed that instead of using a single X-ray tube, they used a linear array of CNT field emitters[25,39,40] where the different positions of the moving X-ray source were emulated by the fixed positions of the multiple X-ray sources on the array. The lateral offset of the CNTs and their sequential electronic firing, produces X-ray beams from different projection angles, thus allowing DT imaging without physical source movements. But apart from a dental system that has seen clinical applications,[41] the rest of the imaging systems remain experimental.[39,40] Also, it is worth noting that having a planar emitter distribution instead of a linear array, improves depth resolution[32] and such a technology is studied in this PhD thesis.

From a financial point of view, the cost to deliver a non-contrast material-enhanced chest CT examination in the United States was found to be about 10-15 times that of a 2D X-ray scan and in Korea the same price ratio was found with CT and 2D scans costing \$200 and \$10-\$20 respectively. On the other hand, chest DT scans cost 1.5-3 times as much as 2D scans at \$30. A similar cost ratio was also seen in Sweden.[35]

In terms of observer performance in evaluating DT images, in a study that included 160 chest DT scans, the average time to report the DT images was about twice as long as the time required to report 2D X-rays, at 134 s and 64 s respectively.[49] In another study with 50 consecutive thoracic spine radiography and DT data sets from elderly patients with vertebral fractures, the four observers reported a longer perceived time for DT evaluation but nevertheless clearly preferred it over radiography.[50] Various degrees of preference of DT over 2D have been expressed in other studies[51,52] whereas the opposite has also been reported for detecting microcalcifications in the breast,[51,53]

indicating a preference that depends on diagnostic objective. Finally, inter- and intra-observer agreement tends to be stronger with DT than with 2D images.[7,54–58]

1.3 Background summary and thesis structure

From what has been mentioned so far, DT appears to have the potential to replace planar radiography as an entry or screening modality thanks to the superior image quality with a comparable dose, or to replace CT as a low-dose and low-cost alternative for a proportion of cases requiring 3D imaging. But until recently, the X-ray source technology was limited by the large size of the X-ray tube and despite some novelty with compact X-ray sources made of CNTs, truly mobile DT systems with non-rotating sources were not clinically available.

However, Adaptix, which has been an industrial partner during this PhD project, took a ground breaking step forward by demonstrating veterinary DT imaging in the clinic with a portable device the size of a personal computer that instead of a movable X-ray source used a fixed square flat-panel source (FPS) array of cold-cathode field emitters.[13] The company has developed arrays of individually addressable X-ray sources that produce X-rays without the need to heat a filament[12] and this has been achieved by leveraging the high electric field gradient that exists around micrometre-sized metallic peaks (the field emitters) which is enough to release electrons at room temperature.

Adaptix has coupled their novel FPS arrays with flat panel imaging detectors to build ultra-compact, portable DT imaging systems. The source array and the detector are fixed relative to each other and different X-ray projections are taken with a rapid sequential electronic activation of the sources without any mechanical movements. The different positions of the sources on the array offer the different projection angles necessary for DT. Also, the planar distribution of X-ray sources offers improved DT depth resolution compared to a linear source array[32] and Adaptix has used their technology to build a line of portable DT devices for applications in orthopaedic, dental, veterinary, NDT and chest DT imaging[13,43].

This thesis contains a description of the Adaptix DT technology and the development of detailed Monte Carlo simulation frameworks that are used to study and optimise all of the Adaptix 3D X-ray imaging systems. In Chapter 2 the characteristics of these systems are given and in Chapter 3 FLUKA[59] and Geant4[60] Monte Carlo simulation frameworks are developed and validated with experiments. These Monte Carlo models are used as virtual twins of the true devices in order to computationally investigate performance details and upgrades that are either expensive or impossible to investigate experimentally. Also, the use of two fundamentally different Monte Carlo codes in line with the experimental validation adds multiple layers of confidence in the virtual twins since, as it is shown later, there is a great level of agreement between the codes themselves and between the codes and the experiments. In Chapter 4, the accuracy of multi-purpose Monte Carlo codes such as FLUKA and Geant4 is tested against more

detailed but also more complex Monte Carlo models in simulating DT procedures. The results of Chapter 4 are used to confirm that general purpose Monte Carlo codes like FLUKA and Geant4, used with their default level of physics detail, are reliable tools for accurate end-to-end simulations of DT devices, something that is a necessary prerequisite in Chapter 5. Chapter 5 includes a concept upgrade of the Adaptix technology to a version appropriate for mobile chest DT. The performance of the upgraded FPS array, the beam characteristics, the image quality and the patient dose are studied thoroughly using detailed Monte Carlo simulations to get deep insight of this concept upgrade. This insight is already being leveraged by Adaptix in the development of their new line of portable chest DT systems. Finally, Chapter 6 contains an automated method to find optimum machine specifications for a multi-FPS chest DT system with groups of the FPS arrays presented in Chapter 5. The optimisation method is packaged into a Python application and takes into consideration engineering, image quality and clinical workflow specifications to find optimum design configurations for Adaptix's new line of multi-FPS portable chest DT systems. The application is used to find specification margins for these systems and the optimum designs within those margins for two versions of FPS are found and are thoroughly characterised. These optimum designs form the founding blocks upon which Adaptix builds their new multi-FPS chest DT systems. Chapter 5 and Chapter 6 are complementary and present research that has been carried out within this PhD project and which is being currently exploited at an industrial level.

Chapter 2

Adaptix flat panel source digital tomosynthesis systems

Until recently, portable 3D imaging was limited to half-ton machines that imaged the patient with a slow mechanical scan of a single X-ray source. These limitations were overcome when the multi-award company Adaptix Ltd demonstrated DT in a veterinary clinic using portable devices the size of a desktop computer that rapidly irradiated the patient with an electronically controlled, compact and stationary FPS array.[13] In this chapter, the Adaptix FPS technology is described and the resulting DT images produced are presented for comparison next to their 2D equivalents. Schematics and photographs of the Adaptix devices are shown while technical details and image examples are given for all the applications where Adaptix has demonstrated usability of their FPS and of their square source array technology at a clinical or preclinical stage.

2.1 The line of Adaptix portable DT systems and their applications

Examples of Adaptix DT imaging systems are shown in Figure 2.1. Regardless of application, they all share the same general design: compact devices, similar in size to a desktop computer and made of a FPS array and a flat panel detector which are fixed in place with reference to each other. The FPS array includes tens of cold-cathode X-ray sources that due to their planar distribution, irradiate the detector from different projection angles. These sources are activated electronically in a rapid and sequential manner without any mechanical movements of the FPS or the detector. The images generated by all the X-ray sources are then reconstructed in less than 30 s[13] into a stack of 3D images using a DT reconstruction algorithm.[61] Adaptix has demonstrated DT of human cadavers (hands, feet, skulls, teeth), of small animals and of electronic devices using FPSs at an accelerating voltage close to 60-70 kVp.[13] Examples of DT images with an FPS and with a movable X-ray tube that emulates the positions of the

FPS array are shown in Figure 1.2 and Figure 2.2. Current work on upgrading to higher voltages and multiple panels for chest DT are discussed in Chapter 5 and Chapter 6.

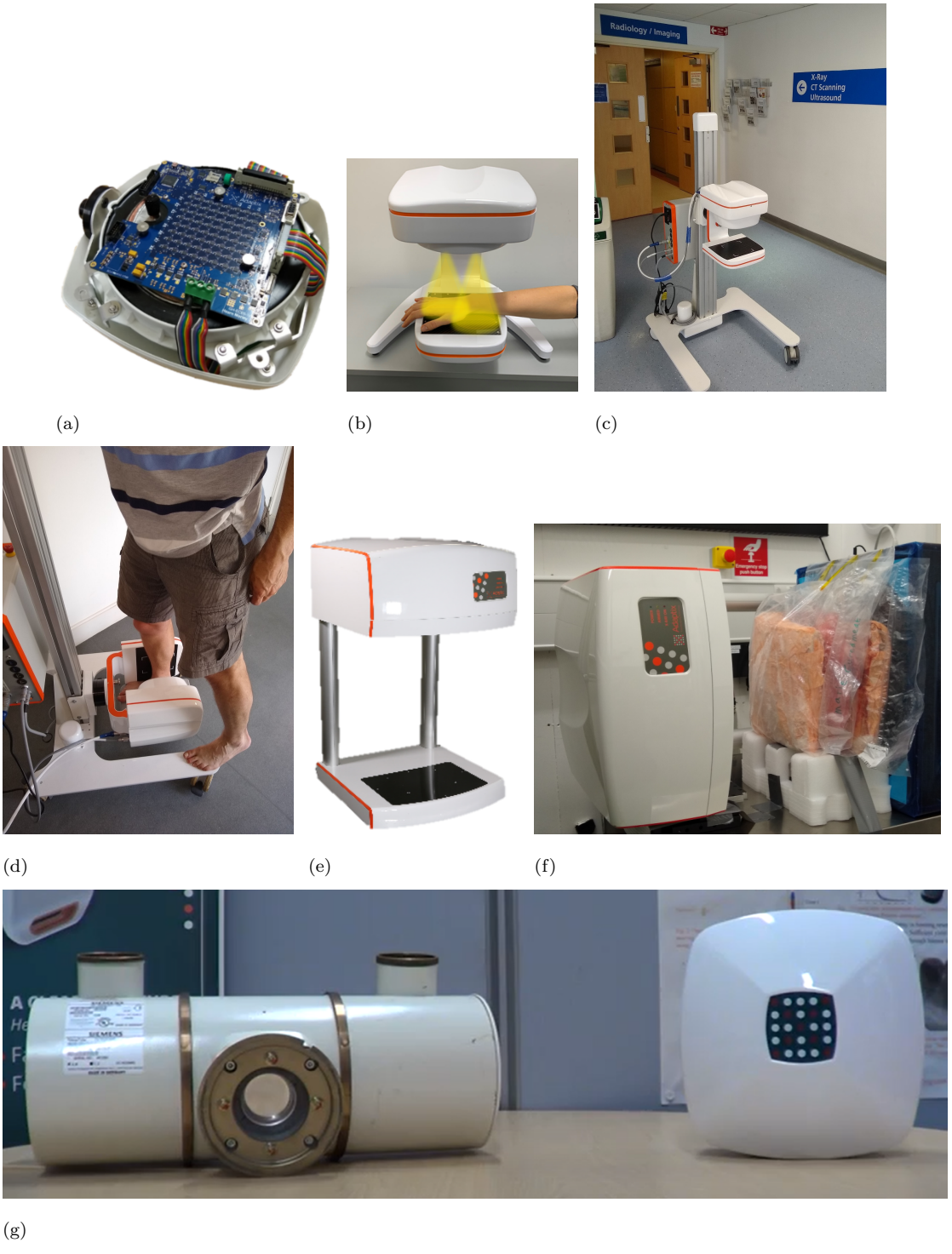

(a) (b) (c)

(d) (e) (f)

(g)

FIGURE 2.1: The Adaptix DT technology. a) Flat panel source array exposed, b-c) Orthopaedic DT system, d) weight-bearing orthopaedic DT, e) Veterinary DT system, f) DT of pig tissue, g) dental FPS compared to a typical, single-source, X-ray tube. (a-f) reproduced with permission from Adaptix Ltd.

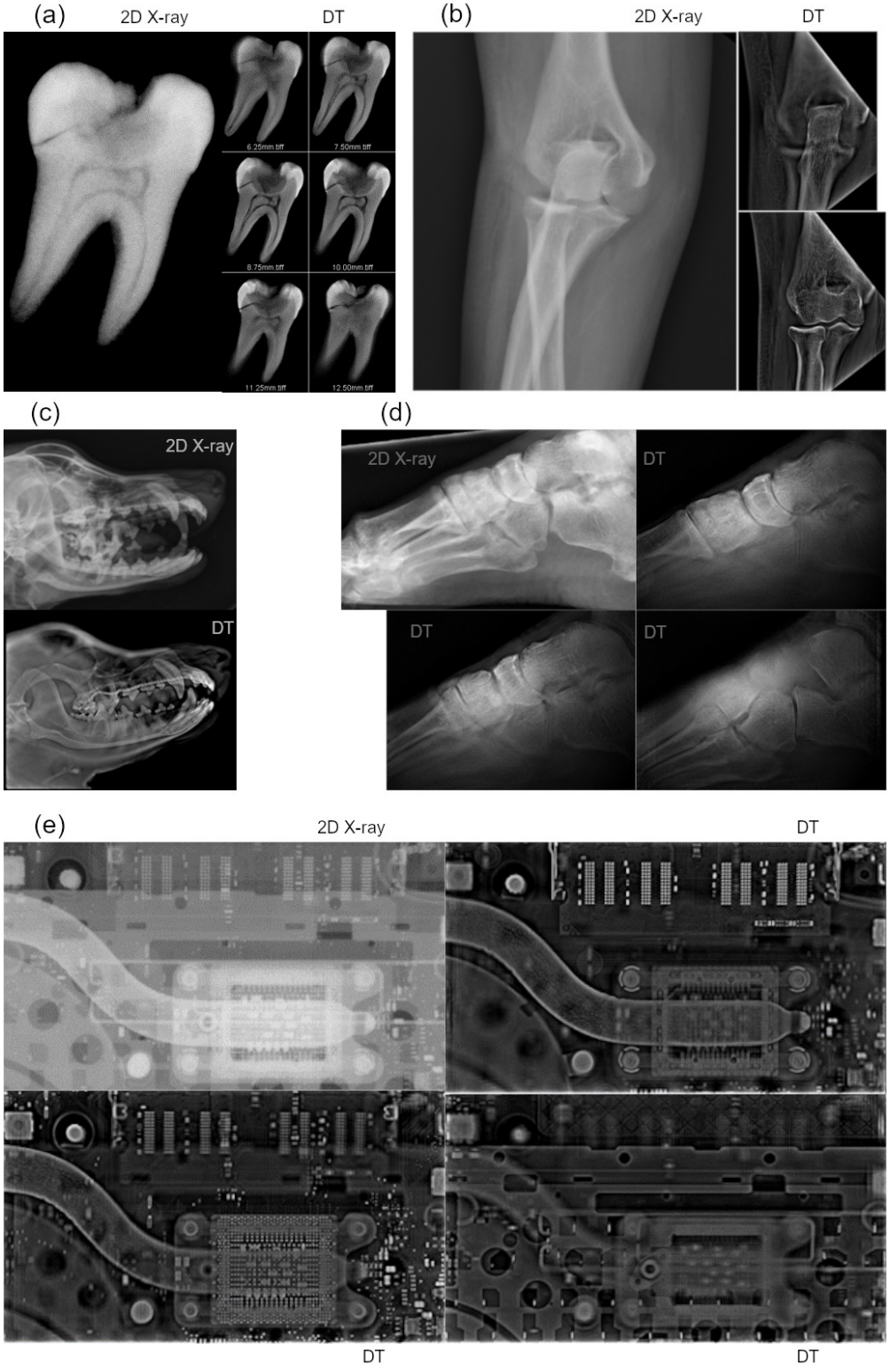

FIGURE 2.2: DT images at different depths using Adaptix square arrays of X-ray sources compared to 2D images. a) tooth, b) elbow, c) dog head, d) foot, e) laptop. (b) and (d) were generated by an FPS and the rest by a movable source that emulated the FPS. Tissue projections overlap in 2D obscuring fine details and depth information but DT produces image planes that correspond to different depths. Objects at the depth of an image plane are in focus on that plane and the rest are blurred out. This allows the 3D structure and 3D location of bones, tubes, soft tissues, electronic components and root canals and fractures of teeth to be identifiable and more clearly observed. See also Figure 1.2. Reproduced with permission from Adaptix Ltd.

2.2 Technological details of the Adaptix FPS arrays

The Adaptix FPS comprises the vacuum enclosure, the cathode with the etched array of electron field emitters, magnetic coils that steer each electron beam into the dedicated collimator apertures to turn each X-ray source on and off, collimators for each X-ray source, a transmissive X-ray target and beam filters. Schematics of a FPS are shown in Figure 2.3.

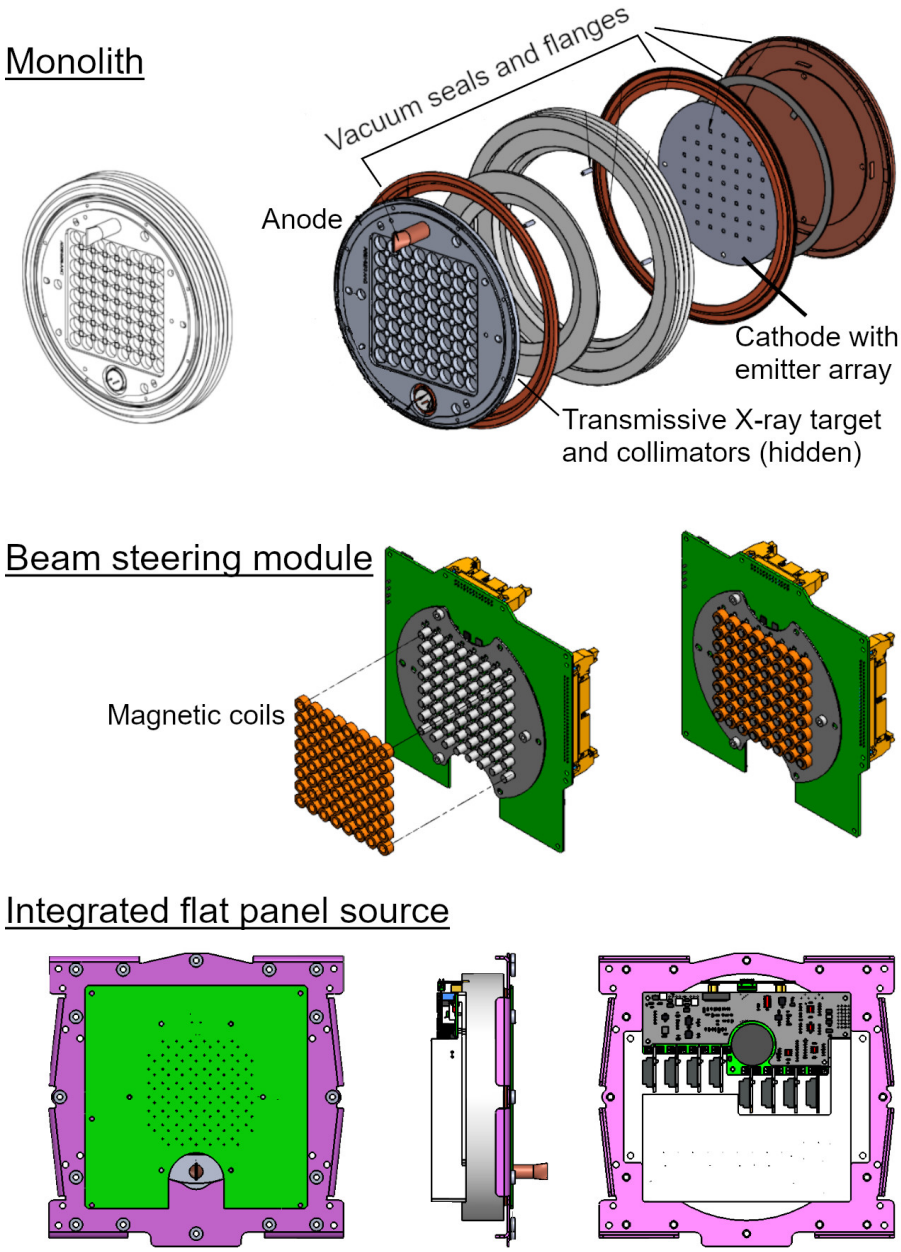

FIGURE 2.3: Schematics of the Adaptix FPS. Reproduced with permission from Adaptix Ltd.

The emitters are nearly 100 µm wide and they are etched on a silicon (Si) wafer in rows and columns with an offset not more than a couple of centimetres. A 60 kV-70 kV

potential difference between anode and cathode creates an electric field between them. Due to the sharp shape and narrow size of the emitters, high electric field gradients develop around them. These gradients are high enough for electrons on the emitters to gain enough energy and escape. This phenomenon is called field emission and avoids the need of heated filaments that are used in conventional X-ray tubes. Heated filaments supply the necessary energy for electrons to escape using heat, a phenomenon called thermionic emission. The electrons that escape are then accelerated by the potential difference towards the anode. Photographs of a cathode and an anode are shown in Figure 2.4.

(a) (b)

FIGURE 2.4: Cathode and anode of the Adaptix FPS: a) the array of electron field emitters etched on the wafer cathode, b) the anode that also acts as an X-ray filter. Large holes on the anode are used to accommodate the magnetic coils and small holes act as filters and collimators for the X-ray sources. See also Figure 2.3.

A multi-hole collimator stands between cathode and anode, with one aperture dedicated for each emitter. The apertures are at a lateral offset from the straight path of the electron beams so when the FPS is armed, electrons travel in a relatively straight path and are absorbed in the collimator; radiation is not emitted. However, magnetic coils shown in Figure 2.3 can be electronically activated to steer individual beams into their dedicated aperture so that they interact with the transmissive X-ray target; radiation is emitted. The wide wells shown in Figure 2.3 and Figure 2.4 are there to accommodate these magnetic coils. Depending on the device (dental, veterinary etc), a different source-to-image distance (SID) is used and different sizes of flat panel detectors so the collimators have different aperture diameters to produce the appropriate size of X-ray field at the specified SID. A simplified cross section of the geometry of one source on the FPS array is shown in Figure 2.5.

Electronic switching of the individual sources on the FPS array takes less than 10 seconds which is faster than the commercial DT systems with a single movable X-ray source.[45] Also, the transmissive target creates a uniform X-ray field rather than a skewed one produced by reflective targets used in conventional X-ray tubes. This phenomenon of skewed fields is called the heel effect and is caused by the angulation of the X-ray target with reference to the electron beam axis and the X-ray beam axis. In the Adaptix FPS, the electron beam axis, the X-ray beam axis and the normal to the X-ray target are parallel to each other as shown in Figure 2.5.

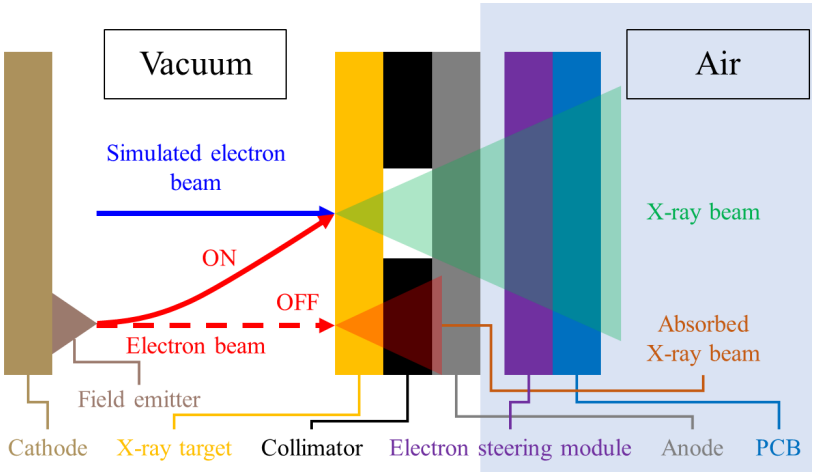

FIGURE 2.5: Simplified cross section of one element of the Adaptix flat panel source array showing the X-ray beam generation inside it. PCB stands for printed circuit board. See also Figure 2.3.

The SID for the dental system is close to 12 cm using an intraoral detector while orthopaedic imaging is done at an SID of 20 cm with a flat panel detector. Finally, the veterinary system has an SID of 45 cm with a flat panel detector. The SID and the size of the array dictate the angular range of the X-ray projections therefore they affect the image quality, especially the depth resolution.[47] On the other hand, keeping the SIDs short increases (to the power of 2) the photon density at the detector which means a source at half the SID is 4 times as efficient; 75% drop in necessary input power. These short SIDs are applicable thanks to the compact nature of the FPS array contrary to an X-ray tube as shown in Figure 2.1 and thanks to the devices being tailored for tomosynthesis, avoiding the large SIDs used in 2D radiography to minimise image magnification effects. The image quality and irradiation geometry due to different source designs such as SID, X-ray cone angle and emitter distribution are investigated later on in this thesis for chest tomosynthesis.

Image resolution is divided in in-plane resolution which depends on the flat panel detector and in depth resolution which depends on the irradiation geometry.[32] 200 μm in-plane resolution is currently available with commercial, non-portable DT systems of other companies[44,45] whereas there are flat panel detectors that offer 160 μm in-plane resolution and could be used with Adaptix FPS.[46] Also, intraoral detectors offer in-plane resolution close to 30 μm and they have been used for stationary intraoral tomosynthesis.[40] On the other hand, because the density of the slices can be defined by the user,[61] and because DT is not clearly a 3D modality, rather than a quasi-3D or sometimes called 2.5D, depth resolution is not defined like in CT. Instead, image quality metrics are used to give a measure for it like the artefact spread function which quantifies how quickly shadow artefacts are blurred out in out of focus planes.[62] The Adaptix FPS has been shown to provide improved depth resolution compared to linear arrays.[32]

The short SID and the compact and lightweight FPS arrays make the Adaptix imaging systems truly portable and deployable on the desktop. Also, the source and the detector are fixed in position with reference to each other which removes any alignment issues during operation, something that must be taken care of for each projection with rotating systems.[37] With the electronic switching of the FPS array, tens of projections are taken in a few seconds and the reconstructed 3D images are available to the clinician less than 30 seconds later. Also, thanks to a novel, meshless reconstruction method, a user defined subset of the slices can be reconstructed, which corresponds to a specific depth range in the patient.[61] Because fewer images are reconstructed, results are presented even faster.

The Adaptix human DT systems are at a pre-clinical stage, gradually reaching maturity to get to the market. The veterinary machines have been used in veterinary clinics with live animals and the company is now building an upgraded version of their FPS to perform chest tomosynthesis. The design and optimisation of such an upgrade has been investigated thoroughly as part of this PhD project and the results are presented in Chapter 5 and Chapter 6. In Chapter 5, the concept upgrade is investigated using detailed Monte Carlo simulations that reveal the expected FPS performance, X-ray beam characteristics, patient dose and image quality. Chapter 6 presents automated irradiation geometry optimisation methods that were developed with Python and were used to identify optimum designs for a multi-FPS chest DT system. These optimisation studies took into consideration engineering, image quality and clinical workflow challenges and objectives and along with the physics simulations, they provide a comprehensive design and optimisation framework for the new line of Adaptix multi-FPS chest DT systems. Such a thorough framework has been instrumental in the optimisation of existing Adaptix technology and in the first steps of introducing a new line of 3D X-ray imaging systems. In the following chapter, a Monte Carlo simulation framework of the current, clinically used FPS is built so that it can be later used for the optimisation of the technology and for the design of the upgraded version for chest DT. Monte Carlo simulations offer insights to information which is difficult or impossible to get with experiments and as such, developing a simulated digital twin of the Adaptix FPS is an important step towards the design and optimisation of this novel technology.

2.3 Summary

Adaptix FPS technology has been a major leap forward for 3D X-ray imaging. The company offers portable 3D X-ray imaging with devices that are smaller, lighter, faster and have better image quality than conventional systems. Applications include NDT for industry and medical imaging for human and veterinary medicine with the medical applications having been demonstrated at a clinical and a pre-clinical level. But the technology is still at an early stage so a wide horizon is open for new physics and engineering research. During this PhD project, both aspects of research were carried out

using a variety of powerful tools like Monte Carlo codes, optimisation algorithms, realistic human phantoms and high-performance computing facilities. End-to-end simulation frameworks were developed to characterise the FPS technology in terms of its physical attributes, diagnostic information and patient dose as well as its compliance to international regulations on radiation safety. These multidisciplinary studies have offered detailed knowledge of the physics and engineering aspects of this new technology and allowed Adaptix to make informed decisions about the development of their novel and truly portable 3D imaging systems. These studies are presented in the next chapters.

Chapter 3

Monte Carlo model of the Adaptix flat panel source

To model, characterise and optimise the Adaptix FPS, the FLUKA [59] and Geant4 [60] Monte Carlo codes were used. These are multi-purpose particle transport codes that have been benchmarked extensively with other codes and with experiments and have found applications in accelerator science, radiation shielding, medical physics and space science among others. The codes have been used in this thesis to simulate the X-ray beam generation, the beam transport in air and in the imaging subjects as well as to model the detector performance. This allows the development of a digital twin of the FPS DT systems which can be used to extensively study the capabilities of the systems in a highly detailed, affordable and reproducible manner, especially when experimental solutions are impossible, not robust enough or simply prohibitive from a financial perspective. In this chapter[1], FLUKA and Geant4 are used to model the X-ray beam generation and the models from both codes are validated with experiments from real FPSs. The models were found to be practically identical and reproduced the experimental results. Therefore, both Monte Carlo models are considered robust and equivalent, and they are used in the rest of the thesis as computational representations of the Adaptix FPS.

3.1 Source geometry

At the time of this work, a 45-emitter FPS was available, so it was used to build and validate the FLUKA and Geant4 Monte Carlo models of this chapter. For simplicity, all emitters were considered identical in the simulations thus modelling one X-ray source would characterise the whole FPS array. Testing of this assumption on a real FPS is presented in Section 3.7.

The modelled geometry of one of the X-ray sources on the FPS array as drawn by FLAIR [64] is shown in Figure 3.1. It included a 10 μm thick tantalum (Ta) X-ray target, a 1 mm thick tungsten (W) X-ray collimator with 1 mm hole diameter, a 200 μm vacuum

[1] Parts of this chapter have been presented at the 12th International Particle Accelerator Conference. [63]

gap, a 150 μm titanium (Ti) anode which also acted as the vacuum to air interface and a 1.6 mm thick PCB placed 8.3 mm downstream from the anode. The PCB was made of epoxy and included a 70 μm layer of copper (Cu) electronics. The epoxy material was available in FLUKA as a 1.85 g cm^{-3} compound made of 19 hydrogen (H) atoms, 18 carbon (C) atoms and 3 oxygen (O) atoms. Epoxy was created in Geant4 according to an existing simulation example available online.[65] It had a density of 1.86 g cm^{-3} and was a compound of two materials with fractional ratios of 0.528 and 0.472. The first material was SiO_2 with 2.2 g cm^{-3} density. The second material had 1.2 g cm^{-3} density and was made of 2 H atoms and 2 C atoms.

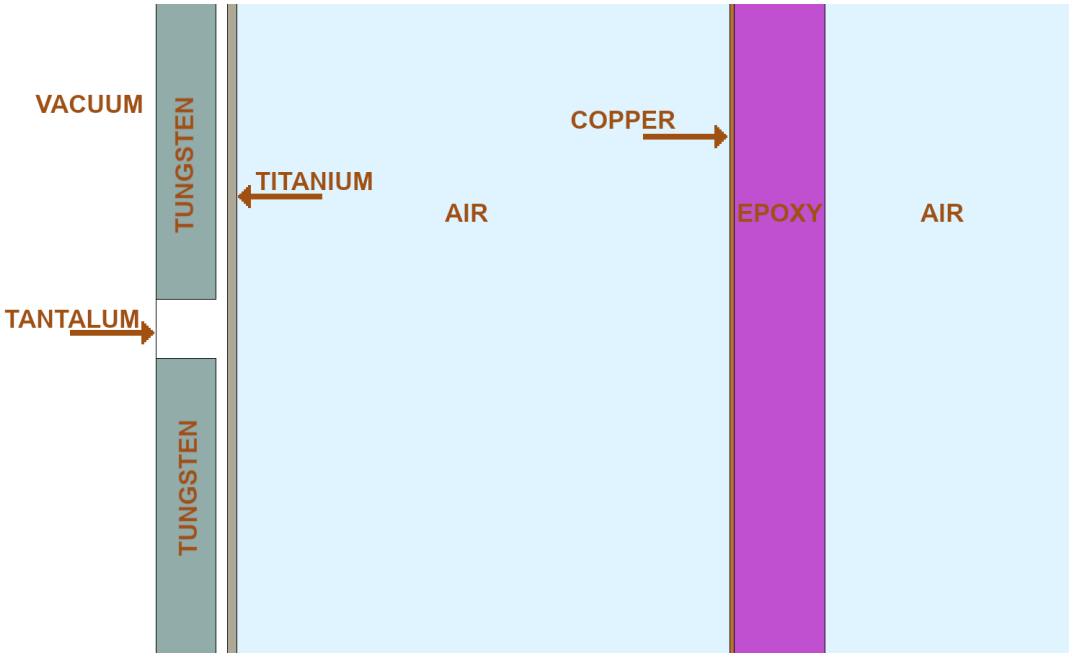

(a)

FIGURE 3.1: Geometry of the FLUKA source model plotted in FLAIR. The electron beam comes from the left and hits the Ta target at the centre with reference to the W collimator aperture. The resulting X-ray beam travels to the right and is shaped into a cone by the collimator and filtered by the Ti anode which acts as a low energy cut-off filter. The Cu and epoxy slabs represent the PCB. Geant4 model is identical. See also Figure 2.5.

Within the FPS there are electromagnetic fields. These are primarily the accelerating electric field, the magnetic field of the steering coils, the electromagnetic fields caused by the primary electron beams and the electromagnetic fields caused by the clouds of scattered electrons inside the FPS. When electrons hit the X-ray target or the collimator, a large portion of them is reflected back and might be redirected again towards the target due to those electromagnetic fields. Primary beams are also expected to be affected by those fields, resulting in an offset of their trajectory away from their intended targets or in the spreading and reshaping of their beam spot. Therefore, any combination of off-focal radiation and reduction of photon yield is expected to emerge.

Regarding off-focal radiation, Adaptix found that the back scattered electrons were absorbed several cm away from the corresponding source so their off-focal radiation was expected to be negligible. Nevertheless, as explained before, when the machine is armed, electrons are accelerated but due to their offset from the collimator aperture they are absorbed, something that is also confirmed experimentally by Adaptix. So, X-ray radiation is produced only when the electron beams are steered towards the centre of the collimators. Any other situation results in absorption within the FPS meaning that the various electromagnetic fields inside the FPS are not strong enough to cause a significant amount of off-focal radiation. As such, although off-focal radiation should be investigated and accurately quantified during dosimetry, especially when optimising the design to follow radiation safety regulations, it was decided that it would not be simulated in this project.

This decision was also based on the fact that at this early stage of development, modelling was focused on the general beam quality of the FPS and on the resulting images, both of which were possible to validate with experimental apparatus that was available at the time. More elaborate modelling of the electromagnetic phenomena taking place inside the FPS was burdened by laboratory limitations at the time that did not allow model validation with reliable experiments within the FPS geometry. Such limitations included non-repeatable behaviour of the FPS prototypes and engineering challenges with doing experiments within the FPS geometry while the FPS was operational.

Due to those experimental limitations, space charge effects and electron beam shape and size were not simulated but were instead approximated. This may have caused an overestimation of the photon yield and ultimately of source efficiency as shown later.

Photon yield can also be affected by the angle of incidence of the electron beam. When the magnetic fields steer each beam into its dedicated aperture in the electron collimator, the beam is incident at an angle and is not normal to the X-ray target. This is expected to affect the X-ray field shape as well as the photon yield. However, the field emitter is at a lateral offset of only 1.5 mm from the collimator aperture and the wafer is 10 mm away from the X-ray target. Therefore, the angle of incidence might be close to 9°. Simulating different angles of incidence without electromagnetic fields with the source geometry shown on Figure 3.1 and plotting the photon yield at the exit of the X-ray collimator aperture, it was found that less than 3% of photons were lost when the electron beam was incident at 10°, as shown in Figure 3.2. The beam losses are due to the X-ray field being slightly skewed thus a larger portion of it is absorbed in the collimator. On the other hand, the narrow possible angles of incidence, the low energies of the electrons and the low amount of off-focal radiation mean that the shape of the X-ray field at the SID of the various Adaptix systems mentioned in this thesis is still expected to be radially symmetric.

Apart from the primary beam, the aforementioned electromagnetic fields affect the off-focal radiation that stems from scattered electrons. But the electron energies are rather low thus scattering is practically angularly uniform. So, because the 1 mm wide

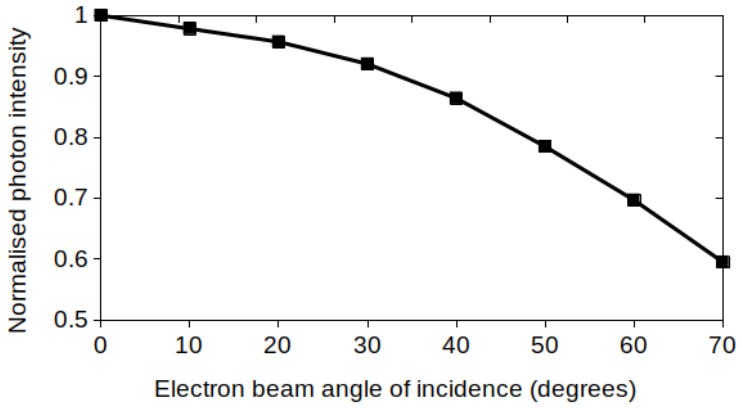

FIGURE 3.2: FLUKA simulated photon yield measured at the exit of the X-ray collimator aperture of Figure 3.1 as a function of angle of incidence of the electron beam. The electron beam is always incident on the centre of the X-ray target. Error bars are less than 1% and are omitted.

collimator aperture and the 1 mm collimator thickness create a $\pi/4$ solid angle, roughly $\pi/4/2\pi = 12.5\%$ of the uniformly backscattered electrons can exit the collimator. And these electrons will mostly reach the collimator again to be fully absorbed since the possibility of a backscattered electron entering any of the 45 collimator apertures, when the latter are arranged in a 5×5 configuration with 1 cm pitch (see Chapter 4) and assuming scatter angle is random which it practically is, is equivalent to the ratio of the surface areas of all the 45 apertures and the total area of the emitter array, so a probability close to $45 \times \pi \times (0.1mm)^2/(4 \times 1cm)^2 = 0.09\%$. Also, as mentioned before, Adaptix observed radiation damage from back-scattered electrons several cm away from their apertures, supporting the assumption of low probability of electron re-entry in its aperture.

According to all the above, off-focal radiation is expected to be negligible for the scope of this thesis, the electromagnetic effects within the FPS geometry could not be reliably studied in the laboratory but nevertheless the resulting X-ray beam was still expected to be radially symmetric but with potential loss of photon yield. Beam shape and intensity could be measured with available equipment at the time so any photon yield losses could be quantified even if not characterised in detail. Therefore, the complexity incurred by using a detailed transportation of the electron beam within the electromagnetic fields inside the FPS geometry was deemed not justifiable. Thus, electromagnetic fields were omitted, and a number of approximations were used to define the electron beam.

Because of the lack of accelerating voltage, it was decided that the electron beam would have an initial kinetic energy equal to the maximum possible kinetic energy with a given accelerating voltage. The FPS under investigation operated at a nominal 60 kV accelerating voltage so the beam initial kinetic energy was set to 60 keV. Also, the real electron emitters were approximately 100 μm in diameter so the electron beam was set to be a Gaussian pencil beam with a 6σ width of 100 μm. Moreover, for simplicity,

the beam would hit the X-ray target at its centre and at a normal incidence given the radially symmetric X-ray beam expected even with electron beams at an angle.

Radiation coming from the electrons reaching the electron collimator after being reflected from the X-ray target is also very small. That is because the collimator is purposely made to absorb the primary electrons and the resulting photons thus scattered electrons with their lower energy and any resulting lower energy photons are absorbed as well. So, to reduce the model complexity even more, that collimator was set to immediately kill any electrons entering it or generated in it. Photon transport was instead simulated everywhere.

All these settings and assumptions were applied to both FLUKA and Geant4 and their impact is discussed further in Section 3.9.

3.2 Physics settings

Due to the attenuation in the anode and the PCB, the photon energy spectrum did not have values lower than 15 keV. So, a 15 keV energy cut was used in FLUKA with the DEFAULTS card set to PRECISIO, meaning all possible interactions were activated. In Geant4, the PENELOPE[66] physics list was used with the range cut of 1 mm. Therefore, all possible electromagnetic interactions were activated, and the energy threshold depended on the material, so that the minimum range of the particles did not exceed 1 mm. Due to the μm thickness of the X-ray target and the filtering components, one would expect a range cut of a few μm to be a better choice. However, the codes still behaved similarly as shown later so the 1 mm range cut proved to be adequate.

3.3 Scoring and beam characterisation

The phase space of particles that exited the PCB was recorded. After collecting several hundred thousands of particles, the phase space was fit with analytical functions to characterise the X-ray beam in terms of its shape, size, divergence and energy spectrum. Electrons were fewer than 100 so they were discarded from the beam characterisation. Nevertheless, the outer, plastic cover of the real machine is expected to simply absorb any electrons escaping from the FPS.

The X-ray collimator had a circular aperture therefore the X-ray field could be considered rotationally symmetric. Using a radial plot of the photon density on the PCB, a maximum radius was defined outside of which the photon density was practically zero and any photons that were there were discarded from the phase space. This was necessary because the penumbra was an exponentially decaying function, and a maximum limit of photon position was required to later sample photons that follow that distribution. This stripping process is shown in Figure 3.3.

Also, because there were no beam shaping components after the X-ray beam had left the source, the divergence was constant. To define the photon direction and thus the

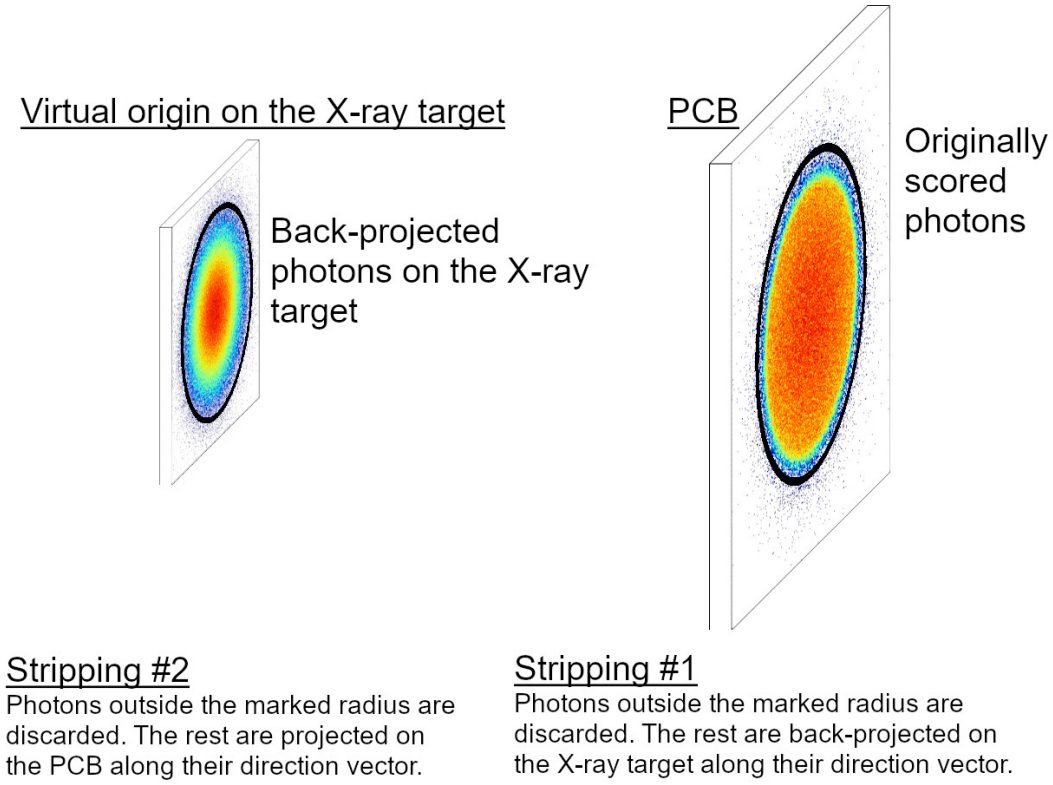

FIGURE 3.3: The stripping method on the X-ray photon results of the Monte Carlo source simulation. In order to fit the results with analytical functions, limits had to be forced that would act as boundary conditions for the fitting algorithms. These limits were set by eye as a maximum radius close to where the beam intensity became negligible. After the two stripping processes, analytical functions are fitted on the phase space of the photons on the PCB. The back-projected beam spot is orders of magnitude smaller than that on the PCB, but it is drawn larger for illustration purposes.

beam divergence, the remaining photons from the stripping process described above were projected back to the X-ray target surface along the opposite of their direction vector. This surface was the exiting surface and not the one where the electrons were incident on. Using a radial plot of the back projected photons on the X-ray target, a maximum radius was again chosen that defined the virtual beam spot size on the X-ray target. This was considered as the virtual origin of photons that reached the PCB. Photons which fell outside this virtual beam spot were considered scatter and were discarded. The remaining photons were projected back to their original position on the PCB. These two stripping processes were done to remove scattered photons that are either already not part of the main X-ray beam (photons outside the user defined radius on the PCB) or that travel at much wider angles than the main beam (photons outside the user defined virtual origin on the X-ray target). To sample the direction of a photon, first the photon position on the PCB is sampled and its virtual origin mentioned above is considered to be the centre of the X-ray target surface. The unit vector between these two points is the photon direction vector.

Finally, the energy spectrum was a function of photon position. In the beginning, two spectra were defined, one for the beam core and one for the penumbra. The intersection

of the beam core and the penumbra was a circle on the X-ray field, the radius of which was selected manually close to where the actual penumbra met the beam core. However, when sampling from two different energy spectra on the same X-ray beam, the transition from the beam core to the penumbra was not smooth but created a ring artefact on the energy density of the X-ray field. So, for simplicity, it was decided that the energy of all photons would be sampled from the energy spectrum of the beam core regardless of whether they belong to the beam core or the penumbra. So, the energy spectrum of the photons that belong to the beam core was fitted with analytical functions and that spectrum was defined as the energy spectrum of the whole X-ray beam.

3.4 Results

After transporting 6×10^9 primary electrons in FLUKA, 509,035 photons and 11 electrons were scored on the PCB. These electrons were neglected. As it will be shown later, the beam intensity was negligible after 1 cm from the centre. Therefore, photons that were outside a ring with radius of 1 cm were discarded. These were then projected back to the X-ray target along the opposite of their direction vector. The radial photon density at the target was also negligible outside a ring with radius equal to 65 μm so photons outside this ring were also discarded. 35,354 photons were discarded from the PCB and 813 from the X-ray target so 472,868 were left or 7.11% of photons were discarded. Thus, the photon yield of this model was 472,868 photons/6×10^9 primary electrons or 7.88×10^{-5} photons per electron.

In Geant4, 1×10^9 primary electrons were transported which resulted in 78,149 photons and 9 electrons escaping from the PCB. These electrons again were neglected. Applying the same stripping procedures as before, 5,200 photons were discarded from the PCB and 99 from the X-ray target, thus 6.78% of photons were discarded. Thus, the photon yield was 7.29×10^{-5} photons per electron which was 7.5% different from the FLUKA result.

Because of the low number of photons, the Geant4 phase space was rotated around the beam axis 4 times by 72°. This increased the number of photons to a value closer to the number of photons produced by FLUKA but without the risk of introducing biases to the photon density and energy distributions.

The radial and energy distributions from both codes are shown in Figure 3.4. As with the photon yield, the radial density and energy spectrum generated by both codes were similar. The photon density was practically zero after 1 cm and there were no photon energies lower than 15 keV. With this number of photons, distributions were still noisy but their general shape was obvious. The energy spectrum of the penumbra was noisier than the beam core because of the far fewer photons that it contained. For both models, the transition from the beam core to the penumbra was set manually close to where the exponential decay begins, specifically at r=$\sqrt{0.3}$ cm.

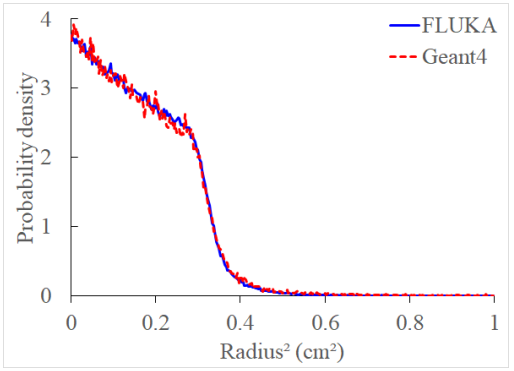

(a)

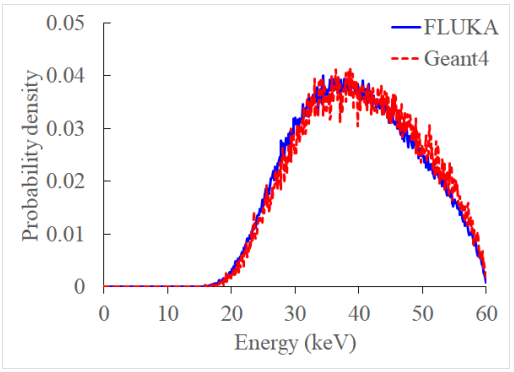

(b)

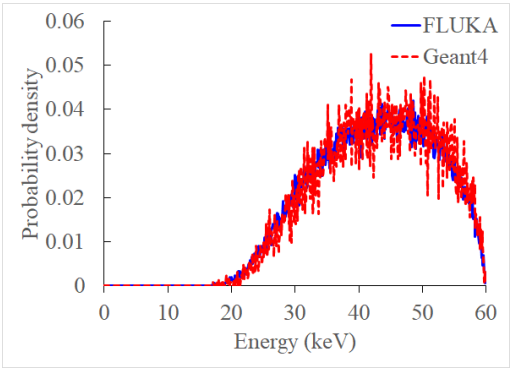

(c)

FIGURE 3.4: Source model results generated by FLUKA and Geant4. a) Beam radius on the PCB, b) Energy spectrum of the beam core and c) Energy spectrum of the penumbra.

3.5 Analytical fit

The number of photons produced in these simulations are not enough for further dosimetry and image quality simulations. Therefore, a method is required by which photons are sampled that follow the distributions in Figure 3.4. But the raw distribution of the radial density is noisy and produces image artefacts in the form of rings if used as is. Therefore, analytical fits of the radial distributions were used to have a smooth distribution to sample from. Analytical fits were also applied on the energy spectra to maintain the same practice although it was not strictly necessary. Also, because it was decided to

sample the photon energy from the distribution of the beam core for all photons whether they belong to the beam core or to the penumbra, the energy spectrum of the penumbra is not used in the following.

The radial density of the photons is fitted with 3 analytical functions. One to describe the beam core, one the penumbra and one to allow a smooth transition between the two. The beam core and the transition are polynomic fits and the penumbra is an exponentially decaying function. Details are shown in Table 3.1.

TABLE 3.1: The analytical fits of the photon density and the energy spectrum of the beam. The a_i parameters are coefficients of the polynomic fits and the a and b parameters are from a $f(x)=ae^{bx}$ fit.

Parameter	Beam core	Transition	Penumbra	Energy spectrum
		FLUKA		
a_0	3.76	-8.04		-1.44
a_1	-6.15	86.69		0.39
a_2	5.15	-176.45		-0.044
a_3				0.0027
a_4				-9.97×10^{-5}
a_5				2.23×10^{-6}
a_6				-3.01×10^{-8}
a_7				2.27×10^{-10}
a_8				-7.31×10^{-13}
a			3362.58	
b			-24.14	
		Geant4		
a_0	3.79	4.40		-1.49
a_1	-6.54	1.59		0.40
a_2	4.51	-31.24		-0.044
a_3				0.0027
a_4				-9.54×10^{-5}
a_5				2.10×10^{-6}
a_6				-2.81×10^{-8}
a_7				2.09×10^{-10}
a_8				-6.66×10^{-13}
a			1070.49	
b			-20.78	

3.6 Model validation

To test the accuracy of these models, a dose rate experiment was performed using the FPS. An RTI Black Piranha[67] was centred to the X-ray field and at a distance of 70 cm from the X-ray target to measure the incident air KERMA (Kinetic Energy Released per unit Mass) at that position. Aluminium (Al) sheets were placed downstream from

the source to attenuate the beam and the air KERMA was measured for each added sheet.

Using the analytical model from Table 3.1, photons were sampled in FLUKA and Geant4 to simulate the dose rate experiment. Al sheets of the same thickness as those in the experiment were simulated while the air KERMA was scored within a 1 cm^3 cube at a 70 cm distance.

The dosimeter returned values in mGy/s but the simulations returned values in mGy/primary. In this case the primary particles were the photons sampled using the analytical descriptions. Multiplying the simulation results with the photon yield returned the dose rate in mGy/primary electron. Knowing that the FPS array sends 50 μA of current for each projection, the dose rate can be expressed in mGy/s by multiplying with 50 μA. 50 μA can be expressed as 50 μC/s which in turn is equal to $50\times10^{-6}\times6.2415\times10^{18}$ electrons/s. The electrons from this factor and from the 1/primary electron are normalised and the units become mGy/s.

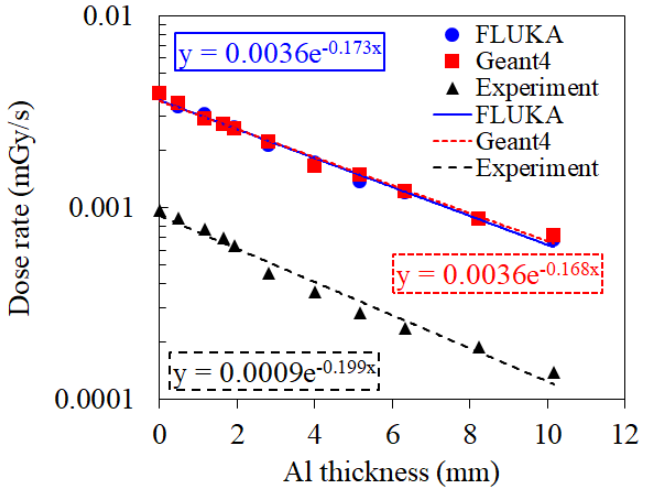

FIGURE 3.5: Validation of the Monte Carlo models with experimental data.

The results of the validation are shown in Figure 3.5. Due to the X-ray beam attenuation from the Al sheets, the KERMA was decreasing at an exponential rate. The two codes agreed with each other but there was a systematic, four-fold discrepancy from the experiment. Potential reasons for this are misalignment of the electron beam in the FPS, its width being larger than the collimator aperture or space charge effects which can affect both the beam trajectory and its shape and size. In all these cases, the electron beam could have been partially absorbed in the collimator, reducing the photon yield. In the simulations, the beam is 100 μm wide and is perfectly aligned to the 1 mm wide collimator aperture which is an ideal scenario, most probably not representative of the true FPS at the current stage of development. Also, another likely reason is that the emitted current was lower than the nominal 50 μA. However, despite these differences, the attenuation trend is similar so the energy spectrum is simulated relatively well.

3.7 Validation troubleshooting

3.7.1 Potential reasons for failure

The emitters in the source array were at a 1.5 mm lateral offset from the centre of their respective collimator aperture. According to Adaptix, the magnetic field generated by the steering coils was very likely insufficient to fully deflect the electron beam by 1.5mm, so some portion of that beam was absorbed by the collimator. In addition, the electron beam has a finite size which may have been larger than the collimator aperture, leading to an additional reduction in the amount of current converted into useful X-ray flux. Also, the emitter and collimator apertures may have not been accurately aligned, so the electron beam was not deflected as expected, and it could have ended up partially within the aperture. Moreover, space charge effects may have reduced the accelerating potential inside the FPS geometry or affected the trajectory, the size and the shape of the electron beam, essentially reducing the number of electrons that reached the X-ray target and their kinetic energy. Furthermore, the electrons did not escape from the emitters vertically either but there was some lateral deviation. This was due to the highly diverging nature of the electric field in the vicinity of the emitter tip (tens-hundreds of nm range). Finally, the electron beam width was also expected to be affected by the finite initial energy distribution of the electrons, since they were field emitted from a range of energies around the Fermi level.

3.7.2 New FPS design

To investigate this discrepancy further, a new source array was devised where the collimator apertures were larger and the field emitters were aligned to the centre of their dedicated aperture. This way, each electron beam would hit the centre of the X-ray target without the need for steering magnetic fields and with fewer losses in the collimator. Photographs of this new FPS array and its FLUKA model are shown in Figure 3.6. It had 45 emitters in a 7×7 rectangular array without the corners. Columns of emitters were labelled A, B, ..., G. Rows were labelled 1, 2, ..., 7. Individual emitters were named alphanumerically like A3 and D4.

The W collimator was 1 mm thick with apertures of 4 mm in diameter and the Ta target was 10 μm thick. The Ti anode was 4 mm thick but there were circular sections with a 4 mm diameter where the thickness was 150 μm thick. These sections were aligned with the collimator apertures. The distance between the collimator and the anode was 200 μm and it was vacuum. A 7 mm Pb collimator was also attached downstream from and on the anode with conical apertures with 2.8 mm and 7.3 mm diameters. Pb slabs were also taped around the collimator to minimise radiation leakage from the sides. Also, because all 45 emitters were etched on the same wafer, when the wafer was connected to a voltage supply, all emitters were active simultaneously. Therefore, to isolate the X-ray beam from each source on the array, steel ball bearings were used to cover all apertures apart from the one that belonged to the emitter under investigation.

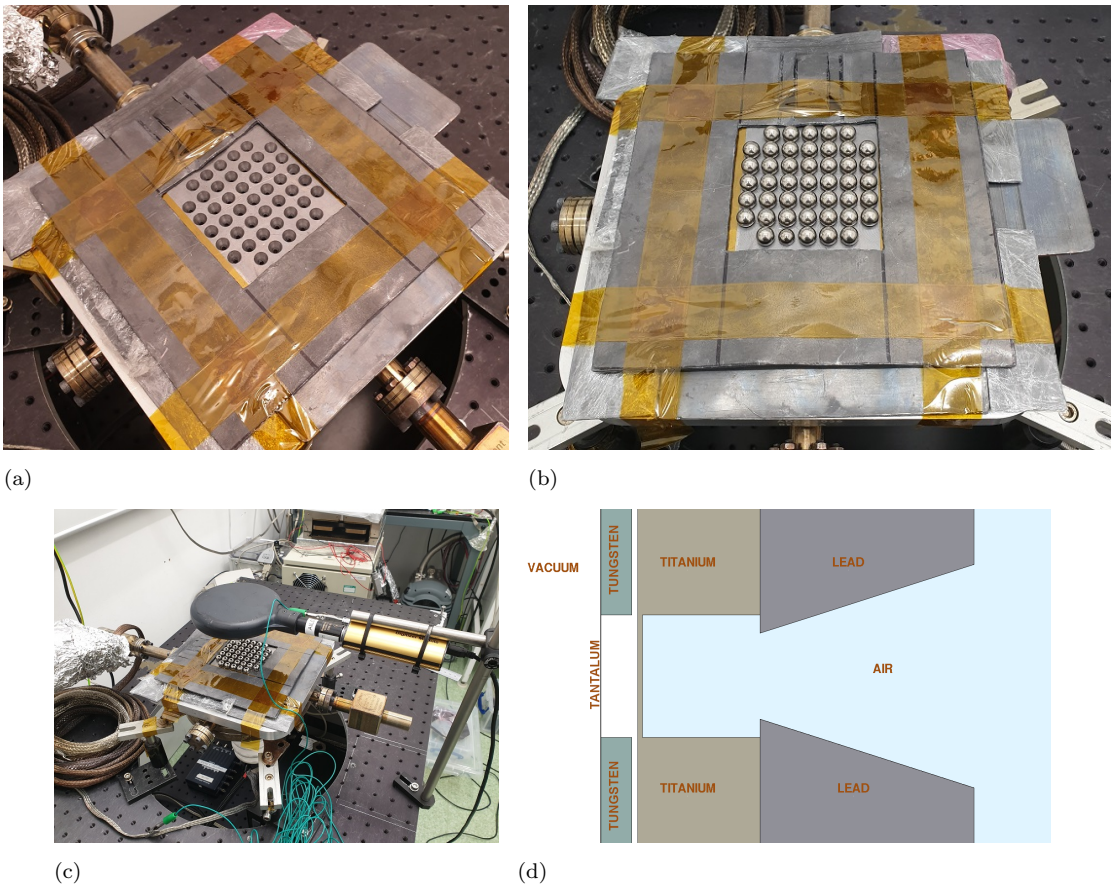

FIGURE 3.6: FPS with collimator aligned to emitter array. a) multi-hole collimator open, b) multi-hole collimator blocked by steel spheres, c) positioning of the dosimeter, d) FLUKA model of the new FPS (a-c) reproduced with permission from Adaptix Ltd.

3.7.3 Experiments with the new FPS

A Radcal[68] 10X6-180 dosimeter was placed downstream so that its centre lay 9 cm away from the X-ray target and was used to measure the dose rate from each source. The dosimeter was aligned by eye to the emitter under investigation and due to the much larger area of the dosimeter compared to the X-ray field at that distance, more accurate alignment was not necessary. Using a high voltage probe, 3 s pulses of 55.53 kV were sent to the wafer and the dose rate of each emitter was measured sequentially.

An Amptek[69] CdTe-123 spectrometer was also calibrated using an Am-241 source and was used to measure the energy spectrum of a small group of the emitters. The distance from the source array was approximately equal to the distance used with the dosimeter. This caused saturation of the spectrometer so a hand-made Pb collimator was used to reduce the amount of radiation detected. A 2 mm thick Pb sheet was used to create the collimator by manually drilling a single hole with approximately 0.5 mm diameter. The Pb sheet was attached to the spectrometer with the aperture aligned to its entrance window.

3.7.4 Monte Carlo simulation of the new FPS

The experiment was replicated in FLUKA. A Gaussian electron beam with 6σ of 100 μm and energy equal to the maximum energy of the measured photon spectrum was transported towards the X-ray target and the phase space of photons exiting the Pb collimator was scored. Photons escaping from both within and outside the collimator aperture were scored. The photon yield of the source was calculated as the ratio of the number of photons scored over the number of primary electrons transported.

The photons from that phase space were transported towards a dosimeter to simulate the air KERMA measurement. The dosimeter was simulated as an air volume the size of the sensitive volume of the Radcal dosimeter which had a 100 cm^2 cross section surface and a 180 cm^3 active volume. The centre of the volume was placed 9 cm from the X-ray target and was aligned to the centre of the collimator aperture. The simulation returned the air KERMA in this air volume. The photons were transported 4 times to improve the statistics of the simulation without a big risk of biasing the result. Also, to achieve air KERMA measurements, the electron energy cuts in the simulation were set to 1 GeV so that all of them were absorbed *in situ* immediately after they were generated.

3.7.5 Unit conversion from simulation to experiment

The air KERMA deposited in the simulated dosimeter was scored in mGy/primary photon and was converted to mGy/primary electron by multiplying with the photon yield of the simulated source.

The wafer used in the experiment did not allow direct measurement of the current supplied to each individual emitter. Therefore, the current to convert the Monte Carlo units to mGy/s was not available. Instead, the total current supplied to the wafer was measured. So, it was decided to use the measured dose rate from each emitter and the simulated dose rate to estimate the current supplied to each emitter. This estimated value would then be compared to the average current expected if the total current was uniformly distributed in the emitter array. To calculate the expected current, the measured dose rate in units of mGy/s was divided by the simulated dose rate that had units of mGy/primary electron. Thus, the result was in units of electrons/s which was converted to Amperes by multiplying with the charge of the electron expressed in Coulombs.

3.7.6 Results

The maximum energy of the measured spectrum was 56 keV and that was the energy of the simulated primary electron beam. The photon yield from the simulation was $4.23 \pm 0.13 \times 10^{-5}$ photons/primary electron. The energy spectrum of these photons is shown in Figure 3.7.

There was a large discrepancy from the experiment, with the simulation producing a softer beam. This can be traced back to the hand drilled Pb collimator. Slight angular

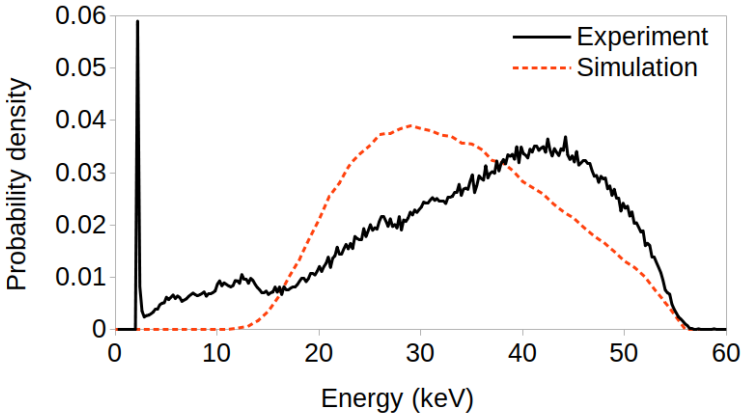

FIGURE 3.7: Energy spectra of a small group of emitters from the new FPS experiment and from the Monte Carlo simulation with one emitter.

misalignment of the aperture with reference to the beam axis probably filtered low energy radiation, causing the hardening of the beam. Also, many photons were detected with energies below 15 keV, below which the simulation estimates zero photon flux. This could be due to the close proximity of the Pb sheet to the spectrometer and the high sensitivity of the latter. Electrons ionised in the Pb sheet might be interacting in the metallic casing of the spectrometer or the clamps used to fix the equipment in position, producing X-ray radiation of a broad energy spectrum. Also, Compton scattering in the aperture prior to detection might be another reason why these low energy photons were detected. The entrance window of the spectrometer had a Be window to protect it from electrons. Finally, the spike close to 2.5 keV of the measured spectrum is of unknown origin, possibly from contamination of the Ta target. An experiment where unwanted filtration and scattered photons were removed could have given more reliable results to confirm the validity of the model in a more robust way. Using an Al filter instead of a hand-made collimator to deal with the saturated spectrometer would have probably produced better results. The attenuation curves in Figure 3.4 are considered a more reliable but still an indirect confirmation of agreement on energy spectrum between simulation and experiment.

After transporting the scored photons four times to the dosimeter, the dose rate was estimated to be $9.94 \pm 0.48 \times 10^{-6}$ GeV/g/primary photon or $6.73 \pm 0.33 \times 10^{-14}$ mGy/primary electron. The average current per emitter and the estimated current using the simulated and measured dose rates are plotted in Figure 3.8. Emitter current is not distributed uniformly in the array but now discrepancies between experiment and simulation are lower than a 3-times factor for most emitters, whereas there was a 4-times factor in Figure 3.4.

3.7.7 Discussion on the troubleshooting

As shown in Figure 3.8, 14 emitters had a discrepancy factor from the average current larger than 3 and 31 of them were below that. That was an obvious improvement from

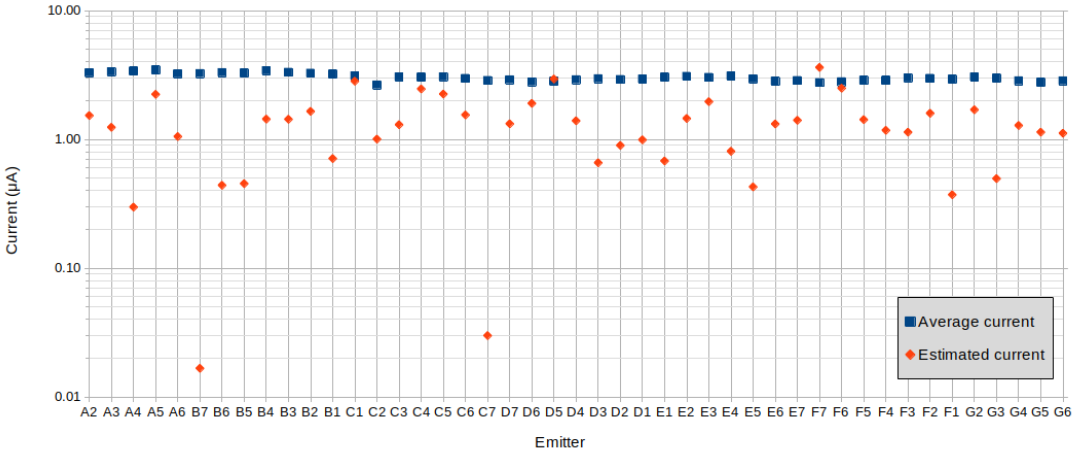

FIGURE 3.8: Performance of a complete wafer of the Adaptix source. Letters denote horizontal and numbers vertical position on the emitter array. Average current is the total input current measured in the wafer divided by the number of emitters. Estimated current is calculated by dividing the measured dose rate with the simulated dose rate per electric current. Errors bars are the size of the points so they are omitted. See the text for details.

the 4-fold discrepancy in Figure 3.4. But this experiment also suggested that there was loss of current in the wafer and that the emitters were not identical as had been the assumption so far in the simulations. So, the four-fold discrepancy in Figure 3.4 may or may not have been due to a combination of beam loss and current loss. The prototype FPS is still under development and non-optimal performance is expected. The fact that the simulations agree with the experiments within a factor of 3 is a promising finding and is deemed satisfactory at this stage. The source model is considered reliable for further studies that will be described later but proper validation must be achieved when a more robust source prototype is manufactured in the future.

3.8 Final adjustments to analytical model

In preliminary imaging simulations, a ring artefact was observed in the X-ray field at the radii where the three analytical descriptions intersected. This was because the analytical fits of the radial density did not have the same 1st derivative at their intersection so the transition from one function to the other was not smooth causing the ring artefact.

To remove it, 4 analytical descriptions instead of 3 were used to define the beam shape and size and adjustments were made manually to them to make for a smoother transition from one fit to the other. A change to the dosimetric characteristics was expected however at a negligible level so no further validation was performed; the slightly adjusted model was assumed to have the same photon yield and energy spectrum as the original.

However, FLUKA and Geant4 have proven twice that they produce the same results and user access to the source code of Geant4 was necessary for the work presented

in Chapter 4 and Chapter 5. Therefore, only Geant4 was used for the rest of this thesis, except where FLUKA is explicitly mentioned, and as such, only the Geant4-based analytical model was adjusted to remove this ring artefact. The new parameters of the model are given in Table 3.2.

TABLE 3.2: The adjusted analytical description of the photon density and the energy spectrum of the beam generated by Geant4. The a_i parameters are coefficients of the polynomic fits and the a and b parameters are from a $f(x)=ae^{bx}$ fit. Parameters are shown in full precision for use in future work.

Parameter	Beam core	Beam core transition	Penumbra transition	Penumbra	Energy spectrum
a_0	3.75531830109	-7.8340080795	-8.0359080795		-1.4868286234
a_1	-6.15155090263	82.3034417985	86.6934417985		0.39795432231
a_2	5.14984950028	-163.60606561	-176.44606561		-0.0442375291165
a_3					0.00266405678493
a_4					-9.54348960127e-05
a_5					2.10229445744e-06
a_6					-2.80512630042e-08
a_7					2.08645076207e-10
a_8					-6.65568439351e-13
a				3362.58062424	
b				-24.1407236835	

3.9 Discussion

A detailed model of the Adaptix FPS array was built and compared to experiments. This X-ray source model is used as a virtual twin of the FPS array in the next chapters for end-to-end simulations of DT imaging procedures. In Chapter 4 the model is used to draw conclusions about the accuracy of general purpose Monte Carlo codes in end-to-end DT simulations that include realistic human phantoms and flat panel detectors and in Chapter 5 it is used to gain deep knowledge of the expected performance of Adaptix FPS technology when this is upgraded to versions best fitted for chest DT. Therefore, the development of a robust Monte Carlo model in this chapter is necessary for delivering reliable results in the chapters that follow.

However, there was a big challenge to validate this model with the FPS array available. Development of such a machine was not mature enough at the time to provide repeatable performance and reliable experimental results. This was evident in Figure 3.4, Figure 3.5 and Figure 3.8 where the model systematically outperformed the FPS and the emitter array showed a non-uniform behaviour. So technically, the model did not agree with the experiments but with careful consideration of the model assumptions and educated guesses of error sources it is possible to consider the model accurate enough for the scope of this project.

Specifically, potential reasons for the disagreement of the model with the experiments were the widely spread and misaligned electron beams which in the model were assumed to be perfectly aligned and well within the limits of the collimator apertures. At the time, such a deviation from nominal beam specifications was suspected by Adaptix but it was difficult to verify or quantify experimentally. But thanks to the work of this chapter, there is now solid evidence in support of this suspicion and the level of underperformance has been quantified, helping Adaptix to estimate the technical cost of

improving the FPS. This led to the manufacturing of a new FPS array where the electron beams travelled directly towards larger collimator apertures without magnetic steering. Contrary to original designs with field emitters at a lateral offset from the collimator apertures, the new design had the emitter array aligned with the collimator array. So, there was no need for beam steering. The higher photon yield measured with this new FPS array supported the assumption that there were indeed beam losses in the original FPS due to a combination of narrower apertures and insufficient magnetic steering, very likely coupled with losses of current from the wafer to the individual emitters as shown in Figure 3.8. Space charge effects within the FPS geometry that were not taken into account in the Monte Carlo models may have been the reasons behind these discrepancies from the experiment. Moreover, assumptions about the minor effect of the angle of incidence were confirmed as shown in Figure 3.2, reducing the number of suspected factors of underperformance.

Omitting the electromagnetic fields within the FPS was a decision based on experience with the FPS performance and on its geometry and maximum energy. Adaptix had observed experimentally that back scattered electrons were absorbed several cm away from their dedicated aperture. This was expressed as hot spots of radiation damage on the FPS components, observable upon visual examination. Also, the only radiation that would be emitted from the FPS would be the photons that originated from the X-ray target and passed through the collimator aperture. These were primarily generated by the primary electron beam coming directly from the field emitters and not from electrons reaching the X-ray target after being scattered somewhere else. That is because the collimator creates a narrow solid angle for backscattered electrons to pass through and because, due to their uniform angular distribution and low kinetic energies, the probability of re-entry of scattered electrons in their aperture is negligible. Also, the angle of incidence of the electron beam was found to not have an important effect on the photon yield and due to the narrow collimator apertures and large SIDs it was expected to not have an important effect on the X-ray beam shape either so it could be modelled as being perpendicular to the X-ray target and aligned to its centre. For the same reason, the space charge effects within the FPS geometry from the various electron clouds would also not affect the shape of the X-ray beam but instead could potentially affect the photon yield. Therefore, omitting the electromagnetic fields was eventually a safe choice to remove the complexity of the code and improve efficiency without adding significant bias to the results other than an overestimation of the photon yield which was quantified.

Finally, the FLUKA and Geant4 simulations agreed on the characteristics of the X-ray beam such as shape, size and energy spectrum as shown in Figure 3.4. They also agreed in the dosimetric and attenuation properties of the beam as shown in Figure 3.5. This showed that these two fundamentally different Monte Carlo codes are equally reliable for the simulation of this novel 3D X-ray imaging technology which essentially

increased the confidence in the developed models. But these here presented models remain qualitative and a terminal and thorough validation and agreement of simulations and experiments with a robust FPS must be achieved to gain the highest confidence in a quantitative Monte Carlo model. However, the scope of Chapter 4 and Chapter 5 is well served with the qualitative models and as such they were deemed sufficient for the rest of this thesis.

3.10 Conclusion

An analytical model of the X-ray beam coming from one source on the Adaptix FPS array has been created. This model is an analytical fit of the results from detailed FLUKA and Geant4 Monte Carlo simulations of beam transport inside the source assembly that were benchmarked with experiments using actual FPSs from Adaptix.

There was an excellent agreement between the FLUKA and Geant4 results in terms of beam shape, beam size and energy spectrum so the FPS model has been successfully benchmarked using two fundamentally different codes. Many technical challenges were faced during the experiments, but the Monte Carlo results were still in good agreement with them. Also, the discrepancy between expected performance and actual performance of the FPS has been quantified and the factors responsible for it have been identified from a pool of potential sources of underperformance. So, the Monte Carlo simulation framework developed in this chapter has offered strategic insight of the Adaptix FPS technology that is challenging to get with just experimental methods. This high-value and detail insight can help Adaptix accelerate the development of their novel, portable, 3D X-ray imaging systems and bring a revolutionary technology in clinics around the world.

Finally, since the two codes are in excellent agreement between them and since the experimental beam attenuation and intensity are reproduced well in the simulations, the models are considered reliable for the scope of this thesis and will be used in the next chapters as well. But Chapter 4 and Chapter 5 include DT simulations with human phantoms based on existing Geant4 codes. Therefore, only the Geant4-based analytical FPS model will be used for DT simulations with these phantoms. The FLUKA code will instead be used only for any necessary source simulations in Chapter 5 because it offers a faster way of building the source geometry than Geant4 through its user friendly but powerful graphical user interface, FLAIR.

Chapter 4

Accuracy of the independent atom approximation in digital tomosynthesis Monte Carlo simulations

Monte Carlo methods are the gold standard for X-ray source simulations. However, Monte Carlo codes use some approximations that incorrectly model physical phenomena. Also, it is a rather challenging task to create more detailed models although not impossible. Approximations used in Monte Carlo codes have been found to affect the results of 2D X-ray imaging simulations when compared to more accurate models. On the other hand, CT simulations were found unaffected by the approximations. DT is a middle ground modality between 2D radiography and CT but there is no intuition as to how it is affected by the approximations in Monte Carlo codes. This is tested in this chapter by performing simulations of a full DT procedure of different phantoms using either approximations or highly detailed models of physical interactions. The results are used to assess whether out-of-the-box, general purpose Monte Carlo codes such as FLUKA and Geant4 are adequate for reliable end-to-end simulations of DT procedures or if more accurate but also computationally and technically expensive models need to be used.

4.1 Introduction

The renewed interest in DT systems mentioned in Chapter 1 has brought DT under extensive research with a variety of tools, the golden standard of which being Monte Carlo simulations. Despite any architectural differences, all MC codes employed must accurately model physics at the diagnostic energies of 10s keV. In most MC codes the default model for the simulation of photon coherent scattering, also known as elastic or Rayleigh scattering, is the Independent Atom Approximation Model (IAM). In the

IAM model, tissues are assumed to be made of free atoms, like a gas. This ignores any molecular interference (MI) effects that have been observed in human tissues and even in liquid water.[70] Because these effects are neglected in IAM, the calculation of the Rayleigh scattering differential cross section leads to a maximum scattering probability at 0° scattering angle.

But in reality, Rayleigh scattering in soft tissues and even in liquids is not peaked at 0° (4° for 60 keV photons in liquid water[70]). There is an abundance of experimental data in the literature from human[71] and animal tissues[72] that demonstrate single or multiple local peaks at scattering angles other than 0°. A compilation of references to such data can be found in a recent work by Paternò.[73]

In 2D X-ray imaging, MI effects are direct on the images but in CT the reconstruction process minimises their magnitude.[74,75] Specifically, 2D X-ray images of chest, pelvis and skull were found to have 5% discrepancies on scatter, mostly on anatomical edges but CT reconstruction algorithms were insensitive to this difference and produced 3D slices with discrepancies less than 10 Hounsfield Units (HU).[75]

However, DT is an incomplete reconstruction problem due to the limited angle of projections used. As such, the effect of MI on the image quality of DT cannot be extrapolated from the radiography or CT results. But on the other hand, it is important to know whether systematic errors are caused by the IAM while DT is under extensive research. So in what follows, a Monte Carlo simulation framework is given in order to estimate the accuracy of IAM against MI in simulations of DT images[1].

4.2 Methods

4.2.1 Flat panel source model

The analytical model derived by Geant4 in Chapter 3 was used to simulate the orthopaedic DT system by Adaptix shown in Figure 2.1(a). Therefore, the FPS array was simulated at 60 kV and had 45 emitters in a 7×7 configuration without the four corners and at a 1 cm pitch. All emitters were considered equivalent, so their respective X-ray beams all had the same beam shape, photon flux, divergence and energy spectrum, as listed in Chapter 3. Also, using Adaptix's nominal current value per emitter, the number of photons emitted by each source on the FPS was calculated at 2.5 billion photons. This number of photons was transported in Geant4 for each X-ray source.

4.2.2 The imaging phantoms

Two phantoms were used, namely the reference male voxel phantom by the International Committee for Radiological Protection (ICRP) report 110[77] and a user made phantom composed of primitive Geant4 solids. Specifically, the right hand of the voxel phantom

[1] Parts of this chapter have been published in the Institute of Physics' Biomedical Physics and Engineering Express.[76]

was used from the fingertips up to just above the wrist and the primitive phantom was made to resemble a broken extremity as shown in Figure 4.1.

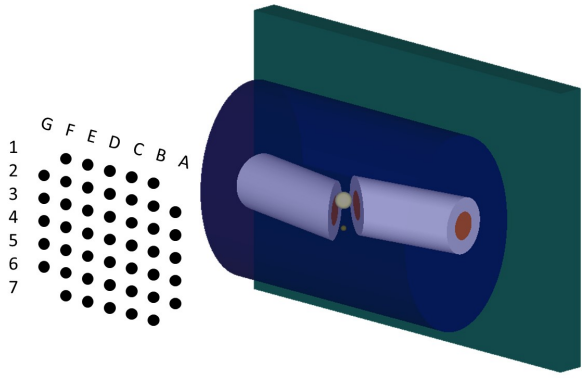

FIGURE 4.1: A phantom resembling a broken extremity placed between the source array and a flat panel detector. Source array is not drawn to scale.

The 53 tissues of the voxel phantom were grouped down to 5 based on their density as shown in Table 4.1, a method inspired by a similar 5-material voxel phantom.[75] The hand section of the phantom does not contain tissues 1 and 50 so they were not used, and all material compositions were taken from tables or assumptions in the literature,[73] listed in Table 4.1. It must be noted that the original voxel dimensions of $2.137\times2.137\times8$ mm^3 were decreased to $2\times2\times8$ mm^3. For the interests of this study, the reduction of the size is deemed unimportant. Also, this work is not about the image resolution but about the distribution of the primary and the scattered radiation. Therefore, the large voxel size is not of concern. Nevertheless, the complexity of the phantom is representative of the complexity of human tissue and that alone is satisfactory for the purpose of this study.

The second phantom is made of an elliptical water cylinder with length, minor axis and major axis equal to 10 cm, 5 cm and 7 cm, respectively. The water cylinder emulates the soft tissue inside of which there are two annular cylinders and two spheres that represent fractures of different shapes and sizes. The outer diameter of the two cylinders is 2 cm and the inner diameter is 1 cm. Both cylinders are made of healthy bone and their insides are made of osteoporotic bone. The bone cylinders are diagonally cut at one end to mimic the fracture and the two bone spheres between them act as healthy bone fragments of 6 mm and 2 mm diameter. Material compositions are shown in Table 4.1 and they are those from literature[73] that best match experimental scattering data[78] using a method suggested by Tartari et al.[74] Details of that method are presented later.

4.2.3 The flat panel detector

The simulated flat panel detector had resolution of 1500×1000 and 1500×1500 pixels for the primitive and for the voxel phantom, respectively. Therefore, the detector was 15×10 cm^2 and 15×15 cm^2 in each simulation. Every pixel summed the number of the incident photons in it, weighted by the cosine of their angle of incidence which created a

TABLE 4.1: Materials used for the two phantoms and their percent decomposition in a compound of four materials [74] as matched or compared by Paternò [73] to experimental data. The 53 tissues of the ICRP110 reference adult male phantom are grouped into 5 based on their density. The left hand of the voxel phantom does not include tissues 1 and 50 so they are not used. Tissue 53 is air.

	Fat	Water	Bone Matrix	Hydroxyapatite	References
Geant4 phantom					
Tissue					
Soft tissue	100				
Bone and bone fragments	36	15	13	36	Normal bone [78]
Bone marrow	55	25	5	15	Osteoporotic bone [78]
Left hand of the ICRP 110 reference adult male voxel phantom					
Tissue number					
22-25 49	83	17			Adipose tissue [71]
17 18 20 21 27-48 51 52	15	73	12		Muscle [79]
3-16 19 26	80	20			Yellow marrow assumption matching femoral head [80]
2	22	22	19	37	Bone [79]

2D map of the cosine weighted photon fluence. This map was transformed to greyscale images with a method described below.

A distance of 5.6 mm between the detector and the phantoms was used to simulate the distance between the detector surface and the detector active layer.

4.2.4 Modelling molecular interference

To investigate the difference on the image caused by more realistic MI effects on diagnostic X-ray coherent scatter, the user source code was linked with a recently published extension that implements these effects in Geant4. [73,81] This extension allows the user to either activate coherent scattering MI effects on a set of specific tissues and materials for which MI data are available or to define a tissue as a compound of water, fat, bone matrix and hydroxyapatite. The code then calculates the MI data of the compound by using the MI data of the four materials according to a method described by Tartari et al. [74] This method changes the coherent scattering differential cross sections but the extension used here [73,81] also integrates them to further recalculate the total scattering cross section. By activating or not MI effects, the difference on the DT image quality between the two models can be estimated.

On the other hand, FLUKA uses the IAM and there is no extension currently to include MI. This essentially drove the decision to use only the Geant4-based model in Chapter 3.

4.2.5 Image processing

Prior to the image acquisition, 45 projection images without the phantoms in place were simulated with the same number of photons as would be simulated with the phantoms in place. These air shots were used to calculate the pixel-wise attenuation images, μ. These were defined as the natural logarithm of the ratio of the air shot, I_0 over the phantom shot, I, according to the Beer-Lambert law, μ=ln(I_0/I). These 45 attenuation images were the input for the DT reconstruction algorithm.

μ is a real number. It is negative in pixels that collect more photons after the beam scatters in the phantom, as photons are redirected to pixels where they would not normally arrive from an air shot; $I_0 < I$. μ is positive in pixels that, due to scattering, receive fewer photons with the phantom than with the air shot; $I_0 > I$. Theoretically, μ can also be zero in pixels where the beam intensity has not changed with the inclusion of a phantom, so $I_0 = I$, but practically this never happens due to the stochastic nature of photon emission and interaction in air and tissues. In the clinic, air shots are preloaded on the system or taken during the various standard calibration procedures, without interfering with the patient's scan.

The DT reconstruction algorithm accepts various data formats, but this study used uncompressed PNG images. Therefore, the 2D attenuation images with negative and positive float numerical data were converted to 16-bit greyscale PNG images. A user Python script scanned all 45 attenuation images and created a single histogram with the frequency of their pixel values. This was done separately for the IAM and the MI images. The lower 1% and higher 99% bins of the two histograms were then used to define the greyscale's white and black ends.

To use the same greyscale for both IAM and MI generated attenuation images, the same white and black ends had to be used. If between the IAM and MI histograms, the minimum 1% mark was a positive number, this number would be the black end of the greyscale for both models otherwise zero was used. For the white end, the 99% margin caused brightness saturation on the projections from the outer sources, so instead the 99% value was scaled by 1.2 and that value was used for the white end. The 99% margin used was the maximum between that of IAM and MI histograms. With this method, all 45 attenuation images created with both scattering models were converted to grey images with the same greyscale. Greyscales were different only between the two phantoms.

4.2.6 Digital tomosynthesis

The reconstruction algorithm used in this study is a modification of the filter of back projections.[61] In contrast to the filtered back projection algorithm, the back projection comes first and the filtering follows. It differs from the original filter of back projections suggested by Bates and Peters[82] in that respect that the ramp filter is applied over planes (slices) parallel to the flat panel detector, while the original one performs filtering over the planes perpendicular to the detector with parallel rays illumination. In this case

the ray tracing technique, which is usually employed for computing back projections, is replaced with an equivalent image mapping procedure. Thus, attenuation images are mapped at a particular height above the detector and their average is fed to the ramp filter. The cone beam geometry is taken into account by the image mapping procedure.

This approach is well suited to the DT geometry. It does not require three-dimensional grid or mesh allocation for storing reconstruction results. Moreover, it performs a user interactive, slice-by-slice reconstruction where each slice position can be chosen at runtime. This allows the display of reconstructed slices on the fly as soon as they are available. The reconstruction slice order can be arbitrary, thus, allowing the most relevant slices to be reconstructed and displayed first.

Contrary to CT, DT reconstructs slices from a set of projection images taken over a limited angle range. Therefore, the inverse problem suffers from incompleteness of data. This incompleteness manifests itself in the appearance of negative numbers and poor image quality. To address this issue, the reconstruction problem must be regularized. [83]

When the reconstruction is performed in the Fourier domain, an addition of a small number to the ramp filter $|k|$ (truncated at the maximum allowed value of the wave number) has a regularization effect. Its value is about a few sizes of the reciprocal lattice cell. Alternatively, filtering can be done by computing a convolution of the average of mapped images with the spatial analogue of the ramp filter over the finite window. Reduction of the size of the convolution window has a regularization effect. [61] Finally, the reconstruction algorithm allows the user to choose a resolution for the DT slices different to that of the input 2D X-ray images. In this study, the resolution of the slices was reduced by a factor of 2 to speed up the reconstruction and regularisation was performed by convolution of the mapped images.

4.2.7 Comparison of results

The projection images (phantom shots) generated by the simulation were compared pixel-by-pixel using a Python script to find the relative difference caused by the two scattering models on the distribution of primary and scatter radiation. This allowed comparison of the results with literature on the differences found in planar X-ray images. [75] The same comparison was then done on the grey scale 2D attenuation images and on the reconstructed 3D DT slices to calculate the relative difference on the pixel grey scale values.

4.3 Results

The difference between IAM and MI in the spatial density of primary and scattered photons for one of the 45 projections of the voxel phantom is shown in Figure 4.2. The figure shows single and multiple scatter components of both coherent and incoherent scattering. The difference between IAM and MI in scatter density was within 5% and was most profound at the edges, which agreed with literature.[75] The structure of the phantom was visible in the difference of the single coherent scatter, but it was lost in the rest of the scatter components. Also, the highest relative differences were found in the coherent scatter, both single and multiple, and the recalculated total scattering cross section had induced a small difference in the primary radiation too. However, the difference in the total radiation remained low. This can be explained by the fact that with both models, the primary (not scattered) radiation formed 90% of the detected radiation, the single coherent scatter formed less than 3% and the multiple coherent less than 0.2%. Finally, the projection in Figure 4.5 was from a source on the top right(A2, Figure 4.1), so the higher differences at the bottom left of the image, mostly visible in the primary radiation, were due to the high statistical noise of the penumbra.

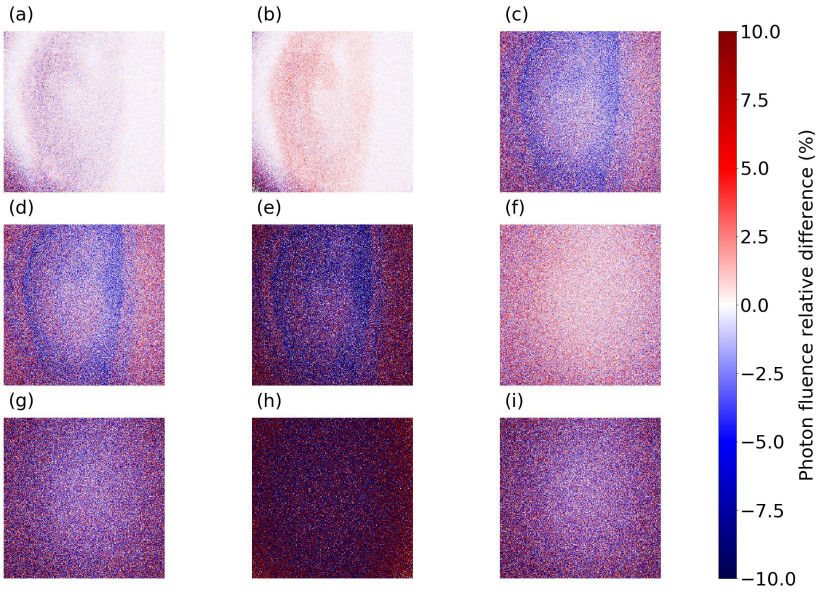

FIGURE 4.2: Difference in the various radiation components between IAM and MIA Rayleigh scattering models when the A2 source irradiated the voxel phantom. a) total, b) primary, c) scatter, d) total single scatter, e) single coherent scatter, f) single incoherent scatter, g) total multiple scatter, h) multiple coherent scatter, i) multiple incoherent scatter. Images were binned with a 4×4 kernel prior to calculation.

The same information for the primitive phantom is shown in Figure 4.3. Simulations agreed with the literature regarding the scatter density differences between the two models. The difference in the primary radiation was higher than in the voxel phantom but the difference in the total radiation remained close to 3%. With both models, 90% of the radiation was primary photon flux, single coherent scatter was below 3% and the

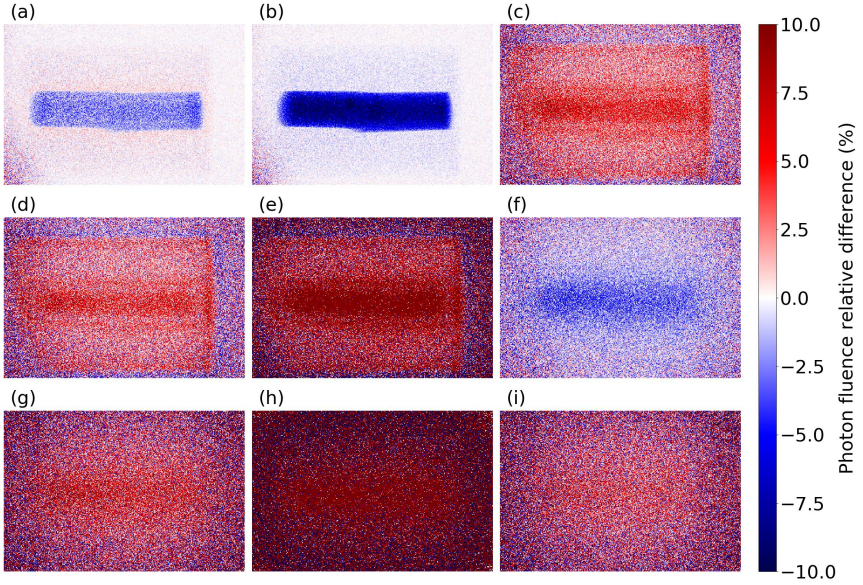

FIGURE 4.3: Difference in the various radiation components between IAM and MIA Rayleigh scattering models when the A2 source irradiated the primitive phantom. a) total, b) primary, c) scatter, d) total single scatter, e) single coherent scatter, f) single incoherent scatter, g) total multiple scatter, h) multiple coherent scatter, i) multiple incoherent scatter. Images were binned with a 4×4 kernel prior to calculation.

multiple coherent scatter formed less than 0.2%; this explained the small difference in the total radiation. Moreover, this detector was 5 cm shorter on the vertical axis so the penumbra on the bottom left was not as visible as before but the larger thickness of this phantom in the beam direction caused cropping on the bottom left of the difference in the scattered radiation.

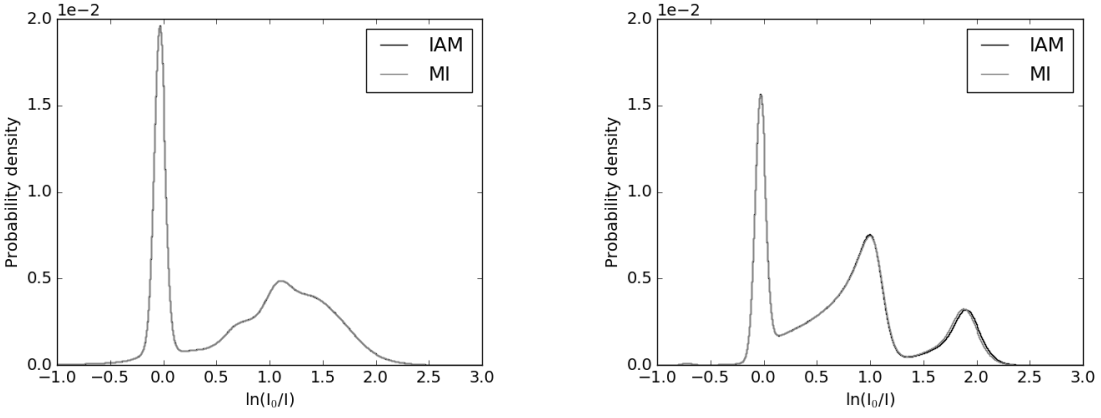

(a) (b)

FIGURE 4.4: Pixel value distributions of the attenuation images of the two phantoms with the two Rayleigh scattering models. The distributions are for values among all 45 emitters and they are practically identical. a) voxel phantom, b) primitive phantom

The distributions of the pixel values in all attenuation images after using the IAM and MI scattering models are shown in Figure 4.4. Both models produced a practically

identical distribution of pixel values with both phantoms apart from a small difference after 1.5 for the primitive phantom. The peak at zero in both figures corresponded to pixels not behind the phantoms while negative values were due to scattered radiation as explained in 4.2.5. The clearly defined peaks of the primitive phantom at 1 and 1.9 were from pixels behind the water cylinder and behind the bone cylinders, respectively. On the contrary, the higher complexity of the voxel phantom produced convolved peaks.

From Figure 4.4, the voxel phantom attenuation images resulting from both scattering models were converted to 16-bit greyscale PNG images using a linear scale with white and black ends at 0 and 2.43, respectively. Similarly, the attenuation images of the primitive phantom were converted with ends at 0 and 2.52. Examples of PNG attenuation images of both phantoms and with both Rayleigh scattering models are shown in Figure 4.5 and Figure 4.6. All images are illustrated with their respectively allocated grey scales. As intuitively expected from the radiation distributions in Figure 4.2 and Figure 4.3, the IAM and the MI scattering models did not cause a visually obvious difference in the X-ray attenuation images. Calculating this difference revealed a discrepancy of less than 4%.

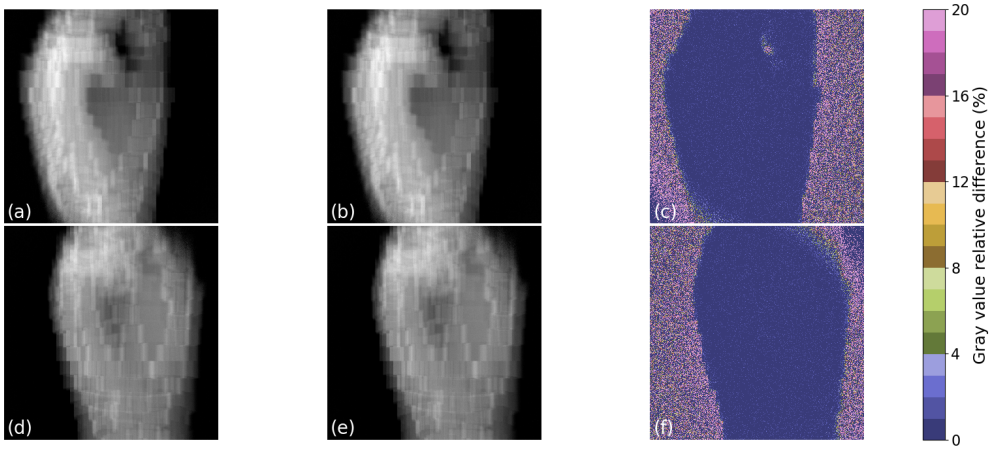

FIGURE 4.5: Attenuation images of the voxel phantom and their absolute percentage difference caused by using either IAM or MI. a) using IAM and b) using MI are images generated by the A2 source, c) relative difference of a-b. d) using IAM and e) using MI are images generated by the G6 source, f) relative difference of d-e. Dark spot in a) and b) was due to the alignment of the X-ray beam with a gap within the curled fingers. Images were binned with a 4×4 kernel prior to calculation of their difference. Differences appeared minor and only black areas caused large deviations due to operations with very small numbers.

The signal to noise ratio (SNR) of a 200×200 pixel region was measured just above the wrist and at the fingers in the greyscale attenuation images of the voxel phantom. The SNR of an 80×80 pixel region was measured on the top left side of the water and in the centre of the left bone in the images of the primitive phantom as well. Due to the different projection angle, the region was manually placed per image to follow the shift of the phantom's projection on the detector. However, the position of the regions was identical between MI and IAM models. Results are shown in Figure 4.7.

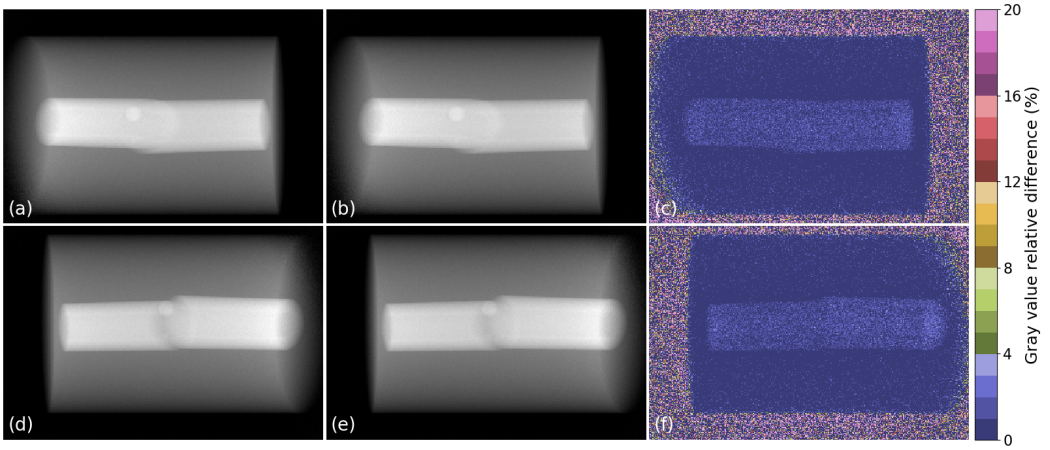

FIGURE 4.6: Attenuation images of the primitive phantom and their absolute percentage difference caused by using either IAM or MI. a) using IAM and b) using MI are images generated by the A2 source, c) relative difference of a-b. d) using IAM and e) using MI are images generated by the G6 source, f) relative difference of d-e. Images were binned with a 4×4 kernel prior to calculation of their difference. Differences appeared minor and only black areas caused large deviations due to operations with very small numbers.

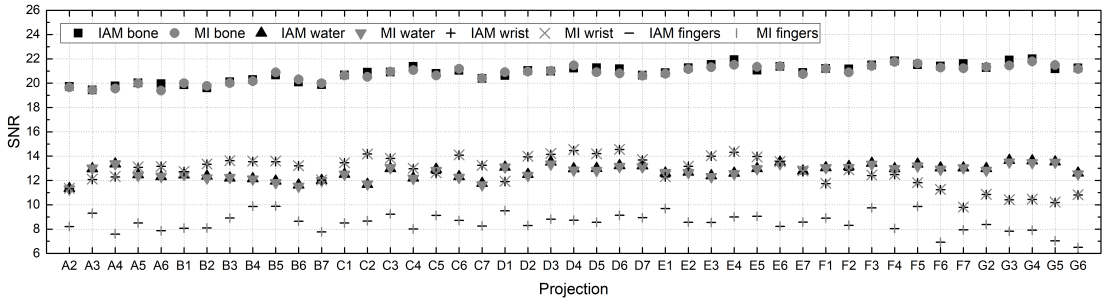

FIGURE 4.7: SNR of various areas in the 2D X-ray projections with both scattering models. Projections are named after the source that produced them. The effect on the SNR due to a change in the scattering model was smaller than the symbol size. Changes on an image-by-image basis were due to the different projection angles and the manual way of placing the area in which the SNR was calculated.

Each projection is named after the source that generated as illustrated in Figure 4.1. The two models barely changed the SNR in the attenuation images. The SNR difference among the projections was due to the change in projection angle and the manual positioning of the regions during the calculation.

Finally, slices from the reconstructed volumes of both phantoms are shown in Figure 4.8 and Figure 4.9. There was no visually obvious difference and by calculation it was found lower than 4%. Only dark areas showed values above that value, an obvious result of numerical precision effects. Also, as shown in Figure 4.10, the SNR of various areas on slices of the two phantoms was affected by less than 2% by adding or removing MI effects. These areas were on structures that were in focus in the selected slices. Each slice brought different structures in focus therefore intra slice comparison was meaningless.

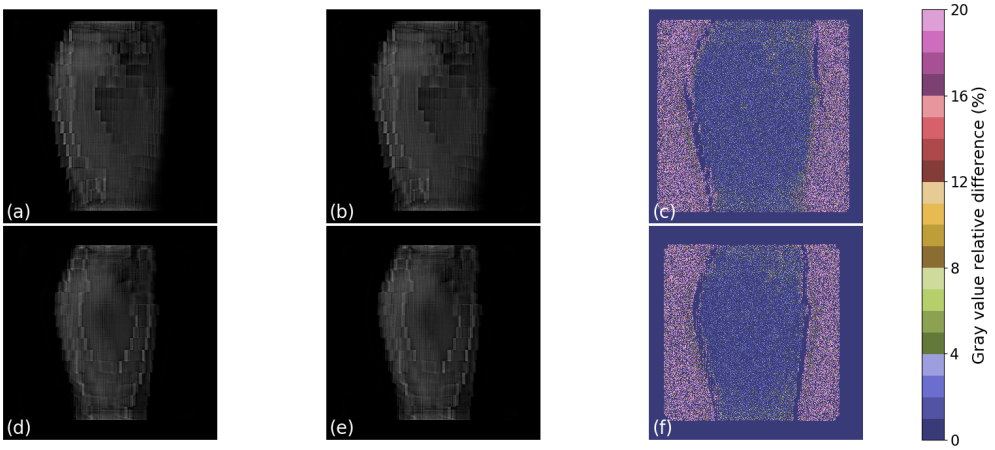

FIGURE 4.8: a, d) two DT reconstructed slices at different depths in the voxel phantom using the IAM model. b, e) the same slices using the MI model, c) relative difference of a-b, f) absolute relative difference of d-e. Voxels that contain the phantom have a discrepancy mostly below 4% while dark voxels have discrepancies above that. A zone of zero difference surrounding the phantom came from the reconstruction algorithm. The same applies for the rectangular frame of zero difference on the outermost regions of the slices. The reconstruction algorithm reduced the image dimensions by half to speed up the process and resulting images were binned with a 2×2 kernel prior to calculation of their difference.

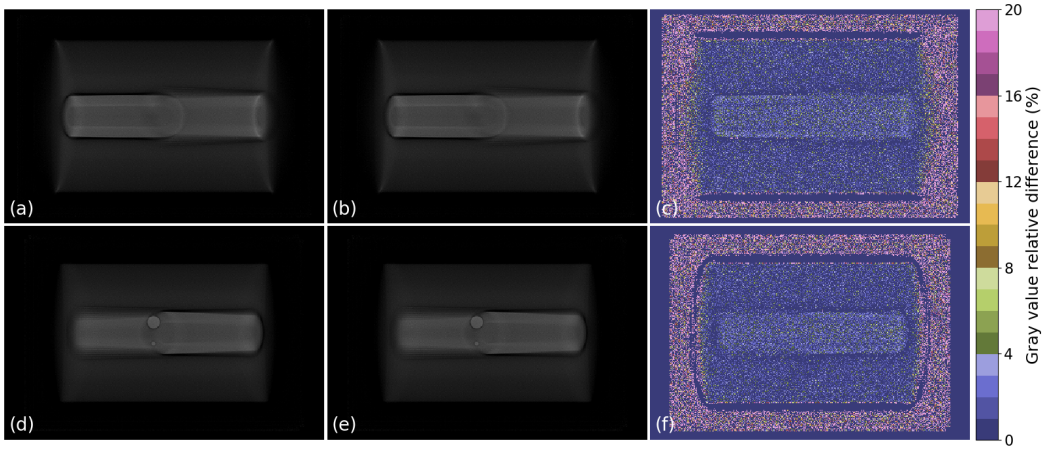

FIGURE 4.9: a, d) two DT reconstructed slices at different depths in the primitive phantom using the IAM model. b, e) the same slices using the MI model, c) relative difference of a-b, f) absolute relative difference of d-e. Voxels that contain the phantom have a discrepancy mostly below 4% while dark voxels have discrepancies above that. A zone of zero difference surrounding the phantom came from the reconstruction algorithm. The same applies for the rectangular frame of zero difference on the outermost regions of the slices. The reconstruction algorithm reduced the image dimensions by half to speed up the process and resulting images were binned with a 2×2 kernel prior to calculation of their difference.

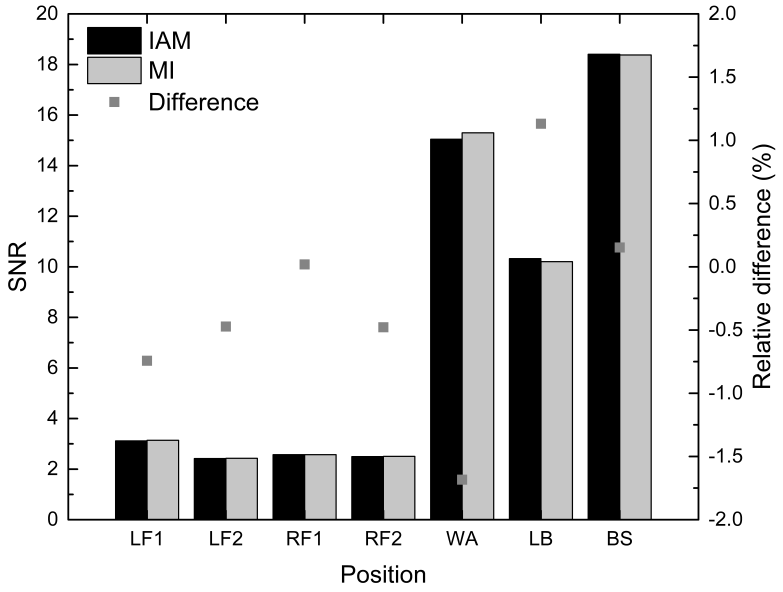

FIGURE 4.10: SNR of various tissues that are in focus in Figure 4.8 and Figure 4.9. LF1 and LF2 are two 50-pixel wide squares on the left finger; RF1 and RF2 similarly on the right finger. WA is a 40-pixel diameter area in the water above the left bone, LB in the centre of the left bone and BS in the large bone sphere.

4.4 Discussion

In these simulations it was decided to use a pixel size of 100 μm, a low flux per projection and an arbitrary way of converting photon flux to pixel value for the following reasons. There was a minimum distance of 5.6 mm between the phantoms and the active layer of the detector. With a Rayleigh scattering peak at 4° for 60 keV photons in liquid water,[70] these scattered photons would be expected at a minimum offset of 329 μm. Also, bone has multiple peaks in a wide range of momentum transfer values that includes that of liquid water.[73] Therefore, 100 μm pixels are small enough to resolve these photons when binned by 4(effective size 400 μm). Also, the average energy as shown in Figure 3.4 is lower than 60 keV therefore most photons would be scattered with a wider angle, making 400 μm effective pixels wide enough to resolve them.

The photon yield from the FLUKA simulation has been compared with Geant4 simulations and with dose rate experiments in Chapter 3 and there was enough confidence that the expected photon flux was estimated well. But the projections were noisy due to the inherently low flux of this system. This could add doubts regarding the validity of these results in a higher flux and thus less noisy procedure. However, in Figure 4.2(a) the colour map was uniform close to 0% difference while in Figure 4.3(a) the cold area of the bone cylinders in the total radiation was below 5%. This simple geometry was unrealistic so based on Figure 4.2 with the complex and more realistic voxel phantom, increasing the photon flux should not change the conclusions.

As was mentioned above, the reconstruction problem is incomplete. In general, the regularization affects the SNR and the image contrast.[83] If one considers the reconstruction in the Fourier domain, a value of the regularization parameter smaller than optimal usually provides reconstructed images of higher contrast but with lower SNR. For example, a small value amplifies the noise, which is intrinsically present in attenuation images, whilst a larger than the optimal value produces smoother images, but with a stronger background component. In many cases only an approximation for the optimal value can be found. The same is true for the width of the window when the reconstruction is performed spatially by convolution, which was the method used here. Nevertheless, the image quality is usually acceptable when the SNR is greater than 10, which implies that the noise level in reconstructed images can even reach 10%. Therefore, variation of the noise level below a few per cent due to approximations made in a physical model are not important in terms of the reconstruction. In addition, computational techniques for noise suppression make small variations in the noise level caused by the choice of a physical model even less important.

Although arbitrary, it is not uncommon in the literature to use cosine weighted photon fluence as the signal for simulated images and the decision to use the 99% margin in Figure 4.4 multiplied by 1.2 as the white end avoided brightness saturation in the projections. The shade of these projections as shown in Figure 4.5 and Figure 4.6 was similar to what is observed in the laboratory and what is found in literature. As such, this methodology was reasonable but also straightforward to understand and implement. However, digital breast tomosynthesis (DBT) uses much lower energies than this work. At those energies and with vast ranges of breast thickness and composition, the scatter-to-primary ratio (SPR) can be different from the 1:9 observed here. More importantly, the portion of the single coherent scatter could be higher and as shown in Figure 4.2 and Figure 4.3, this holds spatial information about the imaged subject. So, there could be situations where there is a larger component of single coherent scatter which carries structural information that is inaccurately modelled and with this inaccuracy being propagated to the image quality even after a DT reconstruction. This could also deteriorate scatter correction methodologies based on Monte Carlo scatter estimations. Therefore, the here-presented conclusions cannot be intuitively extrapolated to DBT. Thankfully, this is trivially addressed on an *ad hoc* basis by simply identifying combinations of energy spectrum, tissue thickness and composition that have higher ratios of single coherent scatter to total radiation. If a manufacturer or medical physicist finds their equipment to be in that situation, they can test whether the IAM produces different image estimations compared to the MI model. Otherwise, the random nature of the other scatter components diffuses the information carried by the MI corrected coherent scatter making the corrections obsolete and the IAM model adequate.

4.5 Conclusion

The recent heightened academic and commercial interest in developing DT imaging systems has brought attention to MC radiation transport literature where the accuracy of commonly used MC photon scattering models such as the IAM had been challenged. Conclusions so far had been drawn for planar X-ray imaging and for CT, the former requiring more accurate MI effects to be included in the models and the latter being sufficient with the IAM. In this chapter, the above conclusions were complemented by proving that DT algorithms are also insensitive to physical effects, like their CT counterparts. Therefore, multipurpose Monte Carlo codes that use the IAM are adequate for the simulation of DT imaging systems. This conclusion is limited to DT with low SPR. However, it is trivial to estimate the SPR of different DT scenarios such as DBT. If SPR is similar to or lower than what was observed in this study, then the IAM should be sufficient. Otherwise, the Geant4 extension by Paternò[73] can give estimates of model discrepancies on an *ad hoc* basis. Due to chest imaging having higher SPR than this example, the study of chest DT in Chapter 5 can be done with default Geant4 code.

Chapter 5

Upgrading the flat panel source to allow stationary chest tomosynthesis: a Monte Carlo study

The line of Adaptix DT systems comprises orthopaedic, dental, veterinary and NDT imaging devices. The company is now expanding their portfolio into low-dose, low-cost chest DT. This requires the upgrade of the current FPS technology to versions with higher voltage, higher current and more emitters because of the thicker volume and larger surface area that needs to be imaged. Before time, money and resources are invested into building the new FPS, a detailed characterisation of the upgrade is necessary and this is best performed using Monte Carlo simulations. In this chapter, the concept upgrade of the Adaptix FPS is modelled using Geant4, based on the FPS models developed in Chapter 3 and different FPS upgrades are simulated and compared with each other in terms of source performance, image quality and patient dose. The outcome of this study is a thorough understanding and confirmation of regulatory compliance of an extensive set of candidate upgrades of the Adaptix FPS which is information that has already been used to make decisions about chest DT FPS specifications. This has given Adaptix a critical head start to the development of this new device and in combination with the multi-FPS studies presented in Chapter 6, the results of this chapter have greatly accelerated the introduction of the new line of Adaptix multi-FPS chest DT systems.

5.1 Introduction

So far, in Chapter 3 and Chapter 4 a flat panel X-ray source simulation framework has been developed and its validity has been confirmed by comparing it with different Monte Carlo codes and experimental data. The estimated X-ray source performance, image quality and physics interaction models were found reliable for simulating the Adaptix

FPS which is still under development. This also means that the simulation framework could be used with a good level of confidence to reproduce the performance of conceptual upgrades to the FPS and to use those to find design and optimisation solutions at an early stage of development. As shown in Chapter 3 and Chapter 4, Monte Carlo simulations can provide insight that is challenging or impossible to get experimentally so studies like this can significantly narrow down design and manufacturing decision trees way before activities commence in the laboratory. Identifying dead ends before resources and time have been invested can accelerate research and drastically reduce the cost of development, essentially bringing portable DT to the clinic faster and at a lower price.

Going back to the technicalities of DT, 3D imaging modalities such as CT and DT typically scan the patient from different angles with a lengthy mechanical movement of a single X-ray tube. Therefore, millions[1] of 3D scans per year require expensive mechanisms to support the heavy X-ray source and have to correct for machine vibrations and patient movements. However, the cold-cathode field emission technology inside Adaptix's FPS allows the creation of compact, stationary arrays of emitters and has already been used successfully in dental, orthopaedic, veterinary and non-destructive testing applications.

This chapter[1] presents Monte Carlo simulations of an upgrade to the Adaptix FPS array from 60 kV to 90 kV and 120 kV which are instead better suited for chest imaging. Different X-ray target thicknesses and accelerating voltages are investigated and combinations are compared in terms of their resulting photon yield, energy spectrum, patient dose and image quality. The upgraded FPS would be used for chest DT with portable imaging systems that are compact, lightweight and that could require less input power compared to X-ray tube-based systems. Such characteristics could bring FPS-based DT systems to the patient's bedside for true point-of-care 3D imaging. A detailed account of the benefits of compact, portable and low input power specifications in medical imaging can be found in Chapter 1.

5.2 Methods

5.2.1 The two-step method

In this study, electron and photon transport needs to be simulated inside 25 X-ray sources where photons are generated after electron emitters fire electrons towards an X-ray target. Then, the 25 resulting X-ray beams need to be transported through the torso of a human phantom. Due to the inherently low photon yield from these types of X-ray sources, as well as the attenuation through the human phantom, it would be extremely inefficient to do all that in a single Monte Carlo simulation. Therefore, a two-step method was preferred.

[1] Parts of this chapter have been published in the Institute of Physics' Biomedical Physics and Engineering Express.[43]

In the first step the photon spectrum of each of the 25 X-ray sources was scored. The X-ray sources were assumed to be identical so only one was simulated. In the second step, the 25 X-ray sources were replaced by 25 user defined X-ray cone beams that had the energy spectrum from the first step. Because the X-ray sources were identical, the user defined X-ray cone beams were also identical. During the second step, each X-ray beam was transported through a human phantom and the primary beam and any produced scatter were detected by a flat panel imaging detector. Dose to the patient was also scored during that step. Details of both steps are given below.

FLUKA was used to perform the first step because it offered a much quicker way to set up the X-ray source geometry and Geant4 was used for the second step because it offered a direct means of importing the human phantom.

5.2.2 X-ray source simulation

The concept upgrade of the Adaptix system has a flat panel emitter array with 25 emitters, in a 5×5 configuration with 2 cm pitch as shown in Figure 5.1(a). X-rays are generated inside the X-ray target when it is bombarded with electrons from each of the 25 emitters as shown in Figure 5.1(b). In this chapter just a single such panel is modelled for simplicity, shown in Figure 5.2(a-b), even though the full product version is likely to use multiple, angled panels for optimal illumination similar to what is shown in Figure 5.2(c).

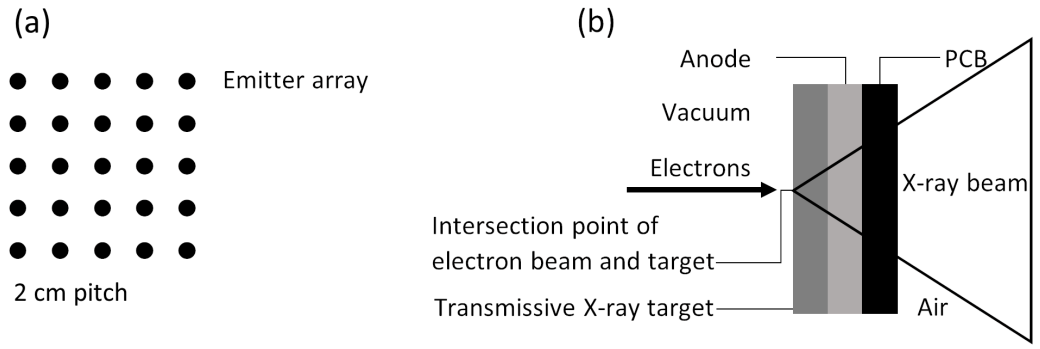

FIGURE 5.1: (a) The emitter array configuration, (b) the source assembly of a single emitter as it was simulated in FLUKA. Illustrations are not drawn to scale.

For simplicity, all electron emitters were considered equivalent therefore for the same accelerating voltage, all 25 X-ray beams were identical. Therefore, simulating one X-ray source would characterise the whole X-ray source array. The X-ray source includes the transmissive X-ray target, collimators and various filters but for simplicity, only the components that have a major effect on the beam energy spectrum were included in the simulation. Therefore, the electron emitter cathode, collimators, wires and plastics were omitted and a FLUKA X-ray source model was built as shown in Figure 5.1(b) which included only the X-ray target and the anode while the Printed Circuit Board (PCB) was added as well due to the Cu that it contains. The distances between components

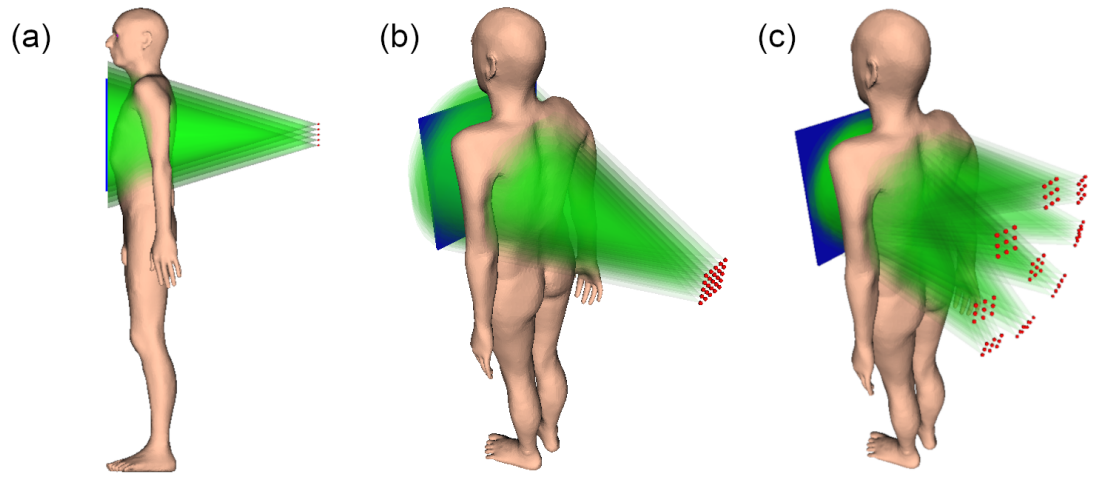

FIGURE 5.2: The irradiation geometry of the current study with the single flat panel source array (a, b) and of a concept irradiation geometry with a multi-panel system (c). Emitters are activated sequentially but here they are all drawn simultaneously active for illustration purposes. The multi-FPS system was designed by Ipioni, the Python application described in Chapter 6. Schematics drawn in FreeCAD. [84]

were also neglected and so they were stacked in the model but their thicknesses were reproduced according to their real dimensions. A gaussian electron pencil beam with 100 μm width was transported towards the source geometry and the resulting photon spectrum that escaped the PCB was scored. The electron beam was monoenergetic at either 90 keV or 120 keV for the 90 kV and 120 kV system respectively. The photon energy spectrum was scored for 4 different target thicknesses between 3 μm and 6 μm so a total of 8 spectra were generated.

The range of target thicknesses was selected based on the efficiency of photon generation and the robustness of the target against radiation damage. Narrow targets have a low photon yield and are more susceptible to radiation damage but thicker targets absorb more of the photons that are generated in them. Therefore, there exists a target thickness where photon yield and target robustness reach an optimum balance.

For the photon yield, this optimum thickness is different for different energies as shown in Figure 5.3. These are results of a FLUKA simulation where monochromatic electron pencil beams were transported towards a 20 μm Ta target. The forward-facing photon density at different depths in the target shows that higher energies have higher optimum values for target thickness and that the photon yield increases with the electron energy regardless of target thickness apart from the build-up region at the start of the curves. The spikes found in some of the curves are from values with high statistical error and could have been removed if more electron primaries were simulated. However, the general trend was already clear and it was decided to estimate the energy spectrum and the photon yield of the full source geometry using target thicknesses between 3 μm and 6 μm for both 90 keV and 120 keV. The PRECISIO card and the minimum allowed energy cut off of 1 keV for electrons and 100 eV for photons were used in FLUKA for

the X-ray source simulations and the electron beam had a 2D gaussian shape with 6σ=100 μm and was normal to the X-ray target.

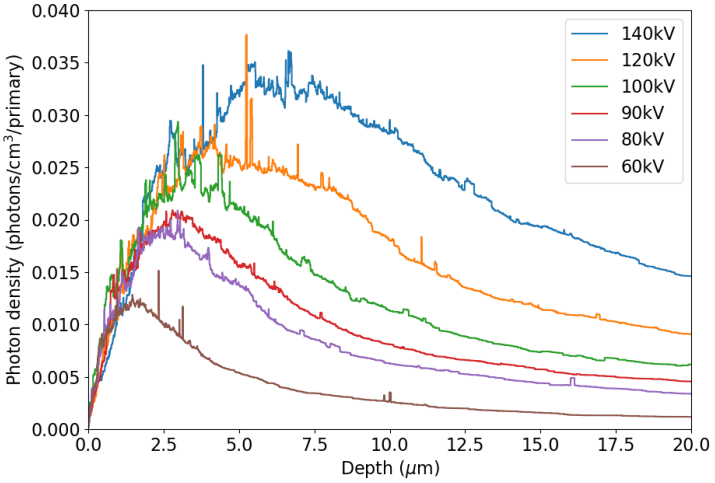

FIGURE 5.3: Forward facing photon density versus electron energy and depth in Ta. The spikes found on each spectrum are statistical noise.

5.2.3 Chest tomosynthesis simulation

X-ray beam model

Identical X-ray cone beams were defined in Geant4 to simulate the propagation of photons towards the patient and the detector. These were defined by the model built in Chapter 3. Each cone beam was positioned with its vertex at the intersection point of the respective electron beam with the X-ray target as shown in Figure 5.1(b) and the X-ray source geometry from the first step was omitted.

The beam size was set so that the X-ray field at the detector was large enough that the four corner X-ray beams fully covered the respective corner on the detector. To accomplish that using the model from Chapter 3, the virtual origin on the X-ray target was shifted along the beam direction while the position on the PCB was left unaltered. The radius of the beam was defined as the distance between the centre of the beam core and the start of the penumbra so each corner of the detector was fully irradiated by the beam core of the respective corner X-ray beam. In the original beam radius model shown in Figure 3.4(a), the edge of the beam core and where the penumbra started was close to the radius with a squared value of 0.3 cm^2. This value was chosen in the following calculations to represent the *de facto* edge of the beam core because it was close to where the beam core ends and because it was a round value that made for elegant calculations.

The distance of each corner source from the respective corner on the detector was 24.75 cm. So, the new X-ray field ought to have a beam core with a radius equal to that value. Using round numbers again, the distance of the virtual origin on the X-ray target

and the PCB had to be scaled from the original 11.25 mm to:

$$d = \frac{\sqrt{0.3\,\text{cm}^2}}{24\,\text{cm}} \times 80\,\text{cm} = 18.257\,\text{mm}$$

So in Geant4, photons were sampled using the analytical fits of Table 3.2 but to sample the photon direction, the virtual origin of the photon was at (x',y',z')=(0,0,-18.257) in mm. The unit vector between the photon position (x,y,z)=(x_0,y_0,0) and the photon virtual origin was the photon direction. This[2] made the beam core diameter 48 cm. In that way, the minimum field size was found that allowed all pixels to be illuminated by the core of at least one beam. This geometry was preferred due to its simplicity but obviously led to stray radiation outside the detector as shown in Figure 5.2(a, b). Plans to optimise the irradiation geometry are discussed at the end of this chapter and in Chapter 6 but this geometry already served its purpose for this proof of concept.

The energy spectrum of the beam was the same for both the beam core and the penumbra. Among the 4 pairs of spectra generated by FLUKA, one pair was chosen to define the energy spectrum of the 90 kVp and the 120 kVp system.

Finally, 2.5×10^9 photons were transported for both energies as in Chapter 4 which resulted in low errors during dosimetry in the phantom and also generated smooth images that resembled experimental ones.

Virtual phantom

The adult mesh type reference male phantom from the ICRP report 145 [85] shown in Figure 5.2 was used in the simulation as the imaging subject. It was chosen because it is a high-resolution, whole-body phantom with segmented organs so it allows both image quality tests and organ dosimetry. It is comprised of millions of tetrahedra with various sizes, each belonging to a specific organ, with each organ having a specific material composition. The lungs do not include the bronchi and bronchioles after the two primary bronchi but have a uniform density and material composition. Also, organ walls such as the skin, the stomach and the urinary bladder have explicit radiosensitive and non-radiosensitive layers for a more accurate calculation of effective dose.

Imaging

The imaging detector was a 2D plane placed 80 cm away from the source array as shown in Figure 5.2(a, b), much closer than the ∼2 m distance used with conventional, rotating-X-ray-tube DT systems. [86] The 80 cm SID was used because the system is purely for tomosynthesis and not for creating conventional 2D images (where a larger SID reduces magnification effects). The shorter SID also means that an X-ray source with lower input power can create the same photon density at the detector.

[2] Due to the simplifications in the calculation, the diameter of the *de facto* beam core ended up being 1.5 cm smaller. This was deemed unimportant for the scope of this chapter and it was left as is.

The 2D detector plane was square with 43 cm sides and its centre lay on the same axis with the source array centre and the approximate centre of the phantom's chest. The simulated detector plane represented the active layer of an imaging detector so a 5.6 mm distance was added between the phantom and the simulated detector plane to emulate the distance between detector surface and detector active layer of a real detector. The detector plane was parallel to the source array plane and was divided in an 860×860 pixel grid, resulting in 500 μm resolution. Each pixel counted the number of photons that were incident on it, normalised by the angle of incidence. 500 μm is a common pixel size for CT systems whereas there are flat panel detectors that could be used with this chest DT system with 160 μm pixel size.[37] However, due to the heavy computations and the multiple X-ray beams that must be simulated, a 500 μm size was preferred to allow improved pixel statistics within reasonable time.

The 25 X-ray projections were normalised on a pixel-by-pixel basis with respective images without the phantom in place and with the same amount of photon flux. Attenuation images were then generated by calculating the natural logarithm of the normalised pixels and these were converted to 16-bit uncompressed greyscale PNG images using the method from Chapter 4. These PNG images were input to a digital tomosynthesis reconstruction algorithm[61] that generated coronal 3D slices of the phantom. The algorithm could create slices of arbitrary spacing so 5 mm were chosen, similar to previous work that investigated the detectability of lung nodules with 5 mm DT slices.[10]

Dosimetry

The dose in the organs was scored for each projection and the effective dose of the whole scan was calculated according to the ICRP report 103.[87] The radiation used is only composed of photons and electrons therefore organ equivalent dose is the quotient of the imparted energy in the organ and the mass of the organ. Also, because the phantom organs/tissues are composed of different tissue sites (two kidneys, multiple muscles, multiple bones etc.), the equivalent dose to an organ/tissue that is composed of multiple sites is calculated as the quotient of the total imparted energy on all the sites and the total mass of these sites. This is not the case for the remainder tissues where the individual dose to each of the 13 is calculated as mentioned before but the equivalent dose to all of them is calculated as the arithmetic mean of their individual doses. Table 5.1 gives a summary of these methods and of the different organs/tissues and tissue sites of the ICRP 145 phantom[85] used for the estimation of the effective dose.

TABLE 5.1: Organs/Tissues with their weighting factors wT for the calculation of effective dose according to ICRP report 103 [87] and the methods used in this work to calculate the organ/tissue equivalent dose with the different organ/tissue sites of the adult mesh type reference male phantom from ICRP report 145. [85]

Organ/Tissue	wT	Organ equivalent dose calculation method	Phantom organ/tissue site ID used for the equivalent dose calculation
Bone marrow (red)	0.12	KERMA to spongiosa sites [77]	1400 2500 2700 2900 4000 4200 4400 4600 4800 5000 5200 5400 5600
Breast		Total imparted energy to glandular breast sites divided by their total mass	6300 6500
Colon		Mass weighted mean of dose to Upper Large Intestine (ULI) and Lower Large Intestine (LLI) [87,88]	ULI: 7601 7801 8001 LLI: 8201 8401
Lung		Total imparted energy in the alveolar interstitium of the lungs divided by its total mass	9700 9900
Remainder tissues		Arithmetic mean of the equivalent doses to the 12 + 1 (prostate) remainder tissues [87]; Equivalent dose to a remainder tissue with multiple sites (adrenals, extrathoracic tissue, kidneys, lymphatic nodes, muscle and oral mucosa) is calculated as the total imparted energy on its tissue sites divided by their total mass	Adrenals: 100 200 Extrathoracic tissue radiosensitive layer: 302 402 Gallbladder: 7000 Heart: 8700 Kidneys: 8900–9400 Lymphatic nodes: 10000–10500 Muscle: 10600–10900 Oral mucosa: 500 501 600 Pancreas: 11300 Prostate: 11500 Small intestine radiosensitive layer: 7401 Spleen: 12700 Thymus: 13100

Table 5.1—continued on next page.

Table 5.1—continued from previous page.

Organ/Tissue	wT	Organ equivalent dose calculation method	Phantom organ/tissue site ID used for the equivalent dose calculation
Stomach		Dose to radiosensitive layer	7201
Gonads	0.08	Total imparted energy to the testes divided by their total mass	12900 13000
Bladder	0.04	Dose to radiosensitive layer	13701
Oesophagus			11001
Liver		Dose to liver	9500
Thyroid		Dose to thyroid	13200
Bone surface (endosteum)	0.01	KERMA to spongiosa sites[77]	1400 1700 2000 2300 2500 2700 2900 3200 3500 3800 4000 4200 4400 4600 4800 5000 5200 5400 5600
Brain		Dose to brain	6100
Salivary glands		Total imparted energy to the salivary glands divided by their total mass	12000 12100
Skin		Total imparted energy to radiosensitive skin layer sites divided by the total mass of radiosensitive skin layer sites	12201 12301 12401 12501

To maintain a balance between simulation accuracy and efficiency, the Penelope physics list that originates from the PENELOPE code[66] was used in Geant4 with a range cut of 1 mm. However, radiosensitive layers found in the phantom's tissues such as the skin, the stomach and the urinary bladder are only tens of μm thick. Also, the phantom does not explicitly contain the radiosensitive layers of endosteum and red bone marrow. Moreover, the range in tissues of electrons with energies below 120 keV are not

more than a few hundred μm so a range cut of 1 mm practically enforces the Kinetic Energy Released per Unit Mass (KERMA) approximation.

However, for energies below 80 keV and 200 keV, the dose to endosteum and red bone marrow respectively is conservatively approximated by the KERMA in spongiosa with an overestimation that reaches several tens of percent.[77] Between 80-200 keV the dose in endosteum is underestimated by KERMA in spongiosa by up to a maximum of ~5%. Because this is a small underestimation compared to the several tens of percent of overestimation at lower energies, and because as shown later the energy spectra of the sources peak at energies much lower than 80 keV, the KERMA to spongiosa was considered a conservative dose approximation in both endosteum and red bone marrow.

Also, electron equilibrium exists in tissues deep inside the body[77] so the 1 mm range cut is still expected to give a good estimate of the dose to the μm thick radiosensitive walls of the alimentary track, the respiratory track and the bladder.

Finally, the KERMA approximation is a conservative estimate of dose to superficial tissues such as the skin, breast and testes at energies below 1 MeV.[77]

5.3 Results

The energy spectra from the different source designs are shown in Figure 5.4. Target thickness does not greatly affect the spectrum width although in Figure 5.4b, where the area under the curve of each spectrum is plotted, it is clear that target thickness affects the photon yield. The photon yield from 90 kVp reaches a plateau within this range of target thickness but the photon yield from 120 kVp is monotonically increasing. At 3 μm, 120 kVp is ~1.7 times as efficient in generating photons while this factor is close to 2 for 6 μm. That means that with input power being the product of voltage and current, a 90 kVp source would need between 28% and 50% more input power to produce the same amount of flux as a 120 kV one.

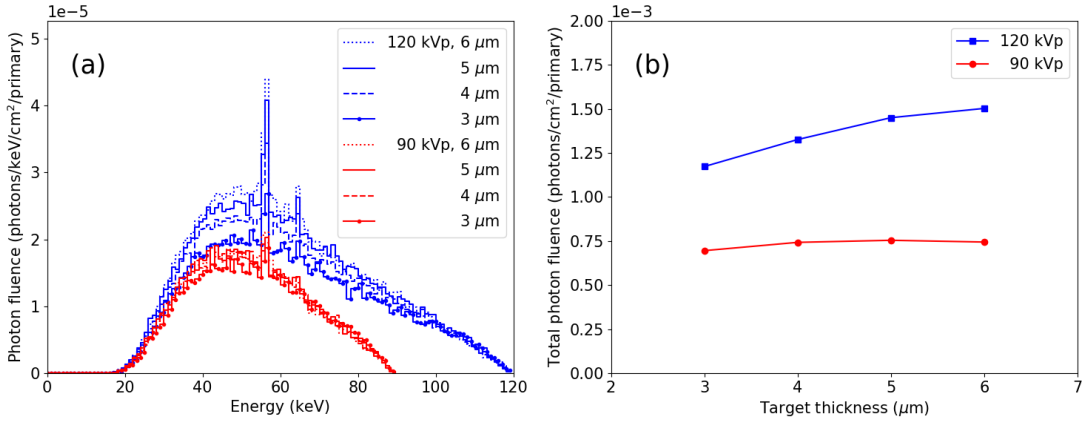

FIGURE 5.4: Photon energy spectra from different source geometries. The spectra comprise a Bremsstrahlung component and characteristic emission lines of Ta: K_α lines close to 56 keV and K_β lines close to 65 keV.

FLUKA results of the attenuation of the 90 kVp and 120 kVp spectra in Al are shown in Figure 5.5. Higher voltages increased the Half-Value Layer (HVL) but the target thickness had negligible effect. The 71 kVp and 100 kVp plots are shown for completion. According to the United States Food & Drug Administration (FDA) [89] and the European Commission, [90] the minimum HVL for 90 kVp and 120 kVp diagnostic X-ray sources should not be less than 3.2 mm and 4.3 mm respectively. The HVL values for all target thicknesses in Figure 5.5 are approximately 6.2 mm and 7.8 mm for the 90 kVp and 120 kVp respectively so requirements were met. Also, the HVL of the 120 kVp was comparable to the 7 mm HVL of a competing commercial system when it operates at 120 kVp. [91]

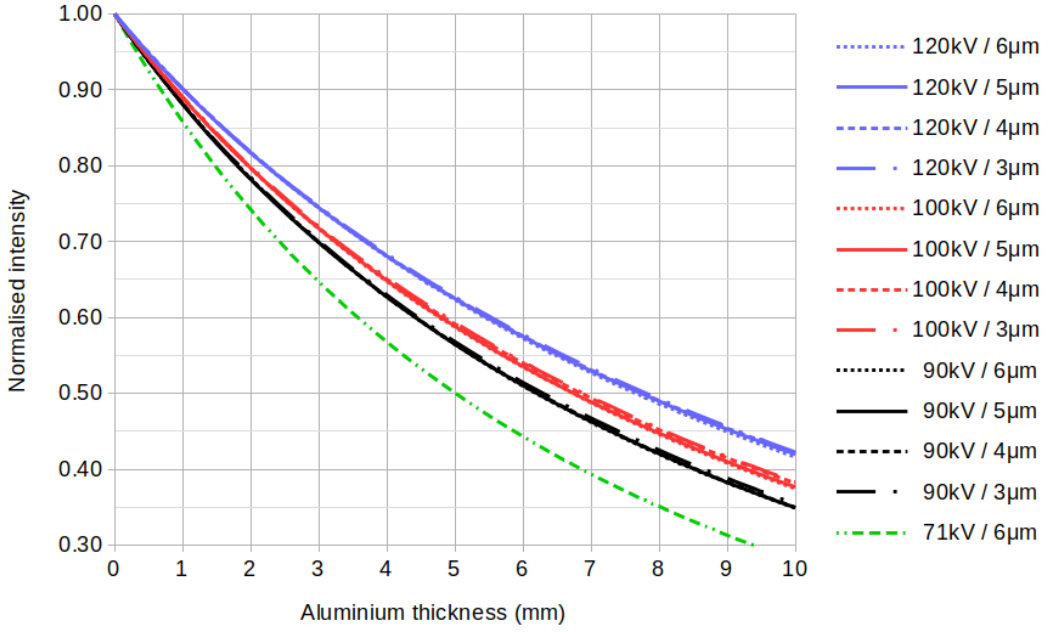

FIGURE 5.5: Attenuation in Al of the energy spectra from different source designs.

To account for the easier manufacturing and better robustness of thicker targets as well as considering the maximum and high plateau photon yield of 120 kVp and 90 kVp respectively, the spectra from the 6 μm target were used for the X-ray beams. DT slices at different depths in the phantom using the two different source arrays are shown in Figure 5.6. Depth is resolved with this irradiation geometry and with both energies as different organs come in and out of focus on the different 3D slices. The organs in focus are the clavicle, the trachea and the spine in each column respectively starting from the left.

At each depth, images look the same regardless of energy spectrum and after calculating the pixel-wise numerical differences, these were found below 10%. The maps of relative difference are noisy with no specific structure which means that DT slices are almost identical with either voltage. Values larger than 10% lie on the outer regions of the images perhaps because the size of the X-ray fields matches the size of the detector. Convolving Figure 5.6(a-f) with 2D kernels of various sizes emulated a gradually higher

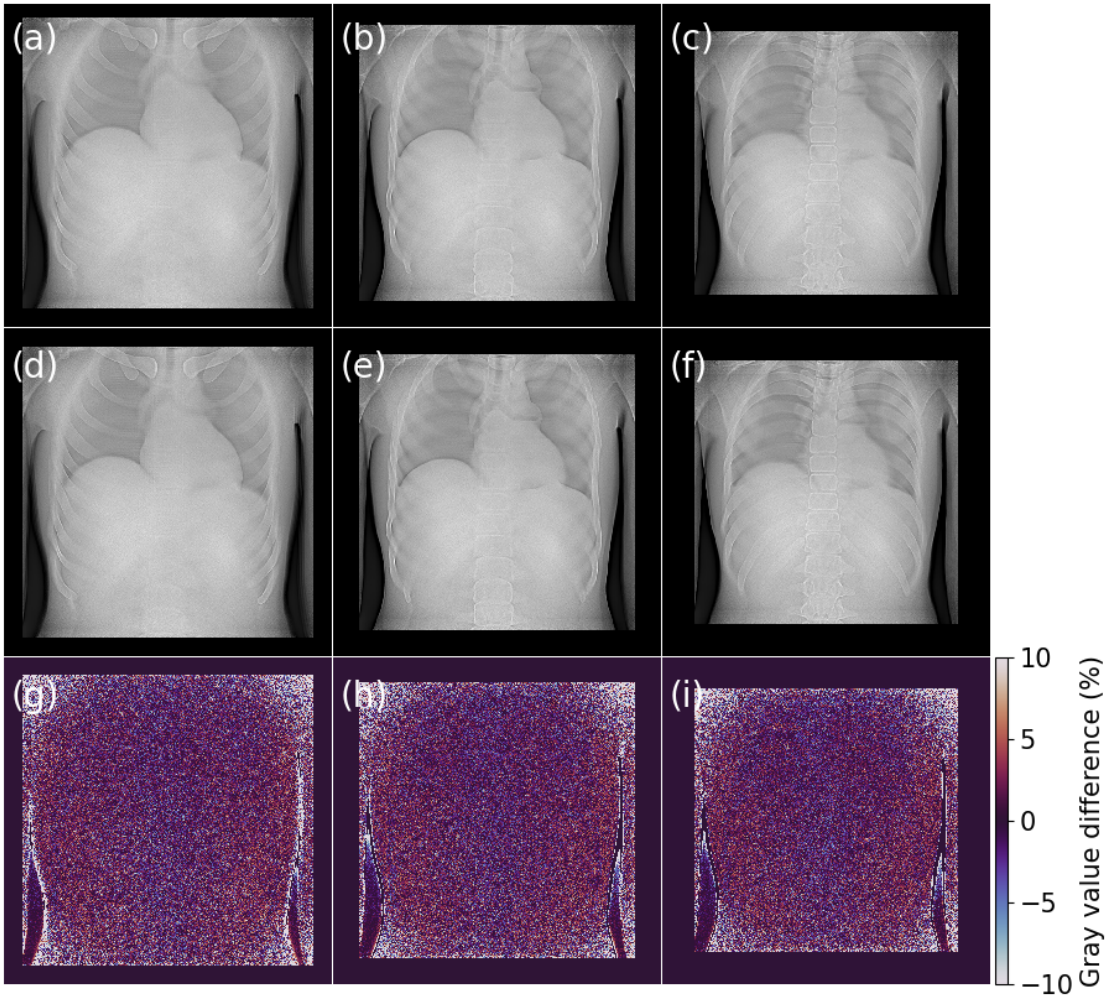

FIGURE 5.6: a-c) Tomosynthesis slices at different depths using the 120 kVp source array, d–f) same slices with the 90 kVp source array, g–i) relative percentage difference between 120 kVp and 90 kVp.

photon flux which further reduced these differences as shown in Figure 5.7. These results agree with literature[42] on the equivalence of image quality with 90 kVp and 120 kVp.

Moreover, a zone of zero values at the edges was produced by the reconstruction algorithm and it became larger for slices that lie closer to the source array. As shown in Figure 5.2, the phantom was irradiated posteroanteriorly so the zero pixel zone was larger for slices closer to the spine and smaller for slices closer to the sternum.

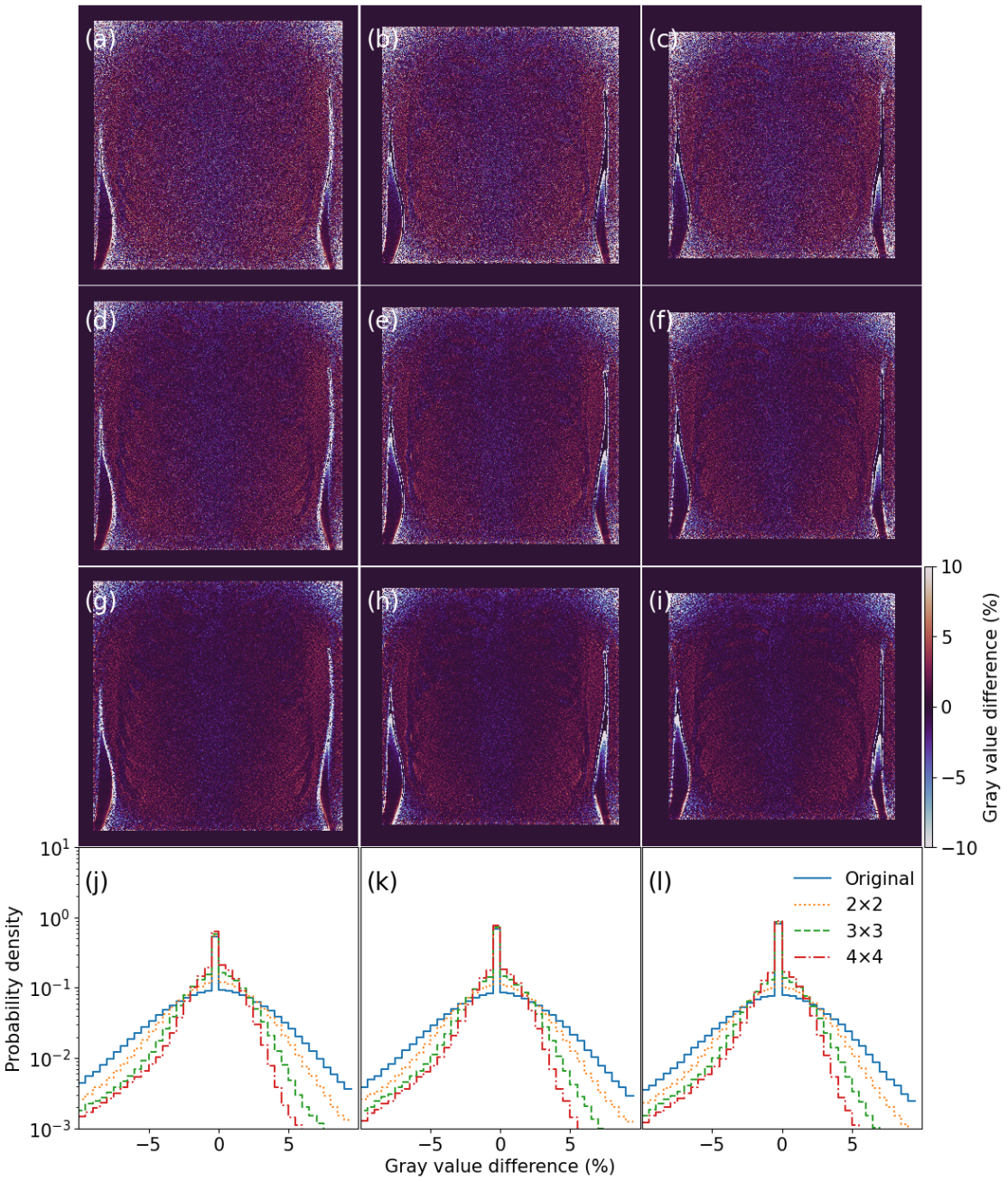

FIGURE 5.7: Relative percent difference of the slices in Figure 5.6(a-f) after binning them with kernels of various sizes to emulate a higher photon flux. Kernels were: a–c) 2×2, d–f) 3×3, g–i) 4×4. Images become darker with larger kernels. Histograms of the values in a–i are drawn in j–l together with histograms at the original slice resolution from Figure 5.6(g-i). Histograms become narrower with larger kernels. Each column in this figure corresponds to the respective column in Figure 5.6.

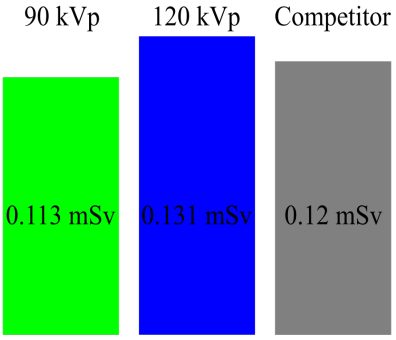

FIGURE 5.8: Effective dose of the 120 kVp and 90 kVp source arrays and of a commercial DT system.

Finally, the effective dose was 11.575 μSv with 90 kVp and 13.425 μSv with 120 kVp with a statistical error of less than 1%. Therefore, there is clinical benefit in reducing the accelerating voltage. However, this effective dose was calculated for the arbitrary photon flux that was enough for 500 μm pixels. Scaling this dose to a 160 μm pixel size so that the same number of photons arrives at the smaller pixels, the effective dose becomes 0.113 mSv and 0.131 mSv for 90 kVp and 120 kVp respectively as shown in Figure 5.8. These values are close to the 0.12 mSv of a clinically available chest DT system with 200 μm pixels.[86]

5.4 Discussion

For the choice of transmissive X-ray target thickness, preliminary simulations were performed to find candidate values. In the tested range between 1–20 μm for 90 kVp and 120 kVp, a range of 3-6 μm produced a relatively large amount of photons with both voltages. Thicker targets suffered from self-absorption, especially for 90 kVp. This was also obvious in Figure 5.2(b) where the photon yield with 90 kVp started declining after 5 μm.

The X-ray beams used were as wide as the detector and there were at least 50 cm between source and patient. Therefore, a uniform X-ray field was expected to arrive at the patient. Also, with energies below 120 keV, photons that enter the collimators are almost always absorbed so they do not contribute a lot to the X-ray field that reaches the patient. So any photon density and spectrum perturbations caused by the added collimators would be insignificant for the scope of this study so collimators were omitted to improve the efficiency of the simulations. Also, photons that are produced from electrons backscattered towards the electron emitter cathode are mostly absorbed in the source assembly therefore the cathode was also omitted.

The detector model was a simple 2D plane that counted the number of photons that crossed its surface, normalised by the angle of incidence of each photon. This approximation is not rare in literature and it was used here because of its simplicity. Nevertheless, in an experimental equivalent of this work the conclusions agreed with

the results of this thesis.[42] So, the simplicity of the detector model should not have had added a significant bias to the results. Also, using 500 μm pixels instead of 160 μm was done to get improved pixel statistics within a reasonable time. This meant that fewer photons were transported and as such the dose to the patient was systematically less. This was addressed by multiplying the dose with the ratio of the surfaces of the two pixel sizes which produced the dose expected with 160 μm pixels if the number of incident photons per pixel was kept the same as with the 500 μm pixels.

The irradiation geometry used in this proof of concept caused a lot of stray radiation outside the limits of the detector that would only increase the dose to the patient without providing clinical information. To get 3D images it is necessary that beams overlap at least partially and depth resolution is improved with a larger angular range of projections. Therefore, the Adaptix system would in reality be comprised of multiple, stationary, flat panel source arrays, at an angle relative to each other, similar to what is shown in Figure 5.2(c) and what has been shown by Wells et al for breast tomosynthesis.[32] The panels could be furnished with collimators that tailor each beam to the detector and reduce stray radiation. The wider angular range of projections and the tailored X-ray fields will offer high depth resolution without dose from stray radiation and the small form factor of the flat panel source arrays will maintain the compact size of the system.

The calculation of the effective dose was a conservative approximation based on the KERMA in the various tissues. As an example, bone marrow is a tissue with the largest weighting factor of 0.12, and the KERMA in spongiosa overestimates the dose in bone marrow by ~120%–130% at 45–50 keV,[77] approximately where the spectra use here peak(Figure 5.2(a)). Similar conclusions can be drawn for the rest of the organs.[77,85,87] Therefore, the true value of the effective dose is expected to be appreciably lower than 0.113 mSv and 0.131 mSv for 90 kVp and 120 kVp respectively. For a more accurate calculation, a range cut of 1 μm should have been used but this would have come at a great cost to simulation time. Therefore, the conservative KERMA approximation with the 1 mm range cut was preferred. On the other hand, an improved irradiation geometry such as that shown in Figure 5.2(c) could have avoided irradiating the sensitive tissues in the head and neck area, which is something that happened in this study as shown in Figure 5.2(a). Therefore, with a more careful irradiation geometry, the dose per projection could have been even less allowing more projections to be added before the effective dose reached 0.12 mSv. Moreover, DT reconstruction methods can include filters to smoothen low signal to noise projections before reconstruction,[61] allowing each projection to be taken with a lower photon flux thus imparting less dose to the patient.

Also, the choice of photon flux was arbitrary, using the same number of photons as the orthopaedic system in Chapter 4. This happened to offer low statistical errors in the images and in the organ dose calculations and also happened to result in effective dose comparable to commercial systems. However, a quick calculation of the mAs required

to produce this amount of flux returned numbers that were orders of magnitude larger than the specifications. For example, with 100 μA per emitter and assuming the X-ray target has the photon yield from Figure 5.4 and a 1 mm cross section per collimator aperture, each emitter should be active for about 4.2 s and 2.1 s with 90 kVp and 120 kVp respectively to produce 2.5 billion photons whereas specifications are closer to 100 ms. Nevertheless, the total scan time from all emitters is not supposed to exceed 10 s. So, the number of photons should have been tens of times lower. However, this study compared images in a pixel-wise fashion, so this very large amount of photon flux was necessary to avoid the generation of image differences caused by statistical errors. Differences were caused by physical models and thus the conclusions of this study will not change by using a different amount of photon flux.

With only 1% of the photons, the statistical noise in the images would increase by about 10% and the dose would decrease 100 times. Using 1/42 of the photons with the 120 kVp FPS, would decrease the dose 42 times and increase the already low (3%) statistical noise in the 2D images by approximately $\sqrt{42}$=6.5 times. On the other hand, using 9 times as many emitters with a multi-FPS system such as the one in Figure 5.2(c), would increase the dose to 9/42 of the effective dose calculated in this example. The end result is a multi-FPS system with just 6.5 times as much noise as this study but only 21% of the dose. For the 90 kVp FPS these values are approximately 4.6 as much noise and 43% effective dose.

All the above suggest that a system like the one in Figure 5.2(c), with many more projections than the 25 used in this work and with careful irradiation of the patient could be used for DT without exceeding the dose of commercial DT systems and without excess image noise, offering all the benefits of using stationary source arrays.

5.5 Conclusion

A stationary flat panel source array paired with a stationary imaging detector offers 3D information of a human chest without the need of rotating components. There is clinical benefit in reducing the accelerating voltage from 120 kVp to 90 kVp as this reduces the effective dose while maintaining image quality. Photon yield and energy spectrum of photons exiting the system are insensitive to a transmissive target thickness between 3 μm and 6 μm for 90 kVp, which could reduce the challenges of manufacturing. The increase in input power demands due to the lower efficiency of a 90 kVp source could reach 50% but this excess could be offset by the lower power requirements from being able to operate with a reduced source to image distance. Also, the faster scan times due to electronic activation require power to be on for shorter periods. Finally, the effective dose with this imaging geometry was calculated in a rather conservative manner and was close to that of clinically used systems. Therefore, a system with multiple flat panel sources, at an angle, creating an X-ray field tailored to the patient could be developed

to deliver faster DT scans, with superior image quality compared to linear arrays and without the risk of excess dose.

Chapter 6

Ipioni: an automated designer of stationary digital tomosynthesis systems with multiple rectangular distributed source arrays

Moving from single-FPS to multi-FPS 3D X-ray imaging systems must offer improved diagnostic performance without compromising system compactness and portability. However, the number of FPSs and the wide range of FPS specifications like emitter pitch, X-ray cone angle and panel rotation turn this upgrade into a multidimensional optimisation problem. Therefore, computational techniques had to be developed to efficiently and automatically explore the vast range of prospective multi-FPS design solutions and identify those that offer optimum system performance. This chapter includes a high-level overview of Ipioni, a software application that was developed in Python and is currently used to find multi-FPS design solutions for the Adaptix chest DT system. Ipioni generates multi-FPS system design solutions that satisfy geometrical specifications such as minimisation of stray radiation and fitting of multiple FPSs in space without overlaps. For each design, Ipioni calculates a range of irradiation geometry metrics like beam overlap in the patient and on the detector and finally generates files that are used in Monte Carlo simulations and with image reconstruction software so that each design can be thoroughly studied in terms of FPS performance, patient dose and image quality. Ultimately, that information will be also used during manufacturing. The capabilities of Ipioni are described in this chapter[1]and two use cases are demonstrated where optimum designs are found for multi-FPS DT systems using actual specifications from Adaptix. The impact of Ipioni in the acceleration and cost reduction of R&D is described in detail and suggestions for integration of Ipioni into other applications are given to highlight Ipioni's value as an early stage and mature stage design and optimisation tool.

[1]Parts of this chapter have been presented at the 13th International Particle Accelerator Conference. [92]

6.1 Introduction

Developing a chest DT system requires a technological upgrade of the current Adaptix FPS to higher voltage and higher current but also the use of multiple FPSs in order to cover the larger area of the human chest. In Chapter 5, higher voltage and higher current FPSs were simulated with Monte Carlo methods and were found capable of producing DT images of a human chest. The effective dose with a single 25 emitter FPS was found low enough to allow more FPSs so that a larger range of angular projections could be collected during imaging. However, patient dose is only one of the many variables that affect the design of a multi-FPS DT system. There are numerous specifications such as the X-ray beam full cone angle, the emitter pitch, the SID, the number of panels and emitters and the size of the FPS, the patient and the detector which by their sheer number and complex relationships largely complicate the process of finding those values that optimise multi-FPS DT performance.[47,93] Therefore, a computational way had to be devised that takes into consideration as many system parameters and acceptance criteria as possible and confirms whether or not a system with a given specification can be built and what are some of its irradiation geometry characteristics that could affect image quality.

Ipioni, pronounced ee-pee-o-nee, from the Greek pronunciation of the goddess Epione, the wife of the ancient Greek god of medicine Asclepius, is a set of algorithms written in Python and packaged under a single Python application that allows the automatic design of DT systems with multiple stationary FPS arrays and a stationary flat panel detector. The capabilities also include the parameter scan for acceptable designs within a region of specifications and the calculation of several irradiation geometry metrics. The capabilities of Ipioni and some of the results produced so far are demonstrated in this chapter. These results have already helped Adaptix narrow down R&D decision trees and prioritise some specifications over others, adding a critical contribution during this early stage of development of a new product. Ipioni has also been used to develop the preliminary design of the multi-FPS chest DT system in Figure 5.2(c).[43]

6.2 Machine design parameters taken into account

An artistic illustration and a 3D model designed by Ipioni of the future multi-FPS chest DT system by Adaptix are shown in Figure 6.1. These are not the final versions of the system that will be manufactured, but used here to help visualise the design steps described below. In Figure 6.1(b), the patient is represented by a semi-transparent box that lies on top of the blue-coloured flat panel detector. The X-ray cone beams are coloured purple and are emitted from the source arrays that lie in each semi-transparent, white-coloured FPS. The emitter arrays are positioned mid-high inside the FPSs and each FPS is angled appropriately so that radiation is focused towards the centre of the detector. A necessary air gap between all FPSs and the patient offers more comfortable positioning and the FPSs do not overlap with each other. Finally, for simplicity, the

X-ray beams are considered perfectly sharp without a penumbra and the fields they produce at the detector surface are strictly confined within the detector edges.

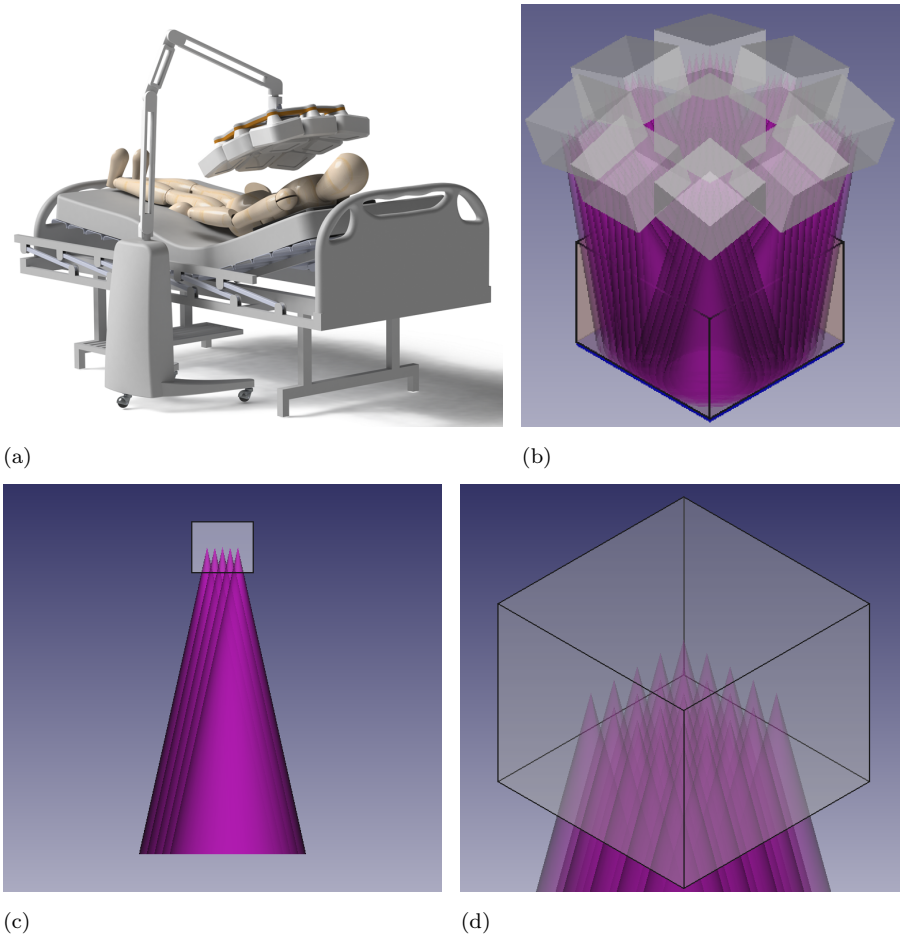

FIGURE 6.1: Illustrations of the Adaptix chest DT system. a) artistic, b) based on Ipioni, c-d) details of a single flat panel source designed by Ipioni. The emitter array lies mid-high in the panel and is parallel to it and all emitters create X-ray cone beams with beam axes normal to the emitter array. Cone beams are identical and the emitter pitch is constant across the array. A multi-FPS system has identical FPSs. (b-d) drawn in FreeCAD.[84] (a) reproduced with permission from Adaptix Ltd.

The parameters necessary to describe and build such a system are shown in Table 6.1. These parameters dictate only the geometric characteristics of the system but as it will be shown later, they are enough to significantly narrow down design and optimisation decision trees before engineering, physics and clinical issues are addressed. The values of these parameters can be changed by the user otherwise they take their default values. These parameters are input to Ipioni and the code can check whether a design is feasible in terms of a number of acceptance criteria such as physical overlaps among components, minimum clearance between patient and device and size of X-ray fields as described in Section 6.3. If the design passes all the criteria it is considered feasible and Ipioni can then calculate a range of irradiation geometry characteristics or export information that is useful for image reconstruction, computer-aided design or physics simulations software. A description of the functionalities available within Ipioni are given in Section 6.4.

TABLE 6.1: Multi-flat-panel-source parameters taken into account by Ipioni.

Parameter	Default value(s)	Description
Panel population	9	The number of flat panel sources used. Values can be between 1 and 9.
Full cone angle	25°	The full cone angle of the X-ray cone beams of all flat panel sources.
SID	60 cm	The source-to-image distance of all flat panel sources, measured between the detector surface and the centre of the source array of each panel.
Emitter pitch	1.5 cm	The pitch of emitters on the emitter array of all flat panel sources.
Panel angle	12.5°	The angle with which all panels apart from the central one are rotated.
Panel size	$12\times12\times10\,\mathrm{cm}^3$	The length, width and height of all the flat panel sources.
Detector length	43 cm	The length of the flat panel imaging detector. Length is measured along the craniocaudal direction in the patient frame of reference.
Detector width	43 cm	The width of the flat panel imaging detector. Width is measured along the lateral direction in the patient frame of reference.
Stray allowance	0 cm	Thickness of a strip around the edges of the detector where radiation is allowed to exist.
Patient thickness	28 cm	The thickness of the patient, measured along the posteroanterior or anteroposterior direction, with zero at the detector surface. Patient length and width are the detector equivalents. The number of voxels along the patient thickness is always such that voxel thickness is 1 cm. As such, integer values of patient thickness are required.

Table 6.1—continued on next page.

Table 6.1—continued from previous page.

Parameter	Default value(s)	Description
Detector length resolution	43	Number of pixels along the detector length. This is also the number of voxels along the patient length.
Detector width resolution	43	Number of pixels along the detector width. This is also the number of voxels along the patient width.
Emitter rows	5	The number of rows of the emitter array in all flat panel sources.
Emitter columns	5	The number of columns of the emitter array in all flat panel sources.
Form factor	$1\times1\times1.5\,\mathrm{m}^3$	Maximum allowed end-to-end length×width×height of the DT imaging system including the FPSs and the detector.
Patient clearance	5 cm	Minimum allowed distance between any FPS and the patient.

6.3 The basics of the Ipioni design engine

In all the functionalities available in Ipioni and described in Section 6.4, the code tries to build a multi-FPS system using the parameters from Table 6.1. This includes building and positioning the detector and the patient, building and positioning the FPSs accordingly, projecting the X-ray cone beams from the FPSs on the detector and then checking that all acceptance criteria in Table 6.2 are met. Meeting all criteria is necessary for the design to be considered feasible.

An important aspect about the construction of the DT systems by Ipioni is that a maximum of 9 panels may be added and each panel has a unique relative position where it is placed and a unique rotation axis around which it is rotated to focus the radiation at the detector centre. The 9 panels, their names and their unique relative positions and rotation axes are listed in Table 6.3.

To position each FPS in the chest DT device, Ipioni first builds the FPS and its emitter array and positions it parallel to the detector with its centre overlapping with the detector centre. The FPS is then rotated around its rotation axis by the panel angle, followed by a vertical shift to the specified SID. This shift is measured between the detector surface and the centre of the emitter array. Then, the elliptical X-ray fields from all emitters are drawn on the detector surface to check that the X-ray field size

TABLE 6.2: The acceptance criteria for any DT system designed by Ipioni.

Criterion	Threshold	Description
X-ray field size	Detector size + 2×stray allowance for both detector dimensions	Cumulative X-ray field of any FPS must not exceed the user defined limits of detector size + stray allowance.
Inter-FPS overlaps	0 cm	Panels must not physically overlap with each other.
FPS-patient overlaps	5 cm	The air gap between any FPS and the patient must not fall below a minimum threshold.
Total system size	$1\times1\times1.5\,\mathrm{m}^3$	End-to-end dimensions of the integrated system (FPSs & detector) must not exceed a maximum size.

TABLE 6.3: Names, relative positions and rotation axes of the 9 flat panel sources. Coordinates are relative to the 2D frame of reference of the detector with origin at the detector centre, x along the left-to-right patient direction and y along the foot-to-head patient direction. x_i, y_i are non-negative and rotations follow the right-hand rule.

Panel name	Position relative to detector centre	Rotation axis
Top left	$(-x_{tl},+y_{tl})$	$\frac{(-1,-1)}{\sqrt{(-1)^2+(-1)^2}}$
Top	$(0,+y_t)$	(-1,0)
Top right	$(+x_{tr},+y_{tr})$	$\frac{(-1,1)}{\sqrt{(-1)^2+1^2}}$
Left	$(-x_l,0)$	(0,-1)
Central	Aligned to detector centre	None
Right	$(+x_r,0)$	(0,1)
Bottom left	$(-x_{bl},-y_{bl})$	$\frac{(1,-1)}{\sqrt{1^2+(-1)^2}}$
Bottom	$(0,-y_b)$	(1,0)
Bottom right	$(+x_{br},-y_{br})$	$\frac{(1,1)}{\sqrt{1^2+1^2}}$

criterion from Table 6.2 is met. At this stage, the cumulative X-ray field of the FPS may fall outside the detector + stray radiation limits but if the criterion is passed it means that the FPS can be translated parallel to the detector so that the X-ray field eventually fits within the detector + stray radiation limits. To do that, the circumscribed rectangle of the cumulative X-ray field of the FPS on the detector surface is assigned as the bounding rectangle of that field. Following the rules from Table 6.3, the distance (x_i,y_i) of the appropriate edge or edges of that rectangle and the corresponding edge or edges respectively of the detector + stray radiation limits are calculated. The FPS is then translated according to Table 6.3. With this, the FPS has taken its final position

and the next FPS can be built in the same manner. After all FPSs have taken their positions, the rest of the acceptance criteria from Table 6.2 are checked. If any of them fail, the design is discarded as unacceptable. If a DT system design passes all checks, then it is marked as acceptable and it is used by Ipioni for various calculations or illustrations as explained in Section 6.4.

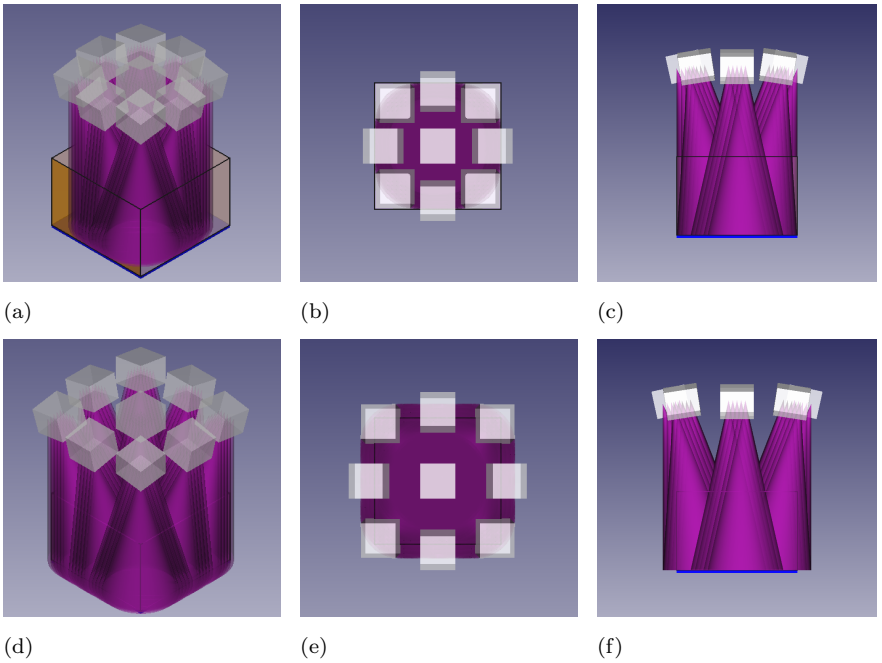

FIGURE 6.2: Chest DT systems designed by Ipioni with the default parameters from Table 6.1 and with (a-c) 0 cm and (d-f) 5 cm stray allowance.

The unique lateral translation and relative position of each FPS can be observed in Figure 6.2 where the same 9-FPS DT system is built twice, with 0 cm and 5 cm stray radiation allowance. With no stray radiation allowance the X-ray fields of all FPSs are tangent to the detector edges but with the extra 5 cm around the detector the panels are shifted by 5 cm away from the detector centre following the directions listed in Table 6.3.

6.4 Functionalities of the Ipioni code

In the following, the terms irradiation geometry and DT system design are used interchangeably and they both refer to a DT system design that can be described by a unique set of values for all parameters in Table 6.1.

6.4.1 Parameter scan for acceptable irradiation geometries

Parameter scans of full cone angle, SID, emitter pitch and panel angle can be performed while keeping the rest of the parameters in Table 6.1 constant and checking each DT system design against the acceptance criteria from Table 6.2. Designs that pass all of them, are saved in a file. The range and resolution of the scan are user defined.

6.4.2 Plotting of the X-ray beams on the detector or inside the patient

For those designs that are acceptable, Ipioni can produce illustrations of the spatial distribution of the X-ray beams on the detector surface and in 2 axial slices within the patient as shown in Figure 6.3.

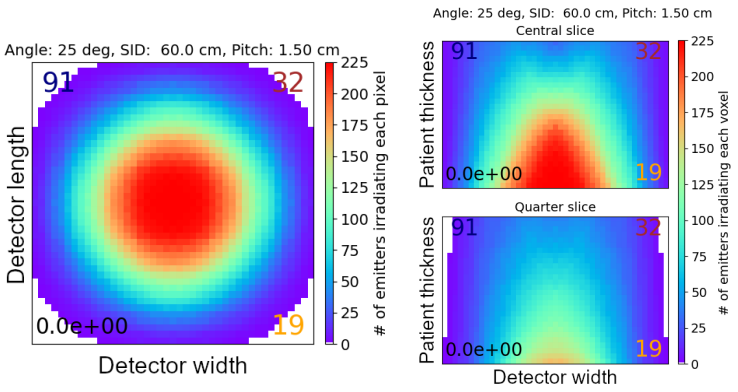

(a) (b)

FIGURE 6.3: Maps of the X-ray field distribution a) on the detector and b) in 2 axial slices in the patient. The central slice goes through the centre of the patient box and the quarter slice is 1/4 from the bottom edge of the patient box. The numbers in the corners of each plot are irradiation metrics described in Section 6.4.4: top left: detector illumination, top right: 2D overlap, bottom left: stray radiation surface, bottom right: 3D overlap. All plots are for a system with the default parameters from Table 6.1.

6.4.3 Exporting emitter coordinates and other device specifications

At this early stage of development, Adaptix is using a movable high-power X-ray source to emulate the positions of the emitters on the not-yet-available high-power FPS arrays. As such, knowledge of the position of those emitters is essential to accurately emulate them with the movable source. These positions are also necessary for simulating the multi-FPS DT system with Monte Carlo or other methods in order to study its performance computationally. Ultimately, these positions and specifications will be used to build the FPSs and integrate them into the multi-FPS DT system. Finally, 3D illustrations of the prospective designs are necessary during design and optimisation.

Ipioni allows the user to export the required data in the appropriate format to facilitate these applications. Figure 5.2 and all of the device illustrations shown in this chapter apart from Figure 6.1(a) were produced by first exporting the emitter coordinates and other device specifications from Ipioni and loading them in FreeCAD to draw the 3D models.

6.4.4 Calculation of irradiation geometry metrics

Due to the thousands of candidate designs that must be compared before the best one is found, numerical metrics, some of which are listed in Table 6.4, have been defined to describe the performance of the multi-FPS DT systems. These metrics offer a convenient

way of doing this comparison by studying the distribution of the DT system designs in the irradiation metrics space instead of having to compare thousands of images such as Figure 6.3. This is demonstrated in full extent for two case studies in Section 6.5.

Ipioni can calculate the metrics of any number of irradiation geometries and save them in a file. The code can either take a list of acceptable geometries produced by the parameter scan mentioned above and calculate their irradiation metrics or be given geometries of unknown acceptance status. Before calculating the irradiation metrics, Ipioni builds the candidate DT system anyway so it always checks the acceptance criteria from Table 6.2. If a geometry does not pass all of them, metrics default to -1.

TABLE 6.4: List of irradiation metrics calculated by Ipioni.

Metric	Units	Description
Angular range	degrees	The widest angle between any 2 emitters and the centre of the detector.
Detector illumination	%	Area of the detector irradiated by at least 1 X-ray beam. Ideally, all pixels are irradiated by at least 1 beam resulting in 100% illumination.
2D overlap	%	Pixel-wise sum of number of emitters irradiating each detector pixel divided by total emitters×total pixels. Ideally, all emitters would irradiate all pixels resulting in 100% 2D overlap.
3D overlap	%	Voxel-wise sum of number of emitters irradiating each patient voxel divided by total emitters×total voxels. Ideally, all emitters would irradiate all voxels resulting in 100% 3D overlap.
Stray radiation	cm^2	The sum of the portions of the X-ray fields that fall outside the detector edges. Portions are summed regardless of any overlaps among them.
Irradiation non-uniformity	cm^2	Standard deviation of the surfaces of the Voronoi cells,[94,95] generated by the emitters when the latter are projected onto the unit hemisphere. Ideally, emitters would be uniformly distributed resulting in $0\,cm^2$ non-uniformity.

The angular range is a commonly used metric in DT and detector illumination is ideally maximised in order to collect as much information as possible. Regarding 3D overlap, higher levels of beam overlap are generally expected to produce better DT images as explained in Chapter 2. A way to quantify beam overlap is to count how many X-ray beams irradiate each patient voxel simultaneously, sum this count for all voxels and divide by the sum of the ideal case where all voxels are irradiated by all beams. In the ideal case, all beams overlap in all voxels so this is expected to offer high levels of 3D diagnostic information. Therefore, due the definition of the 3D overlap metric in Table 6.4, maximising it is deemed a reasonable step in the search of a good irradiation geometry. The 2D overlap metric in Table 6.4 was defined under the same principle but for the 2D detector pixels.

It should be noted that on rare occasions maximising the angular range can lead to no beam overlap. For example, the geometry could be such that the beams are so widely distributed and perhaps each beam is so narrow that they end up not overlapping

with each other. Also, maximum beam overlap can be achieved by having no angular distribution of sources. For example, if all X-ray sources have identical position and direction and each one is wide enough to irradiate all the patient voxels, then by definition this offers 100% beam overlap with zero angular range. But these are two theoretical extremes that are not expected to be encountered in practice.

The stray radiation metric in Table 6.4 is named after the stray radiation specification in Table 6.1 and was defined to measure the surface area of the radiation that falls outside the detector. Stray radiation reduces source efficiency and increases patient dose without any clinical benefit thus it should be minimised with appropriate collimation techniques and source positioning.

Finally, the irradiation non-uniformity was defined in order to combine in one value, 2 metrics that are commonly used in the literature to describe DT acquisitions, that of the angular range and of the density of projections.

This group of irradiation metrics is a preliminary suggestion for a way to describe the performance of the multi-FPS chest DT systems using a few numerical values. A method to test the appropriateness of these metrics is described in Section 6.7 as a proposed future work. However, even if in the future these are proven not appropriate, Ipioni nevertheless offers the framework to design multi-FPS DT systems and it is just a matter of properly using the data it produces to generate representative measures of system performance. Also, calculations of irradiation geometry metrics happen after a system has been built (which happens only if the system passes the acceptance criteria in Table 6.2) and just before any results are exported. Therefore, any modifications on the calculation of the irradiation geometry metrics will leave the core Ipioni design engine untouched. A change in the acceptance criteria can also be done without changing the design engine since these are tested after each design has been built.

Therefore, regardless of the appropriateness of the system irradiation geometry metrics defined in Ipioni and listed on Table 6.4, Ipioni is considered to be a useful tool for the early stage design of multi-FPS DT systems. The metrics used here serve the purpose of demonstrating the capabilities of the code and are used as a set of proposed figures of merit that may be appropriate for describing system performance with just a few numbers. Any amendments to the irradiation geometry metrics would need minor changes to the code that would not interfere with the core Ipioni design engine. A discussion about the integration of the Ipioni code into other applications and the use of Ipioni in combination with other software like physics simulation codes and image reconstruction algorithms is given in Section 6.7.

6.4.5 Tailored X-ray fields

Emitter deactivations

Any number of emitters in any FPS can be deactivated by the user before any of the code functionalities are used. This can be done to simulate purposeful deactivations that create tailored X-ray fields suited for different patients or imaging scenarios or to

simulate how unexpected emitter failures to turn on would affect the DT system. A heart-shaped X-ray field produced by Ipioni using this method is shown in Figure 6.4 demonstrating the ability of a multi-FPS system to produce X-ray fields with both curved and straight sections, parallel to the detector dimensions and in a diagonal. This offers a respectable level of X-ray field shape flexibility without the added weight, size and cost that comes with using additional collimators.

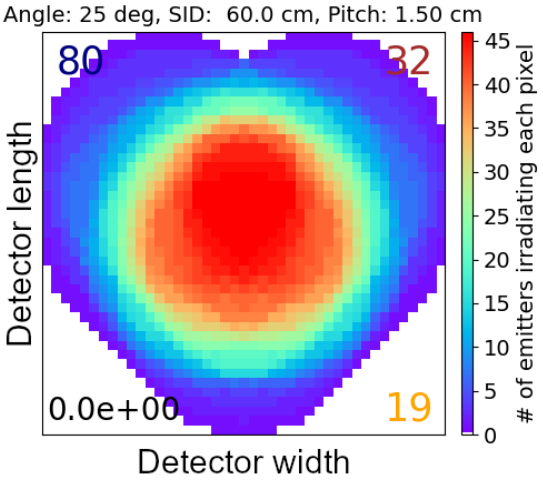

FIGURE 6.4: Example of a complex X-ray field shape produced by deactivating some of the emitters in each flat panel source of a system that is built with the default parameters from Table 6.1.

Using different flat panel source arrangements

Which of the 9 available FPSs are used in a DT system can also be changed. Examples of DT systems with different arrangement of flat panel sources are shown in Figure 6.5. Whereas more panels can irradiate the patient from more projection angles and offer better image quality, the fixed cost of producing a FPS and the form factor constrains for truly portable devices put a reasonable limit on the number of FPSs used. Moreover, the fixed pulse width per emitter means that more FPSs will lead to longer scan times and higher patient dose. On the other hand, if patient dose is kept fixed, using more FPSs must be accompanied by a lower photon flux per emitter which increases image noise. Therefore, it is important to allow control over the population and arrangement of FPSs. Ipioni follows the rules listed in Table 6.3 with any number of FPSs.

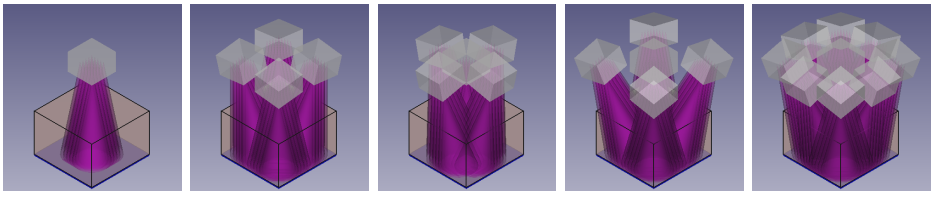

FIGURE 6.5: Examples of DT systems with different flat panel source populations.

6.5 Ipioni workflow to identify candidate designs for multi-FPS chest tomosynthesis systems

In what follows, many of the capabilities of Ipioni were combined into a design and optimisation workflow to identify candidate design specifications for multi-FPS chest DT systems with stationary FPSs and a stationary flat panel detector. This was done using true specification requirements by Adaptix.

6.5.1 Initial boundary conditions and proposed design parameters

As a result of two different technologies proposed to upgrade the current FPS to higher power, Adaptix has identified two potential sizes for those higher-power FPSs, namely $18\times18\times13\,\mathrm{cm}^3$ and $28\times28\times13\,\mathrm{cm}^3$. Also, due to the fixed cost of each FPS but also patient dose and scan time issues that come with multiple FPSs as explained in Section 6.4.5, DT systems with 9, 5(2 versions), and 4 FPSs have been proposed. They were all equipped with 5×5 emitter arrays and examples of them are shown in Figure 6.5. Starting with just this handful of boundary conditions, Ipioni was used to find the thousands of potential system designs and calculate their irradiation metrics so that an educated decision can be taken about the optimum design of a multi-FPS DT system.

To do that, a parameter scan was performed over the full cone angle, SID, emitter pitch and panel angle for the 2 different FPS sizes and the 4 FPS arrangements. After all acceptable geometries were identified, they were fed again into Ipioni to calculate their irradiation metrics listed in Table 6.4. The beam overlap and the angular range of projections are among the most important parameters that must be maximised to improve DT image quality, so the 3D overlap metric and the angular range were plotted for all the acceptable geometries. These plots were used to identify designs that had high values of both metrics. After hand-picking some of the acceptable DT system geometries that had high values for 3D overlap and angular range, Ipioni was used again to plot the X-ray fields of those systems in the patient and on the detector to visually examine how well are the patient and the detector irradiated. Ipioni was also used to export the necessary data to draw the 3D models of those DT systems in FreeCAD. The range and the step of the parameter scan are shown in Table 6.5. To simplify the parameter scan, only the minimum and maximum allowed panel angles were recorded. That is, for each unique triplet of full cone angle, SID and emitter pitch, the minimum and maximum possible panel angles were identified within the range listed in Table 6.5. The rest of the parameters from Table 6.1 had their default values.

TABLE 6.5: Range and step of the parameter scan used in Ipioni in search of the optimum design of a multi-flat-panel-source array chest tomosynthesis system.

	Full cone angle	SID	Emitter pitch	Panel angle
Range	[10°, 70°]	[33 cm, 100 cm]	[1 cm, 3 cm]	[half cone angle, 45°]
Step	5°	1 cm	0.1 cm	0.5°

6.5.2 Results with 18×18×13 cm^3 flat panel sources

4,062, 4,189, 4,726 and 4,832 acceptable geometries were identified by Ipioni for the 9-FPS, 5-FPS with the corner panels, 5-FPS with the side panels and the 4-FPS arrangement respectively and their 3D overlap and angular range are shown in Figure 6.6. 3D overlap is normalised by a number proportional to the available emitters as shown in Table 6.4 so between designs with different number of emitters but equal 3D overlap, the one with the more FPS (i.e. more emitters) shall be considered to have better beam overlap. All points in the plots are designs with unique combinations of values for the parameters listed in Table 6.1.

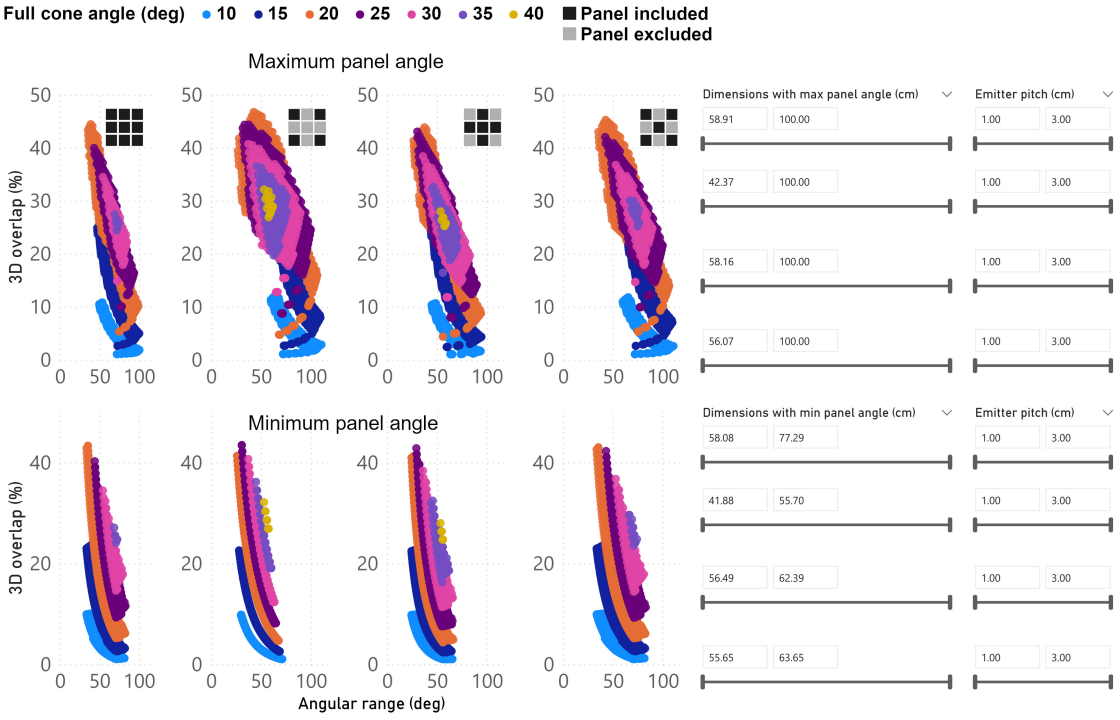

FIGURE 6.6: Ipioni-generated irradiation metrics of the acceptable geometries found with the parameter scan from Table 6.5 with 18×18×13 cm^3 flat panel sources. Every point is a geometry with unique values for the parameters in Table 6.1. Every column of value sliders corresponds to the row of plots on its left. Sliders have the same maximum length in each row for illustration purposes but correspond to different maximum numerical ranges. The numerical range of each slider is shown by the minimum and maximum values above it and is also represented by the relative position of the slider within its maximum length.

With more panels there were fewer acceptable designs. Also, there were more acceptable solutions for the 5-FPS system with the side panels than with the corner panels. Moreover, as expected, the 3D overlap and the angular range are inversely related and the optimum performance is expected to be where a balanced maximisation of both can be achieved. Wider panel angles offer a wider coverage of this irradiation metric space compared to using the minimum allowed panel angle which means that there is greater flexibility when choosing the balance between 3D overlap and angular range. This essentially translates to a greater flexibility in choosing the full cone angle, SID and emitter

pitch. Moreover, the range of end-to-end lateral dimensions of the designs, shown in the sliders on the right-hand side of Figure 6.6, are different for different arrangements of FPSs and choice of panel angle. As expected, more FPSs and at a wider panel angle occupy more space. Interestingly, FPS arrangements with just 4 FPS can be smaller than the $43\times43\,\mathrm{cm}^2$ detector as shown by the low end of the dimensions slider. Also, there are FPS designs with emitter pitch anywhere between 1 and 3 cm whereas there is no acceptable design with full cone angle greater than 40° with 4 FPSs or 5 FPSs with the side panels and no acceptable design exists with full cone angle greater than 35° with 9 FPSs or 5 FPSs with the corner panels.

There are conventional DT imaging systems with 30° angular range and in Figure 6.6 it is obvious that the vast majority of the possible FPS DT system designs offer a much wider angular range. The density of the projections within this angular range is also an important factor for DT image quality but it will be addressed later on. For the moment, considering the 30° of the angular range as a specification close to what the multi-FPS should have, finding the optimum machine design can be focused on maximising the 3D overlap around the region where the angular range is no less than 30°.

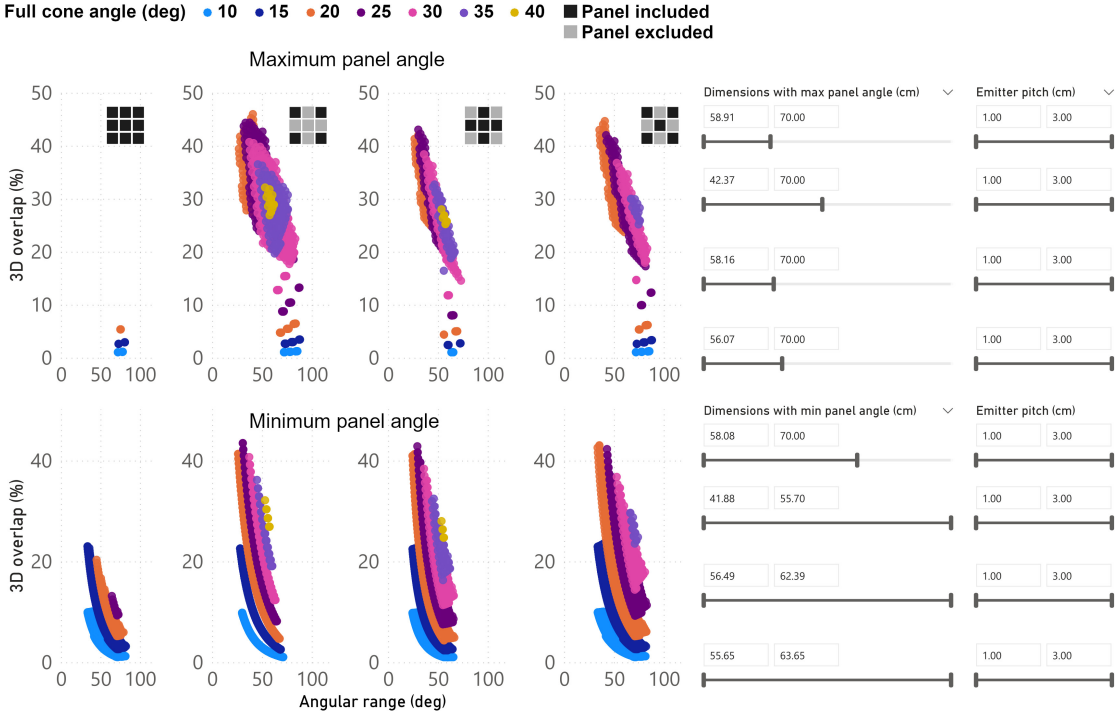

FIGURE 6.7: The irradiation metrics from Figure 6.6 but only for geometries with length × width ≤ $70\times70\,\mathrm{cm}^2$. Every column of value sliders corresponds to the row of plots on its left. Sliders have the same maximum length in each row for illustration purposes but correspond to different maximum numerical ranges. The numerical range of each slider is shown by the minimum and maximum values above it and is also represented by the relative position of the slider within its maximum length.

As mentioned in Chapter 2, smaller devices are easier to manoeuvre and offer more space in already packed ICUs and operating theatres and can pave the way for portable 3D imaging. After filtering Figure 6.6 to discard machine designs that are larger than

$70\times70\,\mathrm{cm}^2$, the results shown in Figure 6.7 reveal that there are systems that can meet this smaller form factor specification and most importantly, the high 3D overlap region of interest is still occupied by many of them, apart for the 9-FPS designs. As expected, the effect of this size specification was the general loss of designs with wide angular range when the maximum panel angle is used and the discarding of the majority of the designs with 9 FPSs regardless of panel angle. The rest of the designs were already below that size limit so their metric space remained unaltered. The value of the size limits was arbitrary and used for demonstration purposes.

Finally, to address the density of projections mentioned above, the emitter pitch can be filtered to force an empirically found safe threshold. Figure 6.8 shows designs that have 1.5 cm emitter pitch or larger as well as having the small form factor from Figure 6.7. Like before, many of those designs occupied the high 3D overlap region of interest and full cone angles around 20° offered the best performance after all the aforementioned specifications have been met. The range of possible full cone angles was also reduced for most FPS arrangements and in general, the effect of this extra emitter pitch specification was the loss of designs with high 3D overlap and relatively narrow angular ranges.

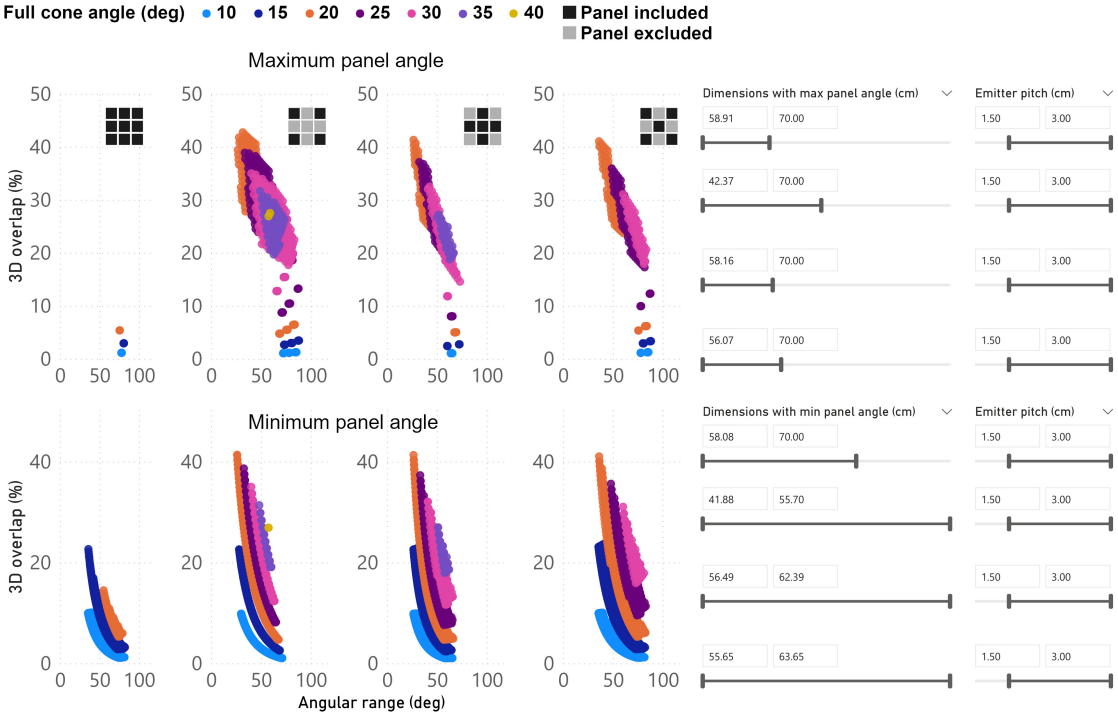

FIGURE 6.8: The irradiation metrics from Figure 6.7 but only for geometries with emitter pitch $\geq 1.5\,\mathrm{cm}$. Every column of value sliders corresponds to the row of plots on its left. Sliders have the same maximum length in each row for illustration purposes but correspond to different maximum numerical ranges. The numerical range of each slider is shown by the minimum and maximum values above it and is also represented by the relative position of the slider within its maximum length.

The designs in Figure 6.8 that offer the maximum 3D overlap with at least 30° angular range are listed in Table 6.6. To begin with, the solutions returned by Ipioni

for the 5-FPS system with the corner panels were the same for both the widest and narrowest panel angle. Therefore, 5 FPSs with the specifications on Table 6.6 cannot be integrated into a multi-FPS system in any other way otherwise some of the acceptance criteria will not be met.

TABLE 6.6: The parameters of the optimum designs from Figure 6.8 and their irradiation metrics.

Panel arrangement	9	5-corners	5-sides	4	9	5-corners	5-sides	4
	With maximum panel angle				With minimum panel angle			
Full cone angle (deg)	20	20	20	20	15	20	25	25
SID (cm)	43	98	97	100	99	98	78	79
Emitter pitch (cm)	1.8	1.5	1.6	1.5	1.8	1.5	1.5	1.5
Panel angle (deg)	17	15	13	13	12	15	13.5	12.5
Angular range (deg)	75.74	36.13	31.04	31.76	35.96	36.13	33.2	32.82
Detector illumination (%)	97.4	85.07	83.99	85.07	92.21	85.07	83.56	85.07
2D overlap (%)	11.08	55.34	53.05	57.26	30.53	55.34	54.58	56.19
3D overlap (%)	5.37	41.04	39.16	42.73	22.66	41.04	37.3	38.65
Irradiation non-uniformity (cm^2)	0.09	0.20	0.177	0.23	0.12	0.20	0.175	0.232
Device length (cm)	67.43	59.28	67.32	54.07	69.92	59.28	60.4	46.65
Device width (cm)	67.43	59.28	67.32	54.07	69.92	59.28	60.4	46.65
Device height (cm)	52.94	107.57	105.36	109.20	107.91	107.57	86.42	88.1
Panel-detector distance (cm)	33.06	88.43	88.64	90.80	90.09	88.43	69.58	69.9
Panel-patient distance (cm)	5.06	68.43	60.64	62.80	62.09	60.43	41.58	41.9

All designs have full cone angle close to 20° and 5 of them have an SID close to the maximum allowed 100 cm. Moreover, the emitter pitch is between 1.5 and 1.8 cm with 5 of the systems having the lowest allowed 1.5 cm. Unexpectedly, a narrower panel angle offered wider angular range for the systems with 5 and 4 FPS but this difference was less than 3°. The angular range of these systems was between 30° and 40°. A larger difference was observed with the 9-FPS system where the wider panel angle produced a 75.74° angular range, almost 40° wider than with a narrow panel angle. Also, panel angle was always narrower than the full cone and at least 83% of the detector area was illuminated with all designs. This percentage was practically the same with both panel angles and close to 83-85% for all but the two 9-FPS systems which reached values above 92%. Furthermore, all but the 9-FPS systems had 2D overlap close to 55% and 3D overlap close to 40%. No more than 5% change was observed in these metrics between the wide panel angle and the narrow panel angle versions. Furthermore, the irradiation uniformity improved with more panels (i.e. more emitters). With the 9-FPS system the non-uniformity improved by 25% by using a wide panel angle whereas a much smaller change was observed in the rest of the systems. Moreover, the device dimensions shrank with the narrower panel angles for the DT systems with 4 and 5 FPS but instead more than doubled with the 9-FPS system. Finally, the 9-FPS system with the widest panel angle barely overcomes the 5 cm minimum patient clearance threshold whereas all the other designs leave much more room for patient positioning. 3D models and the X-ray beam density inside the patient and on the detector from all these designs are shown in Figure 6.9.

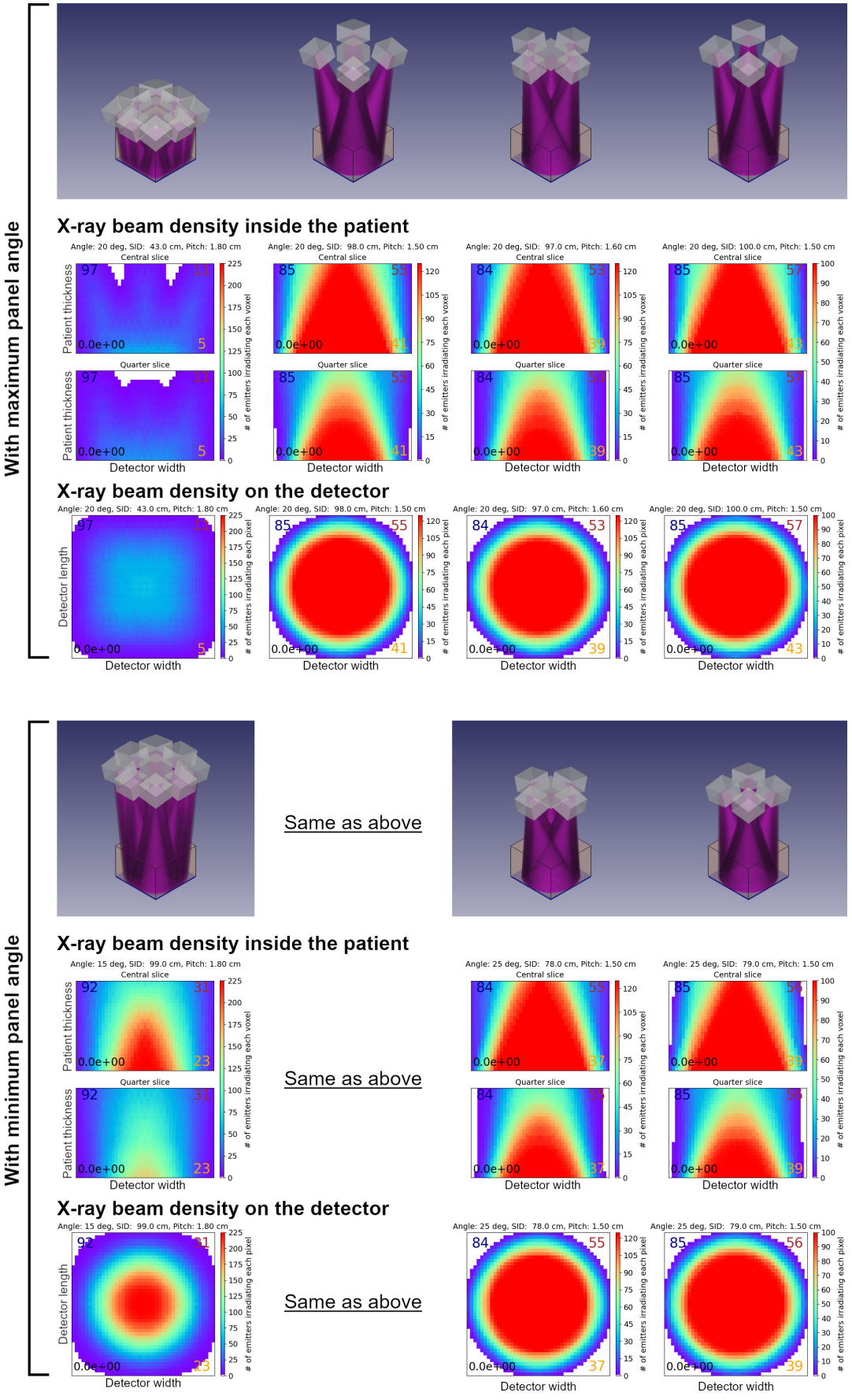

FIGURE 6.9: 3D models and X-ray beam density inside the patient and on the detector of the designs in Table 6.6.

The 3D models and the X-ray fields in Figure 6.9 show that full irradiation of the patient or the detector has not been achieved and that the best illumination in terms of detector coverage come from the 9-FPS system with the widest panel angle. However, due to the distribution of the X-ray beams inside the patient and on the detector, the beam overlap of that system was largely inferior to that of all the rest. The colour scales have been kept different for each plot so that the beam density for each DT system can be compared to their respective hottest spot possible (100% 2D overlap and 3D overlap). With this in mind, the hot spots were shaped almost identical with all systems apart from the 9-FPS ones.

This similarity was also expressed in the similar values of detector illumination, 2D and 3D overlap. Moreover, the worst beam overlap was observed with the 9-FPS system with the widest panel angle, followed by its narrow panel angle equivalent and then followed by the other configurations. This trend was also observed on the 2D and 3D overlap metrics, showing that these metrics may be a good single-value representation of the beam overlap instead of anything that requires visual examination.

Lastly, 3D versions of Figure 6.6 are shown in Figure 6.10 and Figure 6.11 with SID and emitter pitch as the third dimension respectively, showing how these specifications affect 3D overlap and angular range.

In Figure 6.10, 3D overlap increased with larger SID and, at a constant SID, wider full cone angles offered higher 3D overlap since there is a larger degree of overlap when beams are wider. However, values between 20° and 25° were those that produced acceptable geometries that reached the highest possible 3D overlap values. Wider full cone angles were limited to shorter SIDs due to X-ray field size constrains thus 3D overlap was likewise limited. Moreover, wider panel angles made the proportionality between 3D overlap and SID less strict, as witnessed by the more spread-out phase space of these metrics with wider panel angles. This spreading of the metric space was more pronounced with fewer emitters (i.e. fewer FPSs) and this was also observed in the metric space of 3D overlap and angular range, as mentioned before for Figure 6.6.

On the other hand, in Figure 6.10 angular range decreased with larger SID and, at a constant SID, wider full cone angles generally reduced the angular range due to the rules from Table 6.3. Wider full cone angles projected wider X-ray fields on the detector thus the FPS was transported laterally by a shorter (x_i,y_i), which decreased the angular range. But narrow panel angles caused the SID-angular range projections from different full cone angles to be stacked on top of each other, meaning that full cone angle had essentially no effect on angular range when narrow panel angles were used. On the other hand, the wider panel angles deconvolved the SID-angular range projections from different full cone angles, so wider full cone angles generally reduce the angular range as mentioned before but also make the proportionality between angular range and SID less strict, as witnessed by the more spread-out phase space of these two metrics with wider panel angles. This spreading of the metric space was also more pronounced with fewer emitters (i.e. fewer FPSs), as mentioned before for Figure 6.6.

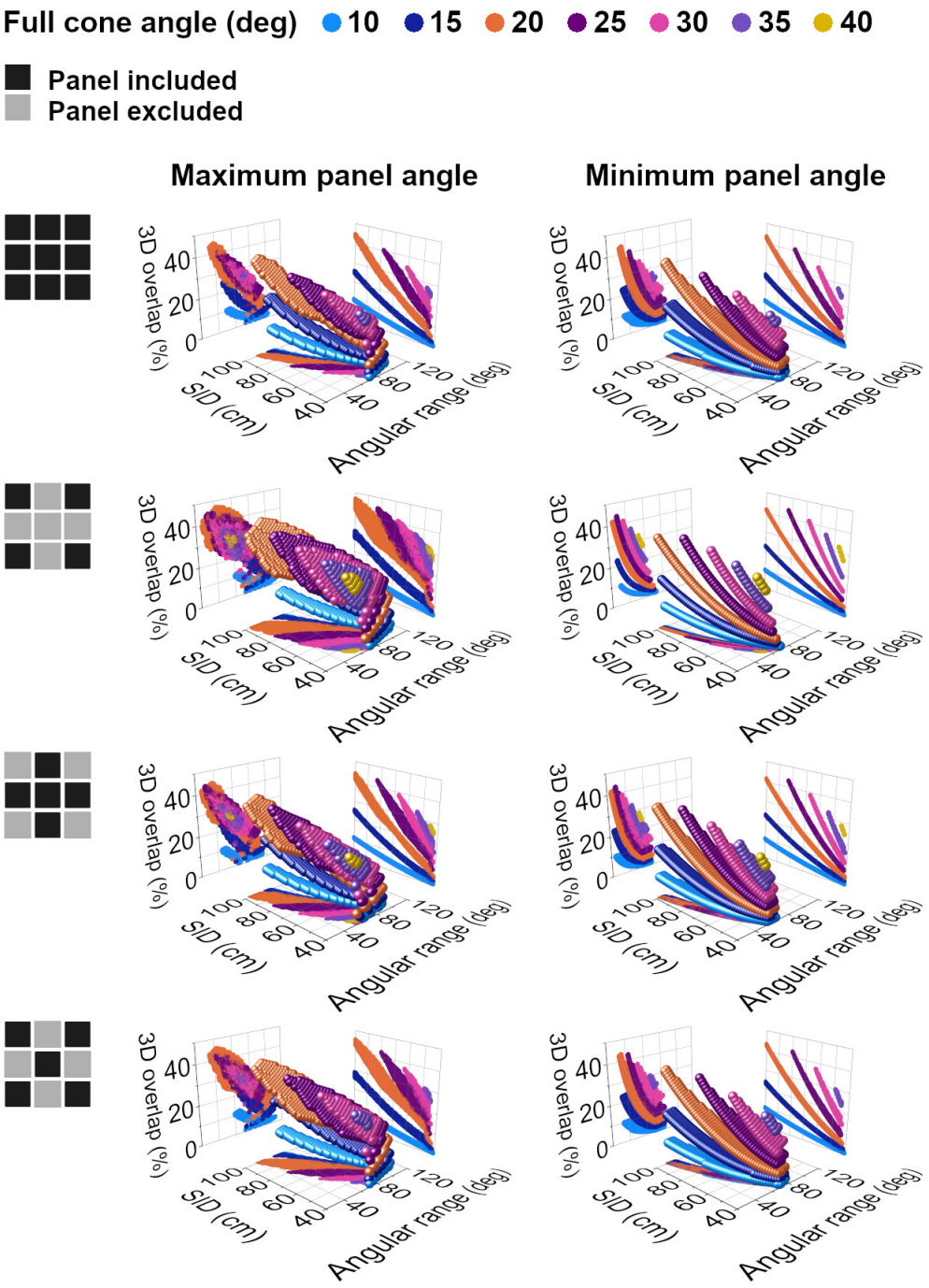

FIGURE 6.10: The effect of SID, full cone angle and panel angle on 3D overlap and angular range of different chest DT systems with $18\times18\times13\,\mathrm{cm}^3$ FPSs. In all cases, increasing the SID and the cone angle improves 3D overlap but full cone angles close to 20° offer the maximum 3D overlap. Narrower angular ranges are achieved with taller SIDs in all cases. Also, increasing the cone angle generally narrows the range of angular range values. Moreover, wider panel angles create more widely spread metric spaces, giving greater flexibility in choosing the optimum design. This spreading is most pronounced with fewer FPSs. All these suggest that the choice of full cone angle and SID will greatly affect the performance of the multi-FPS system and can largely limit the options for multi-FPS designs, especially when more FPSs are used and at narrower panel angles to save space. See Figure 6.11 for the equivalent figure with emitter pitch.

So, in general, 3D overlap was highly dependent on the SID and the full cone angle but this dependence became less strict with fewer emitters and wider panel angles. Angular range was also highly dependent on the SID and the full cone angle but in an opposite manner to 3D overlap, and this dependence became less strict with fewer emitters and with wider panel angles.

The impact of emitter pitch on 3D overlap and angular range is shown in Figure 6.11. The metric spaces were generally shaped like groups of sheets relatively parallel to the emitter pitch dimension and normal to the 3D overlap-SID projection plane. The sheets were more skewed when fewer panels and when wide panel angles were used and this was also expressed as the more widely spread projection on the 3D overlap-SID plane as mentioned before. This meant that a change in emitter pitch caused almost no changes in the 3D overlap when many emitters were involved and panel angles were narrow but relatively small changes were generated otherwise, with the larger change observed when only 4 panels were used. The effect of emitter pitch was mostly the reduction of the maximum achievable 3D overlap with gradually larger pitch without any other effects on the smaller values.

Furthermore, the 3D metric spaces in Figure 6.11 were stacked on top of each other with reference to the angular range-emitter pitch projection plane. Regardless of how skewed they were, their projections on the angular range-emitter pitch plane were convolved, across a wide range of angular range values with wide panel angles and more narrow range of angular range values with narrow panel angles. This meant that that regardless of panel angle and full cone angle, emitter pitch had practically no effect on the angular range. The most profound effect of emitter pitch on the angular range was that larger emitter pitch values gradually converged the minimum and maximum allowed angular ranges, expressed by the triangle sheet-like shape of the metric spaces.

So, in general, emitter pitch affected 3D overlap mostly when there were few emitters and panels were widely angled and its most profound effect was that it limited the highest achievable 3D overlap without affecting the rest of the values. Also, emitter pitch affected angular range mostly when there were few emitters and panels were widely angled and its most profound effect was that it limited the highest and lower achievable angular range without affecting the rest of the values in any major way.

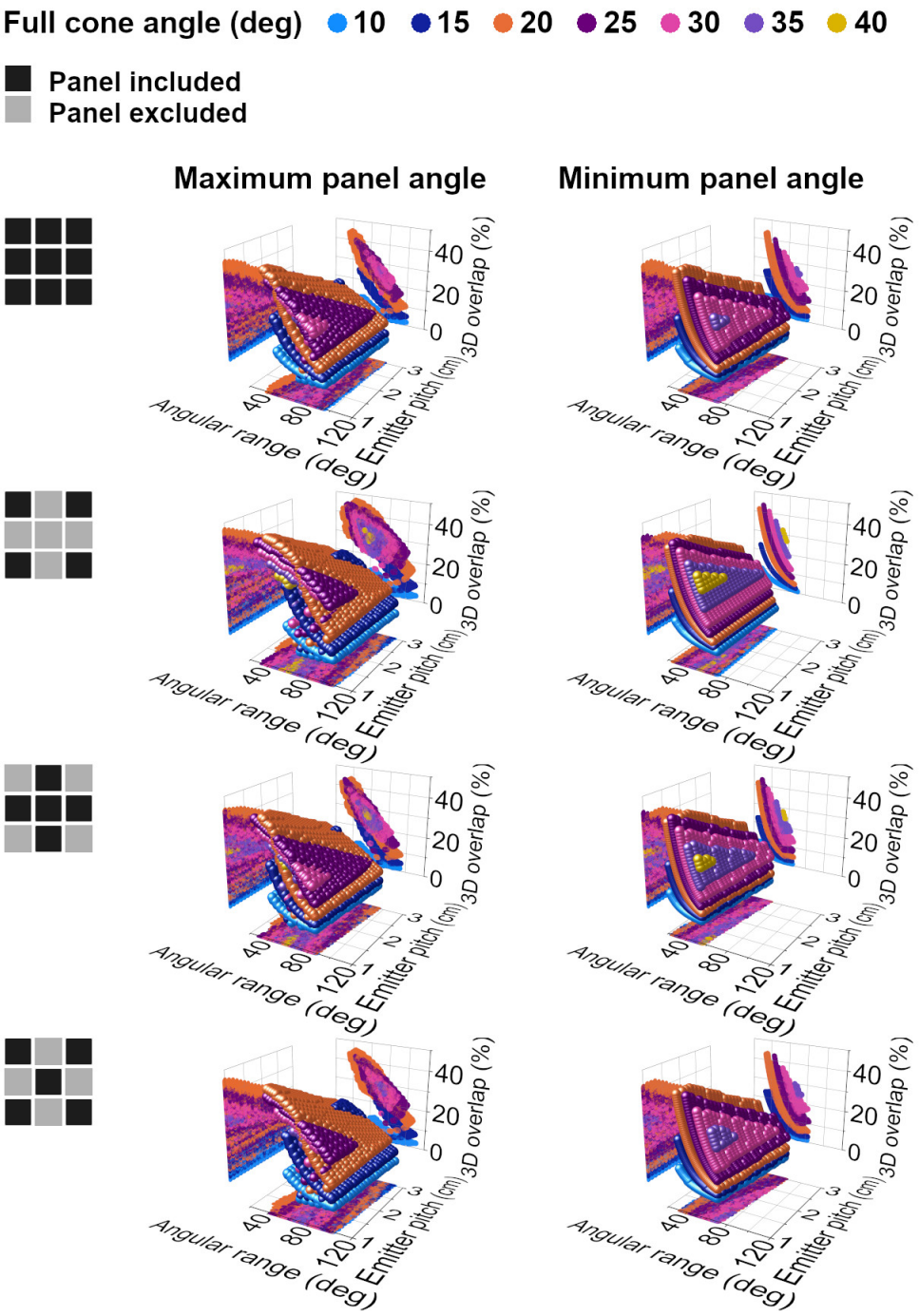

FIGURE 6.11: The effect of emitter pitch, full cone angle and panel angle on 3D overlap and angular range of different chest DT systems with $18\times18\times13\,\text{cm}^3$ FPSs. In all cases, increasing the emitter pitch removes the higher values of 3D overlap without affecting the lower values. On the other hand, it removes the lower values of angular range without greatly affecting the larger values. So, emitter pitch mostly affects the ranges of possible values of 3D overlap and angular range and does not force specific values. Similarly to Figure 6.10, wider panel angles generate more widely spread metric spaces offering greater flexibility in the choice of emitter pitch, on top of the existing light dependence of designs on the emitter pitch. Finally, this spreading of the metric space is more pronounced with fewer FPSs. All these suggest that, contrary to SID and cone angle, emitter pitch could be chosen during the design of the FPS without this choice being a strictly limiting factor on the design of the multi-FPS integrated system.

Finally, irradiation non-uniformity appeared to be a good metric that combined both angular range and density of projections as shown in Figure 6.12. The metric was oppositely proportional to angular range and oppositely proportional to the number of emitters which is an indirect measure of projection density. Also, irradiation non-uniformity differentiated between the two 5-FPS systems, giving better (lower) values of non-uniformity with the version that had the side FPSs compared to the corner FPSs for angular ranges bellow 60°. This could have been due to the fact that the corner FPSs on the 5-FPS system are rotated around their respective diagonal and the side FPSs on the other 5-FPS system are rotated around one of their sides. Since the largest distance between any two neighbouring emitters on the array is their diagonal distance, this distance is expected to have a large impact on the irradiation non-uniformity. And when emitters are projected onto a unit sphere, the diagonal distances of their projections shrink at a greater degree when the emitters belong to the corner panels than when they belong to side panels due to which axis is the rotation axis. Therefore, the emitter projections are clustered more closely instead of being more widely distributed with the corner panels, so the standard deviation of the areas of the Voronoi cells becomes larger and thus non-uniformity increases. The dependence of irradiation non-uniformity on the different FPS arrangements was maintained across all values of angular range but the 4- and 5-FPS plots gradually converged at larger values. Also, the data points were spread more widely at larger values with the wide panel angle meaning that other factors started affecting that metric at large angular ranges.

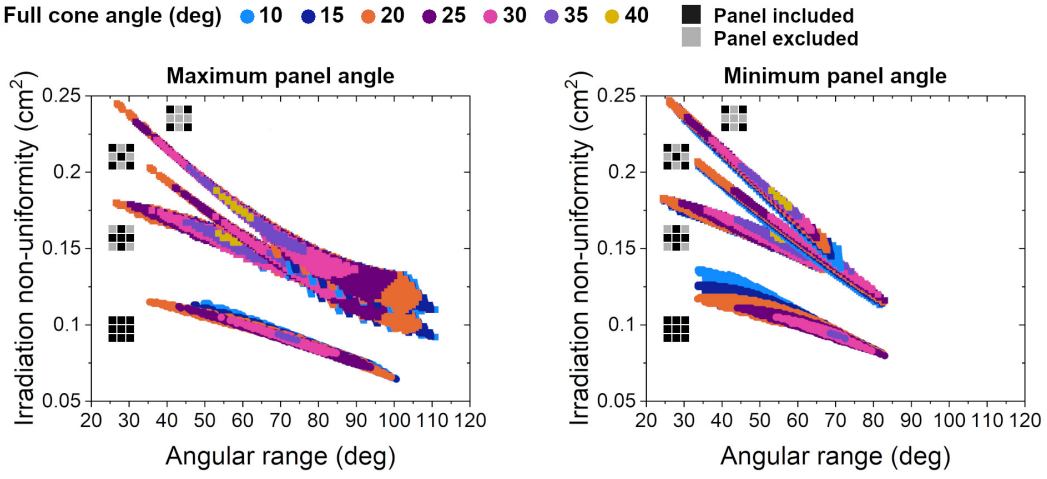

FIGURE 6.12: Correlation between irradiation non-uniformity and angular range with different chest DT system designs with $18\times18\times13\,\mathrm{cm}^3$ FPSs. The two metrics are proportional but irradiation non-uniformity can also discriminate between systems that have the same angular range and different irradiation geometry. The 9-FPS systems generally outperform the rest and wider panel angles allow for better (lower) values of irradiation non-uniformity. However, near the 30° angular range region of interest, the two metric spaces are generally the same. Also, increasing the cone angle generally removes the low and high ends of the metric spaces. Finally, the distributions become more spread at high angular ranges with wide panel angles suggesting that other factors start having an effect on irradiation non-uniformity.

6.5.3 Results with 28×28×13 cm^3 flat panel sources

The same process was followed with the 28×28×13 cm^3 FPSs. 4,445, 3,721 and 2,885 designs were found for systems with 4 FPSs, 5 FPSs with the side panels and 5 FPS with corner panels respectively and the results are shown in Figure 6.13. This time, there were no possible designs that included all 9 FPSs and the distribution of the possible designs on the irradiation metrics phase space is narrower. The number of designs is also considerably smaller compared to the equivalent with the smaller panels (4,832, 4,726 and 4,189 respectively). All these mean that with larger panels there is less flexibility in choosing the device specifications.

Emitter pitch could still have any value between 1 and 3 cm but the full cone angle was limited to values smaller than 40° and in terms of machine size the designs were less compact than their equivalents with 18×18×13 cm^3 FPSs. However, in all cases, the high 3D overlap region was occupied by several designs and, like before, the vast majority of designs had angular range above 30°.

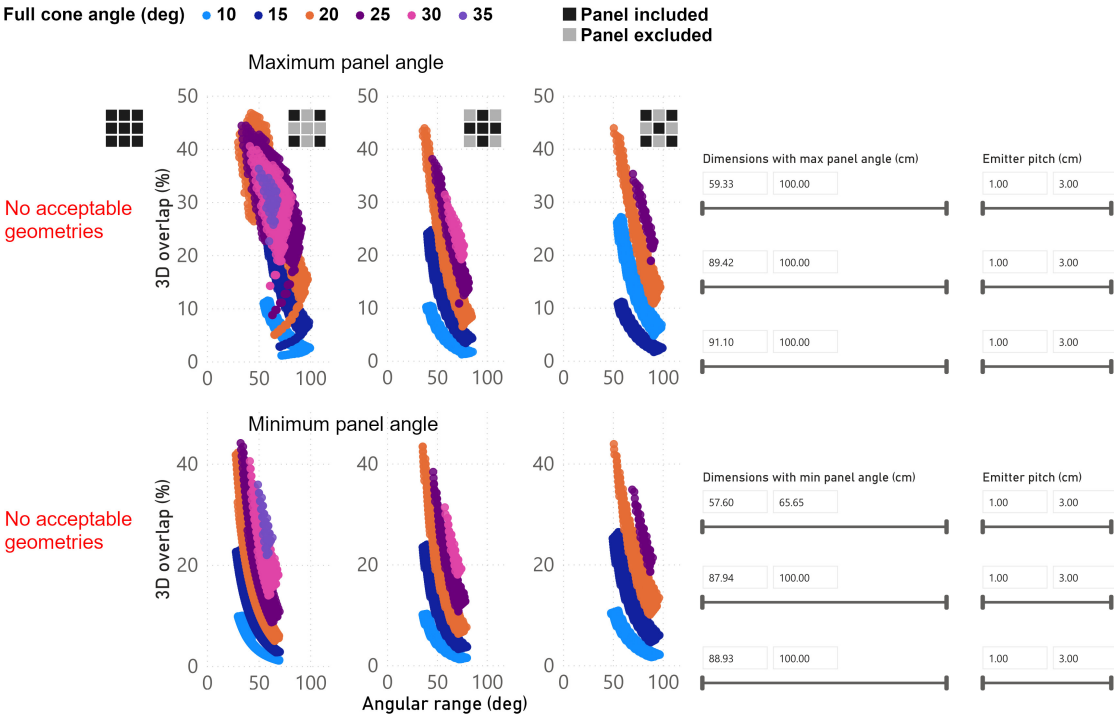

FIGURE 6.13: Ipioni-generated irradiation metrics of the acceptable geometries found with the parameter scan from Table 6.5 with 28×28×13 cm^3 flat panel sources. Every point is a geometry with unique values for the parameters in Table 6.1. Every column of value sliders corresponds to the row of plots on its left. Sliders have the same maximum length in each row for illustration purposes but correspond to different maximum numerical ranges. The numerical range of each slider is shown by the minimum and maximum values above it and is also represented by the relative position of the slider within its maximum length.

Changing the device size specification to have length×width no wider than 90×90 cm^2 produces the results shown in Figure 6.14. Now, there are only narrow panel angle DT systems that have 5 FPSs in a diagonal cross configuration and they all have 10° full

cone angle. Also, the 5-FPS designs with 4 panels on the sides are practically limited to the narrowest panel angles except for a few exceptions which can use wider panel angles. Finally, many 4-FPS designs with relatively narrow full cone angles have been lost when the panel angle is at its widest whereas the metric space of 4-FPS systems with the narrowest panel angle remained unaltered. All in all, the high 3D overlap region of interest is now occupied by fewer solutions and as with the smaller panels, solutions with wider angular ranges were eliminated first while gradually reducing the total size specifications. Like before, the choice of 90 cm was arbitrary and used for demonstration purposes.

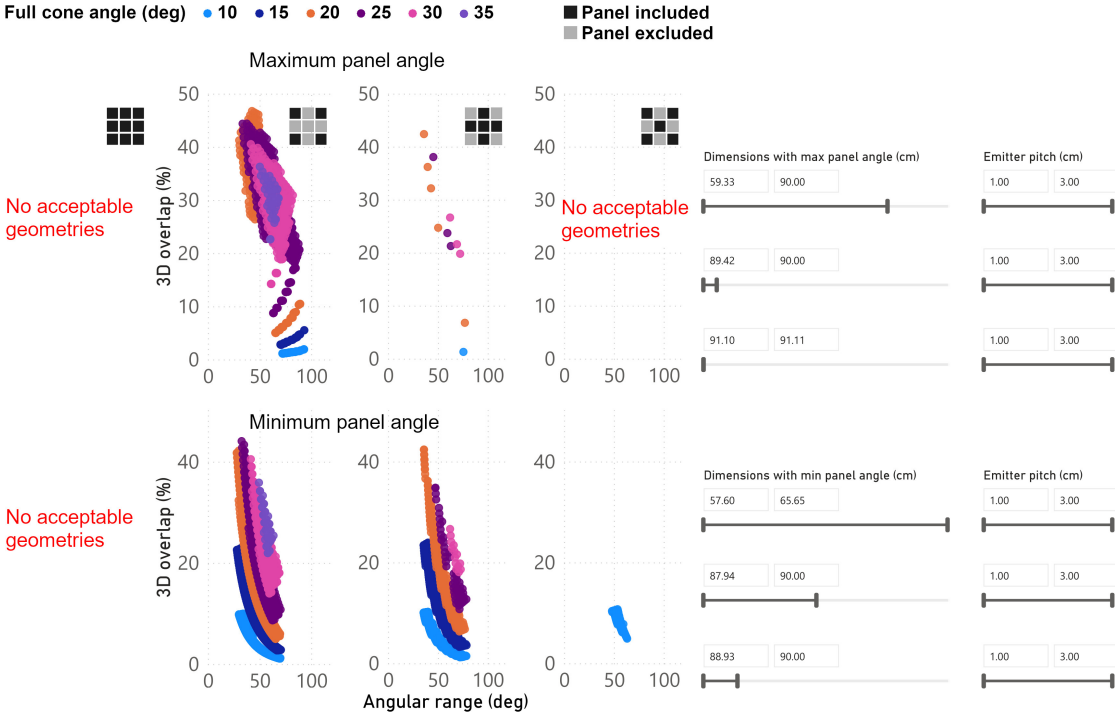

FIGURE 6.14: The irradiation metrics from Figure 6.13 but only for geometries with length × width $\leq 90 \times 90\,\text{cm}^2$. Every column of value sliders corresponds to the row of plots on its left. Sliders have the same maximum length in each row for illustration purposes but correspond to different maximum numerical ranges. The numerical range of each slider is shown by the minimum and maximum values above it and is also represented by the relative position of the slider within its maximum length.

Forcing an emitter pitch value of 1.5 cm or greater, as it was done with the smaller FPSs, produced the results which are shown in Figure 6.15. The effect of this specification was the loss of solutions with relatively high 3D overlap which was an expected outcome as it was with the smaller FPSs. Also, full cone angles close to 20° still appeared to offer the best performance. After all these specifications were enforced, only 4 and 5 FPSs in very specific configurations could meet them and these solutions were more limited with 5 FPSs compared to the 4-FPS ones. The designs from Figure 6.15 that produced the highest 3D overlap with an angular range of at least 30° for each FPS configuration are listed in Table 6.7.

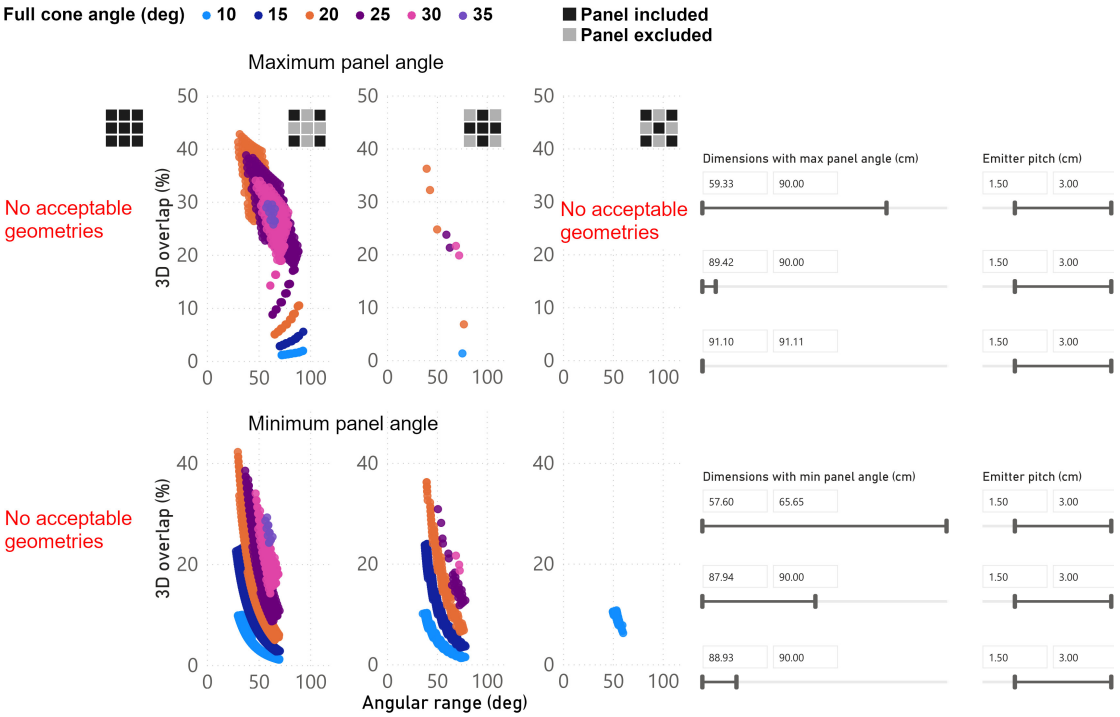

FIGURE 6.15: The irradiation metrics from Figure 6.14 but only for geometries with emitter pitch ≥ 1.5 cm. Every column of value sliders corresponds to the row of plots on its left. Sliders have the same maximum length in each row for illustration purposes but correspond to different maximum numerical ranges. The numerical range of each slider is shown by the minimum and maximum values above it and is also represented by the relative position of the slider within its maximum length.

TABLE 6.7: The parameters of the optimum designs from Figure 6.15 and their irradiation metrics.

Panel arrangement	9	5-corners	5-sides	4	9	5-corners	5-sides	4
	With maximum panel angle				With minimum panel angle			
Full cone angle (deg)			20	20		10	20	20
SID (cm)			92	100		100	92	99
Emitter pitch (cm)			1.7	1.5		2.8	1.7	1.5
Panel angle (deg)			17	13		18	17	12
Angular range (deg)			39.7	31.76		53.66	39.7	30.22
Detector illumination (%)			83.99	85.07		96.32	83.99	85.07
2D overlap (%)			50.06	57.26		14.67	50.06	55.44
3D overlap (%)			36.18	42.73		10.73	36.18	41.24
Irradiation non-uniformity (cm^2)			0.172	0.233		0.168	0.172	0.237
Device length (cm)			89.42	64.07		89.97	89.42	61.51
Device width (cm)			89.42	64.07		89.97	89.42	61.51
Device height (cm)			102.31	110.79		112.3	102.31	109.47
Panel-detector distance (cm)			81.69	89.21		87.7	81.69	88.53
Panel-patient distance (cm)			53.69	61.21		59.7	63.69	60.53

The optimum design with the 5-FPS system with the side panels is the same with the wide and the narrow panel angle. Also, for the 4-FPS system, the wide and narrow panel angle solutions were almost identical across all metrics and device specifications. Moreover, the results of the 4-FPS system are close to those of the 5-FPS system with the side panels. All these suggest that the larger size of the FPSs largely limits the flexibility on the choice of multi-FPS designs. Moreover, although the 5-FPS system

with the corner panels had similar characteristics to the rest of the designs in terms of dimensions, it had a largely inferior performance. The combination of narrow cone angle and wide emitter pitch offered superior detector coverage but greatly reduced 2D and 3D overlap, although angular range was much wider and irradiation non-uniformity was slightly better than the other designs. 3D models and maps of the X-ray beam density in the patient and on the detector of the optimum designs from Table 6.7 are shown in Figure 6.16.

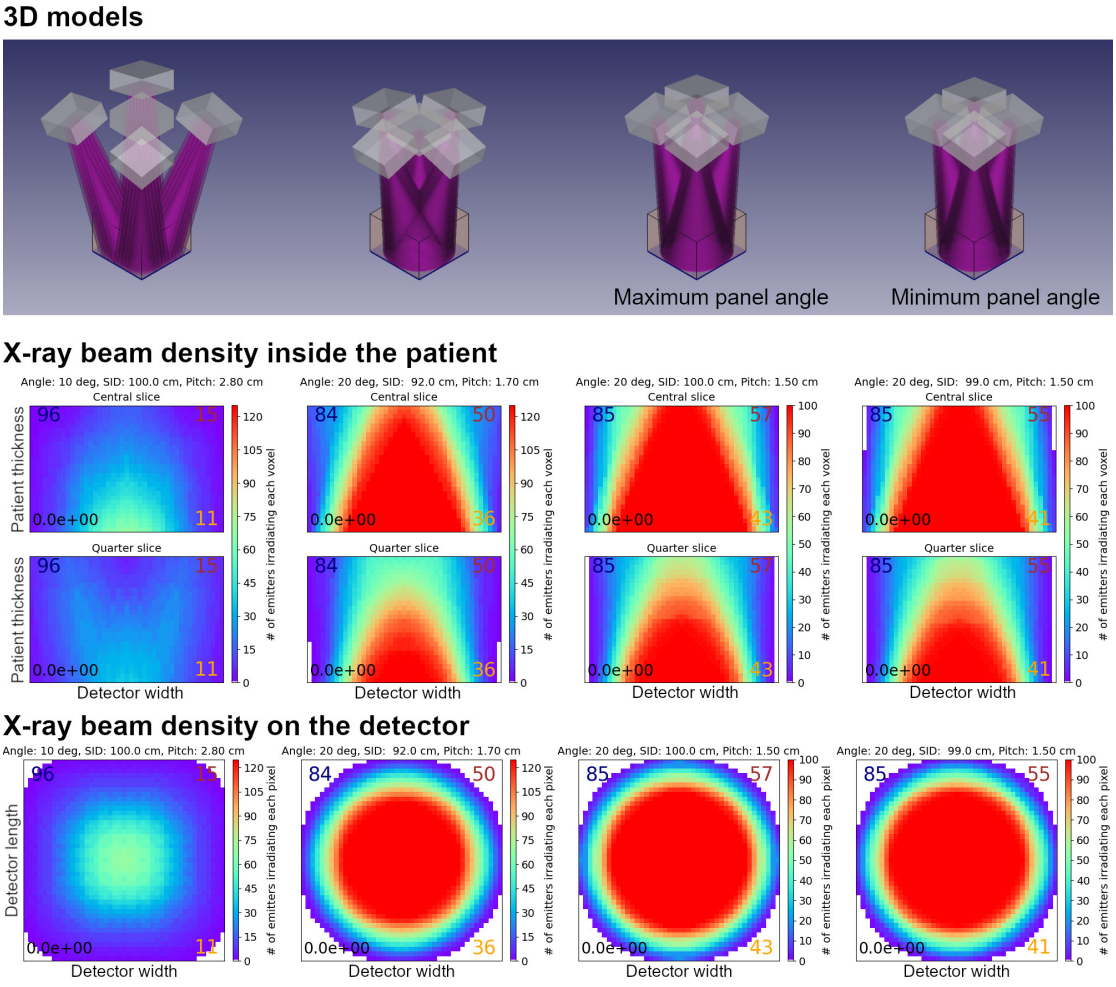

FIGURE 6.16: 3D models and X-ray beam density inside the patient and on the detector of the designs in Table 6.7.

Lastly, 3D versions of Figure 6.13 are shown in Figure 6.17 and Figure 6.18 with SID and emitter pitch as the third dimensions, showing how these specifications affect 3D overlap and angular range.

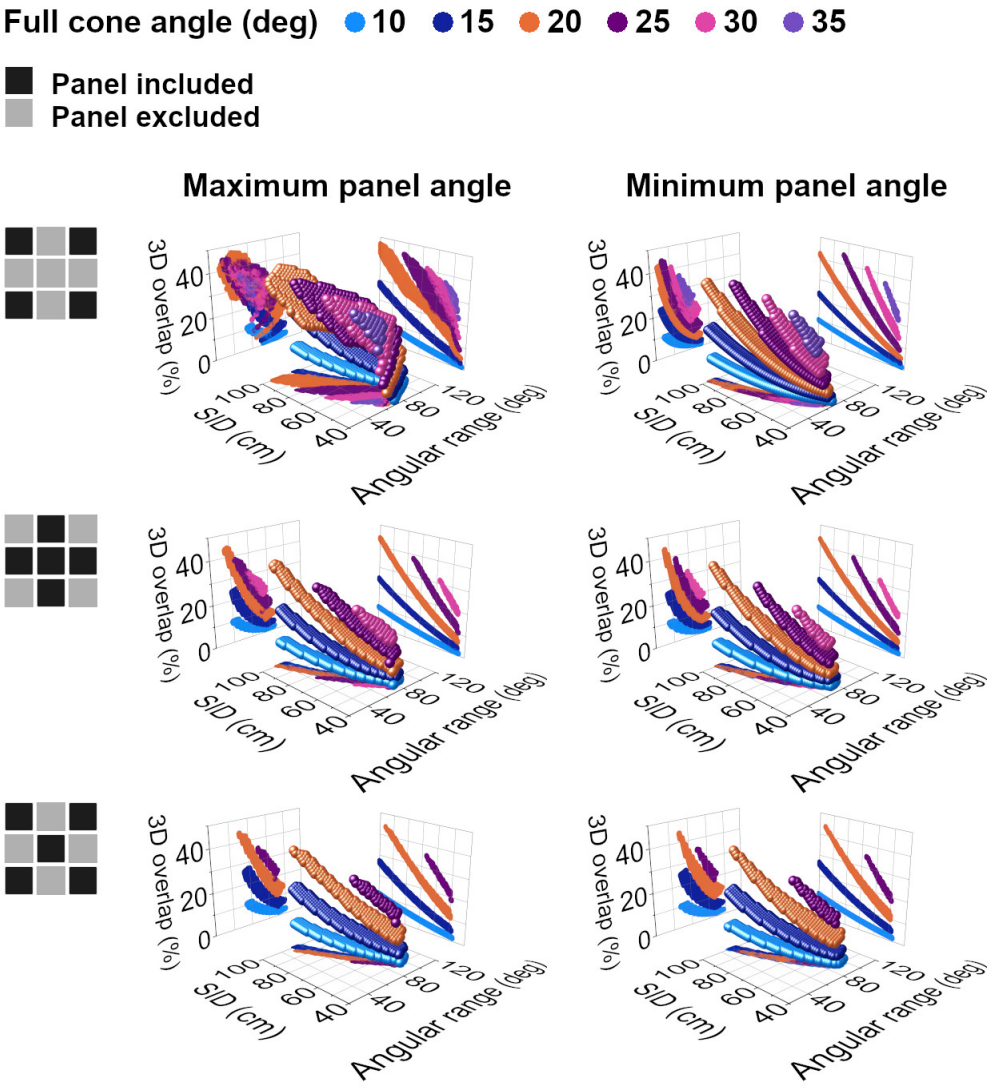

FIGURE 6.17: The effect of SID, full cone angle and panel angle on 3D overlap and angular range of different chest DT systems with $28\times28\times13\,\mathrm{cm}^3$ FPSs. The data trends are similar to those from the smaller panels in Figure 6.10 and a full cone angle close to 20° still produces the highest 3D overlap. But the metric spaces with wide and narrow panel angles are now similar to each other and relatively constrained instead of spread out, apart from the 4-FPS metric spaces. This indicates that the larger FPS size comes with stricter limitations on the choice of multi-FPS designs, compared to the smaller FPSs. See Figure 6.18 for the equivalent figure with emitter pitch.

The conclusions generally remain the same as with the smaller FPSs. However, there were no designs with 40° full cone angle or with 9 FPSs. The 3D metric space maintained the sheet-like shape for each full cone angle in the same manner as with the smaller FPSs. Also, 3D overlap remained heavily dependent on SID and full cone angle with this dependence being less strict with 4 FPSs at a wide panel angle as expressed by the wider spread of the metric space. Moreover, apart from the 4-FPS system with wide panel angle, the metric spaces were similar regardless of panel angle and they were more compact than those with the smaller FPSs shown in Figure 6.10. This indicates

that the larger FPSs used here not only allow for fewer possible designs but they also limit the flexibility in choosing design specifications.

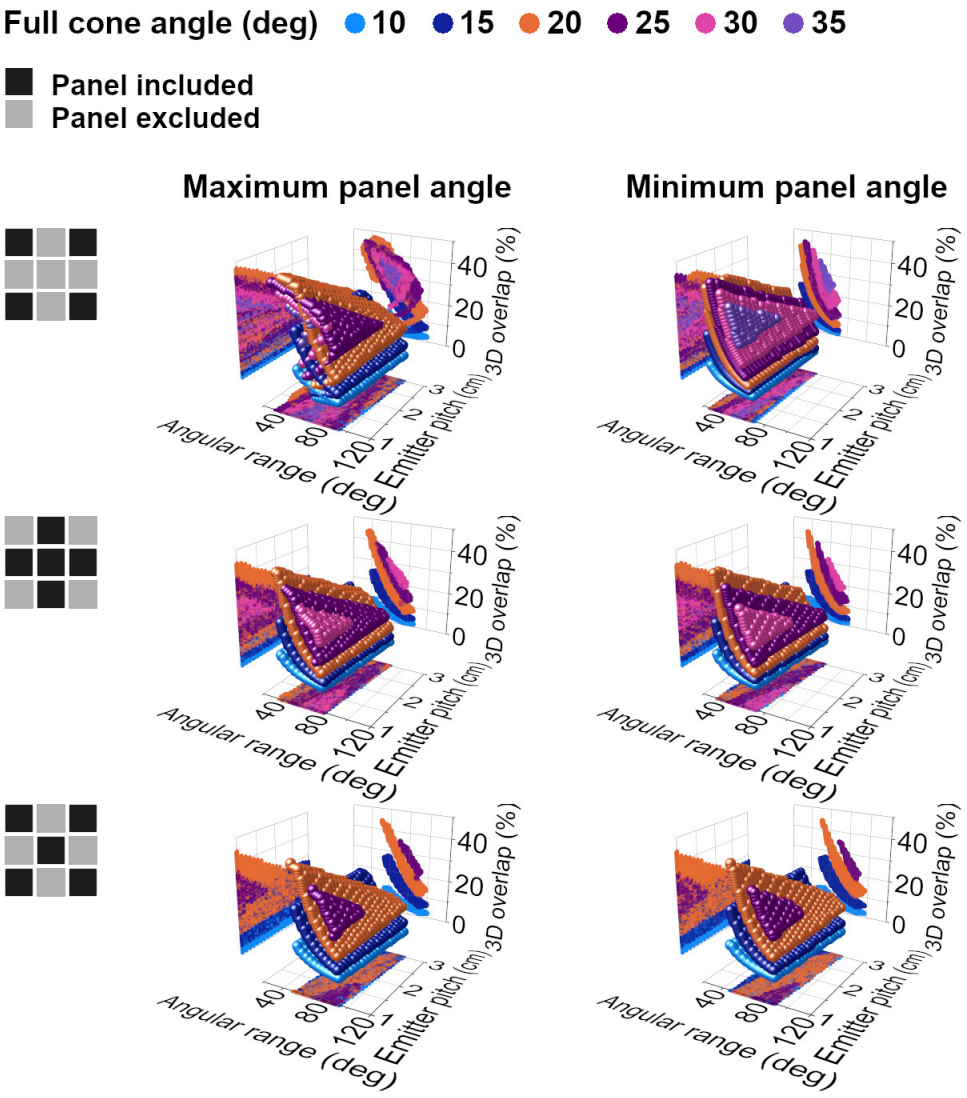

FIGURE 6.18: The effect of emitter pitch, full cone angle and panel angle on 3D overlap and angular range of different chest DT systems with $28\times28\times13\,\text{cm}^3$ FPSs. The data trends are similar to those from the smaller panels in Figure 6.11. Increasing the emitter pitch removes the higher values of 3D overlap without greatly affecting the lower values. It also removes the lower values of angular range without greatly affecting the larger values. So, emitter pitch mostly affects the ranges of possible values of 3D overlap and angular range and does not force specific values. As also observed in Figure 6.17, the metric spaces with wide and narrow panel angles are similar to each other and relatively constrained instead of spread out, apart from the 4-FPS metric spaces. All the above indicate that the larger FPS size comes with stricter limitations on the choice of multi-FPS designs, compared to the smaller FPSs, but the choice of emitter pitch during the design of the FPS would still not be a strictly limiting factor on the design of the multi-FPS integrated system.

In Figure 6.18, increasing the emitter pitch reduced the range of possible 3D overlap values, mostly the high values. A similar effect was observed on angular range but this time low values were removed. This indicates that emitter pitch has much less impact on

system performance than cone angle and SID. Moreover, as observed before, the metric spaces were similar between wide and narrow panel angle apart from the 4-FPS systems. This is a result of the aforementioned fewer possible designs and limited flexibility in design specifications.

Finally, irradiation non-uniformity has the same proportionality features with angular range and the number of emitters as it was shown with the smaller FPSs. The spreading of the metric space at high angular ranges with the wide panel angle is also smaller due to the design limitations mentioned before. However, near the 30° angular range region of interest, the two metric spaces are generally similar. So, apart from the exact numerical values, the general conclusions remain the same with the two different sizes of FPSs.

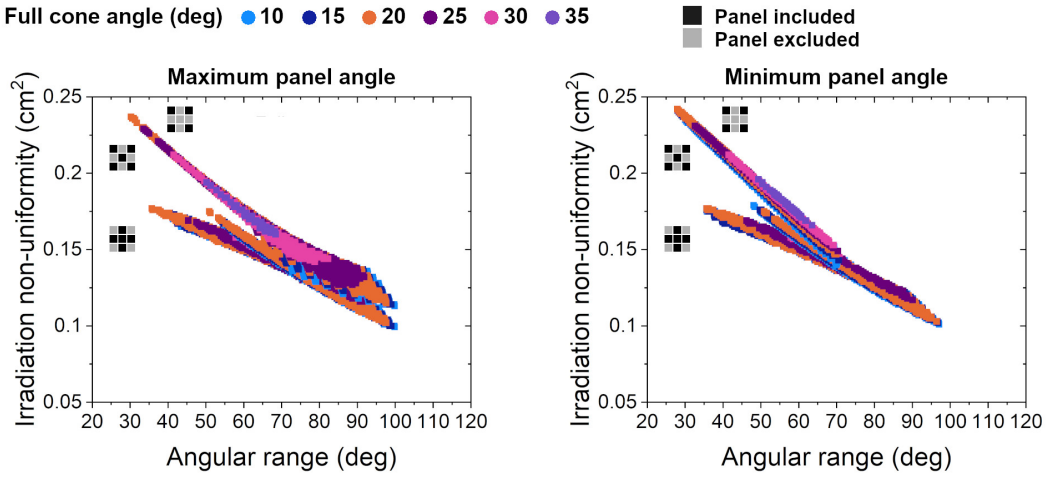

FIGURE 6.19: Correlation between irradiation non-uniformity and angular range with different designs of a chest DT system with $28\times28\times13\,\mathrm{cm}^3$ FPSs. The results are generally similar to those from Figure 6.12. Angular range and irradiation non-uniformity are proportional to each other and irradiation non-uniformity can discriminate between systems that have the same angular range but different irradiation geometry. However, due to a lower maximum angular range with the larger FPSs, wider panel angles now allow for better (lower) irradiation non-uniformity mostly on the 4-FPS system instead of all the designs. Nevertheless, near the 30° angular range region of interest, the two metric spaces are generally the same but now the 5-FPS system with the corner panels has a minimum possible angular range close to 50°. Finally, the phase space becomes more spread at high angular ranges, especially with wide panel angles suggesting that other factors start having an effect on irradiation non-uniformity.

6.6 Finding the optimum design among those shortlisted by Ipioni

As mentioned before, Ipioni can provide answers only to geometrical issues of multi-FPS DT system design and optimisation. However, this already narrows down the decision trees significantly as shown in the previous section. Ipioni scanned the tens of thousands of combinations of device specifications from Table 6.5, identified the few thousands that satisfy the acceptance criteria from Table 6.2 and calculated the multitude of irradiation

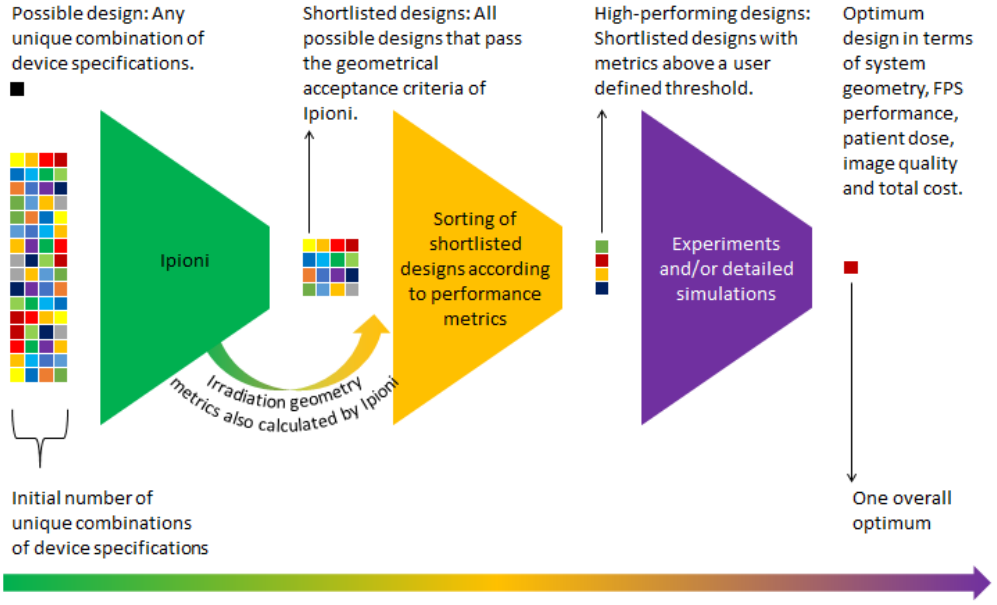

FIGURE 6.20: The role of Ipioni in the design and optimisation workflow of multi-flat-panel-source DT systems.

geometry metrics from Table 6.4 by which the designs could be sorted. All these results were saved on a file. On a step that was optional, several designs from that results file were then discarded by means of a database query that removed designs exceeding a user defined maximum size and having emitter pitch below a user defined threshold. These thresholds could have just been used as the values of their respective parameters at the start of the parameter scan and the results would have been the same. Then, choosing the best among the designs that were left was as simple as another database query that returned the designs which had the maximum 3D overlap as long as angular range was at least 30°. These are listed on Table 6.6 and Table 6.7.

To finalise the study and decide on a final optimum design among those, the handful of these designs could be replicated in the laboratory or in computer simulations like those in Chapter 5. This can provide further performance details such as patient dose and image quality. The role of Ipioni in this design and optimisation workflow is illustrated in Figure 6.20.

Without Ipioni, these experimental or computational studies would have to be performed with designs that are based on intuition, on empirical knowledge or on a limited amount of information perhaps acquired via slow and iterative trial and error. Due to the tens of thousands of prospective designs, it is obvious that such a task could easily fall short of the true optimum design specifications and would waste precious time, capital and resources. Instead, Ipioni scans the full width of the solutions space, identifies the solutions that are feasible in terms of a number of acceptance criteria and calculates irradiation geometry metrics to score each design with. Given access to HPC facilities this can be completed in a matter of hours, and from the results, those that have the highest performance can be immediately pipelined into further experimental tests or

detailed simulations to identify the overall optimum. Therefore, Ipioni's role is truly catalytical in the design and optimisation of the multi-FPS DT systems even if only geometrical issues are addressed.

However, due to the lack of appropriate tools at the time of writing of this thesis, an experimental replication was not possible. Also, lack of time did not allow detailed Monte Carlo simulations of the designs. As such, the final steps of this optimisation workflow were not added in this thesis. But nevertheless, the whole process described in the previous section was to demonstrate the capabilities of the code. The results were filtered by an arbitrary maximum device size and an arbitrary minimum emitter pitch since the true Adaptix specifications remain proprietary. As such, two examples of end-to-end use of Ipioni were shown in detail for demonstration purposes and it is now only a matter of replicating the exact steps and just replacing the demonstration values with the true Adaptix specifications. This work is done now by the QUASAR group and Adaptix during the development of the higher power FPS and results are expected soon.

In conclusion, Ipioni's role is to perform a parameter scan and shortlist candidate designs based on irradiation geometry metrics and geometrical acceptance criteria. It is then the user's responsibility to replicate the shortlisted designs in the laboratory or in detailed physics simulations to acquire information regarding patient dose and image quality. The choice of experiments or simulations is up to the user and does not depend on the solutions generated by Ipioni. Nevertheless, all the geometrical specifications needed to replicate the shortlisted designs in experiments or simulations are automatically exported by the code during the shortlisting parameter scan. So, after Ipioni has identified those candidate designs, there is no extra step before they are realised in the laboratory or replicated in computer simulations and this allows a seamless transition from Ipioni to the experimental or computational studies. As such, the end result of using Ipioni is a quick and simple design and optimisation workflow for multi-FPS DT systems that is developed from scratch based upon just a handful of acceptance criteria. This makes Ipioni a perfect tool during the introduction of a novel 3D X-ray imaging system that has never been seen before and thus there is no prior knowledge to build it upon. Finally, the fact that Ipioni has already identified and characterised an extensive range of 3D X-ray imaging products which have not been built yet clearly demonstrates its power as an early-stage design and optimisation tool that can significantly accelerate R&D and bring down cost and time to commercialisation.

6.7 Discussion

Ipioni involves a lot of calculations of trigonometric functions, including the intersections of cones and planes and the discretisation of results into pixel and voxel elements. Numerical imprecisions are therefore expected however since the designs exported by

the code appear as expected in 3D using FreeCAD, these imprecisions are deemed negligible at this early stage of development. Of course, the code allows finer pixel and voxel meshes and the examples given here were just for demonstration.

After performing the parameter scans for both sizes of FPSs, full cone angle, SID and panel angle were found to have much greater effect on irradiation metrics than emitter pitch. Therefore, the choice of emitter pitch could be left to the engineers dealing with challenges involving the manufacturing of the FPS. According to the results of this chapter, regardless of the choice of emitter pitch, there is a rather large flexibility in the rest of the device specifications to allow optimisation of multi-FPS device performance. Therefore, choosing the emitter pitch during the design of the FPS as a unit would not put strict limitations on the design of an integrated multi-FPS system. Also, even if the FPS dimensions end up being different than $18\times18\times13\,\mathrm{cm}^3$ or $28\times28\times13\,\mathrm{cm}^3$ or if any of the specifications in Table 6.1 change, Ipioni can be used again as explained above to find the irradiation metrics and acceptable designs metric space with the new device specifications.

The irradiation geometry metrics listed in Table 6.4 have not been tested for appropriateness against actual image quality figures of merit. Therefore, a proposed future work would be to simulate, emulate or actually acquire DT images with systems proposed by Ipioni, calculate DT image SNR, contrast, artefact spread function and other image quality metrics and see whether or not they correlate with any of the metrics used by Ipioni. If a correlation is found, then image quality as commonly defined in literature could be estimated *a priori* with Ipioni's irradiation metrics, before investing time and resources into building a multi-FPS DT system. This could drastically accelerate and reduce the cost of design and optimisation. Also, if not for a single metric, then a performance score or quality index composed of several metrics could be used to estimate the image quality of a proposed system.[96] Ipioni can then be used as explained here to calculate this score or to find the designs that maximise it and thus maximise image quality.

One of the ways that the above is now being done by the QUASAR group and Adaptix is by using Ipioni to export emitter positions, beam directions and beam sizes of acceptable designs and using them to simulate beam transport and image generation using an analytical image simulator built by Adaptix. Different phantoms are used and image quality metrics will be measured on the resulting images and they will be compared with the metrics provided by Ipioni. Also, the Geant4 model used to generate the results from Chapter 5 could be refactored to use CUDA technology so that highly detailed simulations with dosimetric and image data can be performed in large scale using graphics processing units and thousands of Ipioni-generated device specifications.

The largest limitation of Ipioni is that it does not include the physical phenomena involved in X-ray imaging. Dose to the patient and scatter are not taken into account and these are fundamental quantities that must be studied in detail and minimised for all the imaging modalities mentioned in Chapter 2, including DT. However, Monte Carlo

simulations are better suited for this type of studies. Ipioni's role is instead to first find which designs are possible to build from a geometrical point of view and identify those few that maximise some irradiation geometry metrics. Then, these few can be simulated with Monte Carlo methods as mentioned before to get detailed insights of machine performance including image quality and patient dose.

Another limitation is that Ipioni currently uses perfectly sharp cone beams whereas in reality, beam penumbra is expected. These cone beams were found to be incapable of achieving high detector coverage unless beam overlap was sacrificed or stray radiation is included. So, a useful next feature of Ipioni could be the ability to use rectangular beams or a gross collimator to reshape many cone beams into a single rectangular beam. Also, beam penumbra could be expressed as partial irradiation while the beam core would be considered full irradiation such that whether a pixel or voxel are irradiated or not could be expressed by a percentage instead of the binary way that is used at the moment with the perfectly sharp beams.

Finally, parameter scans are lengthy. Instead, Ipioni could become part of a genetic algorithm, responsible for reading device specifications, asserting the geometrical acceptance, calculating irradiation geometry metrics and then feeding those to the algorithm. The algorithm would give the design a score according to whether or not it is geometrically acceptable and according to the values of the irradiation geometry metrics. It would then generate a new set of device specifications, slightly different and according to some loss function, that it would feed to Ipioni with the goal of achieving an improved score. This process can be repeated until the design performance converges to some high level. Ipioni can be used as is for something like that by sending the irradiation metrics to the genetic algorithm instead of writing them to a file and by accepting device specifications by the algorithm instead of waiting for user input. The exchange of data between the genetic algorithm and Ipioni would happen in a loop until the process converges to a solution.

6.8 Conclusion

Ipioni is a computer application that can be used to find geometrically acceptable designs of DT imaging systems with multiple stationary FPSs and a stationary flat panel detector. It requires only a handful of input data, it can calculate a large number of metrics to score the generated designs and it can also export all the necessary information to visualise them in 3D. The data exported by Ipioni can also be used in DT image reconstruction software, in physics simulation software and ultimately for manufacturing. Using Ipioni in its current version and with the workflow described here, the code has already helped narrow down design decision trees and identify parameters that are less important than others during this early stage of developing a multi-FPS chest DT system. This is critical information and at this early stage is expected to rapidly accelerate the development of a new generation of compact and portable 3D imaging systems

by Adaptix. But further to that, the code's ability to be part of larger simulation or design optimisation frameworks raises the potential for it becoming widely used even at later, more mature stages of device development proving that Ipioni is a powerful and valuable tool for bringing a new medical imaging technology to clinics globally.

Chapter 7

Thesis summary and conclusions

Although initially superseded by CT due to the higher 3D image quality of CT compared to DT, in Chapter 1 it was shown that DT started raising interest again as a low-dose alternative to CT and as a 3D but similar dose alternative to 2D radiography. Cold-cathode field emission technology developed by Adaptix and described in Chapter 2, is a novel technology that allows the construction of stationary flat panel X-ray source arrays which emulate the different positions of a mechanically translated X-ray tube without actually needing to move the sources. The benefits of this technology include a much more compact X-ray source, shorter imaging time, lower cost than conventional X-ray tubes and the ability to irradiate the patient from planarly distributed projection angles which improves image quality compared to a linearly distributed array. Thus, 3D imaging modalities, including DT, can be performed with cheaper, lighter and portable machines and focusing on DT, this technology is expected to bring low-dose and low-cost 3D X-ray imaging to the patient's bedside.

In Chapter 3, a Monte Carlo simulation framework of the Adaptix cold-cathode flat panel source arrays was developed in two different Monte Carlo codes, namely FLUKA and Geant4, and the results were validated with experimental data. The model produced results which were practically identical between the two codes. Also, the simulated results were within an order of magnitude from the experiments in terms of photon yield and much closer in terms of energy spectrum and half value layer. Challenges with steering and focusing of the electron beam were identified as sources of error and better agreement is expected when these challenges are overcome. As such, the flat panel source model was successfully benchmarked between two fundamentally different Monte Carlo codes and validated with experimental results proving its reliability. Therefore, combined with the uniqueness of the Adaptix technology and the demonstrated benefits against conventional X-ray tubes, this simulation framework can be the foundation for further industrial and academic research as the technology is developed and gradually adopted in more clinics around the world.

Using this simulation framework, the accuracy of widely used approximations of Monte Carlo photon transport in tissues was tested in Chapter 4 against a more accurate representation of these interactions. The approximations were found to be no more

than a few percent different from the more accurate models in terms of image quality. Thus, the approximations are considered accurate enough for simulating DT procedures, paving the way for future research with well-known, general-purpose Monte Carlo codes without the need for more complex and difficult to build models.

With the accuracy of general-purpose Monte Carlo codes confirmed, a higher voltage and higher current upgrade to the Adaptix flat panel source was built in Chapter 5 using Monte Carlo methods based on the validated models from Chapter 3. The upgraded model was used to simulate end-to-end chest DT procedures with a highly realistic human phantom. The results indicated that a square array of X-ray sources at a shorter than usual source-to-image distance is capable of producing 3D images of the phantom. Also, using different voltages at a constant photon flux did not change the resulting images by more than a few percent and a reduction in effective dose was observed with lower voltage. Therefore, lower voltage cold cathode flat panel source arrays were proven to be excellent candidates for a compact and low-dose chest DT system. Moreover, the dose was found low enough to allow multiple flat panel sources on a single device, validating Adaptix's vision for a portable, low-dose chest DT system with multiple flat panel sources and superior image quality.

Finally, to address the need for a chest DT system with multiple flat panel sources, a Python application named Ipioni was developed that could automatically design such a system. In Chapter 6 it was demonstrated that the code can take a handful of geometrical device specifications and find the thousands of potential machine designs that meet them. By means of irradiation geometry metrics, each design is scored in terms of how well its X-ray beams overlap, how wide is the angular range of projections and how are these projections distributed within the angular range. Ipioni can be used to identify the designs with a high score and export many of the design characteristics that are needed to simulate them in detail with Monte Carlo or other methods, to emulate their performance in the laboratory using movable conventional X-ray sources and to ultimately manufacture them. Without Ipioni to rapidly identify candidate designs among a pool of tens of thousands, investing time and resources in Monte Carlo simulations or experiments could easily fall short of the optimum machine design and incur technical debt and financial losses. As such, the code has already helped Adaptix take informed decisions that accelerated their activities and reduced the cost of development at a very early stage. However, the code's ability to generate data necessary for physics and imaging simulations and its ability to become part of advanced genetic algorithms for design optimisation raises the potential for it to be widely used even at later, more mature stages of development and thus continuously support the delivery of cutting-edge imaging technology.

In conclusion, this thesis describes a first of its kind and comprehensive design and optimisation framework of a novel, compact and portable 3D X-ray imaging technology. The framework includes detailed physics simulations of the flat panel X-ray source array, detailed physics simulations of radiation transport inside the patient and the detector

and a computer aided design application that automatically finds thousands of multi-flat-panel source DT system designs that meet any reasonable design specifications. The framework is expandable by means of more accurate experimental results to build it upon, by means of running the detailed chest DT Monte Carlo simulation on graphics processing units on a larger scale and by means of upgrading Ipioni, the computer aided design application, with control over a wider range of specifications. Furthermore, the framework can be improved by adding more realistic representation of the device in Ipioni and by integrating Ipioni into other optimisation applications such as genetic algorithms to completely automate the search of the optimum design. Therefore, this is a simulation framework that can be used at early and mature stages of device development to offer deep insights of source performance, patient dose, image quality and integrated device specifications which can truly accelerate and bring down the cost of R&D. It has already provided critical answers to Adaptix about the status, advantages and potential of their flat panel X-ray sources and has laid the foundations for future research on a low-dose, ultra-compact and affordable X-ray imaging technology that is gradually being adopted globally and has the potential to replace the more than a century old technology of X-ray tubes.

Bibliography

[1] National Health Service. Annual Statistical Release 2020-21. *Diagnostic Imaging Dataset 2020-21 Data*, (1):6–8, Oct. 2021. URL https://www.england.nhs.uk/statistics/statistical-work-areas/diagnostic-imaging-dataset/diagnostic-imaging-dataset-2019-20-data/.

[2] R. L. Webber, R. A. Horton, D. A. Tyndall, and J. B. Ludlow. Tuned-aperture computed tomography (TACT). Theory and application for three-dimensional dento-alveolar imaging. *Dentomaxillofac. Rad.*, 26(1):53–62, Jan. 1997. doi: 10.1038/sj.dmfr.4600201.

[3] J. T. Dobbins and D. J. Godfrey. Digital x-ray tomosynthesis: current state of the art and clinical potential. *Phys. Med. Biol.*, 48(19):R65–R106, Sept. 2003. doi: 10.1088/0031-9155/48/19/r01.

[4] J. Y. Choo, K. Y. Lee, A. Yu, et al. A comparison of digital tomosynthesis and chest radiography in evaluating airway lesions using computed tomography as a reference. *Eur. Radiol.*, 26(9):3147–3154, Dec. 2015. doi: 10.1007/s00330-015-4127-z.

[5] C. Meltzer, M. Gilljam, J. Vikgren, et al. Quantification of pulmonary pathology in cystic fibrosis–comparison between digital chest tomosynthesis and computed tomography. *Radiat. Prot. Dosim.*, 195(3-4):434–442, Mar. 2021. doi: 10.1093/rpd/ncab017.

[6] K. Mermuys, F. D. Geeter, K. Bacher, et al. Digital tomosynthesis in the detection of urolithiasis: diagnostic performance and dosimetry compared with digital radiography with MDCT as the reference standard. *Am. J. Roentgenol.*, 195(1):161–167, July 2010. doi: 10.2214/ajr.09.3075.

[7] Y. Yamada, M. Jinzaki, M. Hashimoto, et al. Tomosynthesis for the early detection of pulmonary emphysema: diagnostic performance compared with chest radiography, using multidetector computed tomography as reference. *Eur. Radiol.*, 23(8):2118–2126, Mar. 2013. doi: 10.1007/s00330-013-2814-1.

[8] M. Held, F. Cremers, P. K. Sneed, et al. Assessment of image quality and dose calculation accuracy on kV CBCT, MV CBCT, and MV CT images for urgent palliative radiotherapy treatments. *Journal of Applied Clinical Medical Physics*, 17(2):279–290, Mar. 2016. doi: 10.1120/jacmp.v17i2.6040.

[9] J. Vikgren, S. Zachrisson, A. Svalkvist, et al. Comparison of chest tomosynthesis and chest radiography for detection of pulmonary nodules: human observer study of clinical cases. *Radiology*, 249(3):1034–1041, Dec. 2008. doi: 10.1148/radiol.2492080304.

[10] E. Quaia, E. Baratella, S. Cernic, et al. Analysis of the impact of digital tomosynthesis on the radiological investigation of patients with suspected pulmonary lesions on chest radiography. *Eur. Radiol.*, 22(9):1912–1922, Apr. 2012. doi: 10.1007/s00330-012-2440-3.

[11] J. Cant, A. Snoeckx, G. Behiels, et al. Can portable tomosynthesis improve the diagnostic value of bedside chest x-ray in the intensive care unit? A proof of concept study. *European Radiology Experimental*, 1(1), Oct. 2017. doi: 10.1186/s41747-017-0021-6.

[12] G. Travish, F. J. Rangel, M. A. Evans, et al. Addressable flat-panel x-ray sources for medical, security, and industrial applications. In S. Goto, C. Morawe, and A. M. Khounsary, editors, *Proc. SPIE*, Oct. 2012. doi: 10.1117/12.929354.

[13] Adaptix Ltd. URL `https://www.adaptix.com`. Accessed 20 February 2022.

[14] J. Bushberg. *The essential physics of medical imaging*. Wolters Kluwer Health/Lippincott Williams & Wilkins, Philadelphia, 2012. ISBN 9780781780575.

[15] S. T. Ratliff. Webb's physics of medical imaging, second edition. *Medical Physics*, 40(9):097301, aug 2013. doi: 10.1118/1.4818282.

[16] *Diagnostic radiology physics*. International Atomic Energy Agency, Nov. 2014. ISBN 9201310102. URL `https://www.ebook.de/de/product/20622679/diagnostic_radiology_physics.html`.

[17] K. S. Livingston, E. A. Edwards, M. Griffin, et al. Use of digital tomosynthesis in assessing accurate medial epicondyle fracture displacement as compared with conventional radiography and computed tomography. *J. Pediatr. Orthoped.*, 41 (10):e877–e883, aug 2021. doi: 10.1097/bpo.0000000000001917.

[18] G. Bachar, J. H. Siewerdsen, M. J. Daly, et al. Image quality and localization accuracy in C-arm tomosynthesis-guided head and neck surgery. *Med. Phys.*, 34 (12):4664–4677, Nov. 2007. doi: 10.1118/1.2799492.

[19] M. Jehangir, C. Mallory, and J. R. Medverd. Digital tomosynthesis for detection of ingested foreign objects in the emergency department: a case of razor blade ingestion. *Emergency Radiology*, 26(2):249–252, Jan. 2019. doi: 10.1007/s10140-018-01664-x.

[20] T. Omori, S. Nakamura, and K. Shiratori. Localization of the patency capsule by abdominal tomosynthesis. *Digestion*, 91(4):318–325, 2015. doi: 10.1159/000381471.

[21] E. R. Heitzman. Thoracic radiology: The past 50 years. *Radiology*, 214(2):309–313, Feb. 2000. doi: 10.1148/radiology.214.2.r00fe53309.

[22] E. M. Nelson, S. M. Monazzam, K. D. Kim, et al. Intraoperative fluoroscopy, portable X-ray, and CT: patient and operating room personnel radiation exposure in spinal surgery. *The Spine Journal*, 14(12):2985–2991, Dec. 2014. doi: 10.1016/j.spinee.2014.06.003.

[23] Carestream. URL https://www.carestream.com/. Accessed 1st of March 2022.

[24] GE Healthcare. URL https://www.gehealthcare.co.uk/. Accessed 1st of March 2022.

[25] C. Inscoe. *Stationary digital tomosynthesis: implementation, characterization, and image processing techniques*. phdthesis, University of North Carolina, Chapel Hill, 2018.

[26] A. Nitrosi, M. Bertolini, A. Chendi, et al. Physical characterization of a novel wireless DRX Plus 3543C using both a carbon nano tube (CNT) mobile x-ray system and a traditional x-ray system. *Physics in Medicine & Biology*, 65(11): 11NT02, June 2020. doi: 10.1088/1361-6560/ab8afb.

[27] M. Alhrishy, A. Varnavas, T. Carrell, et al. Interventional digital tomosynthesis from a standard fluoroscopy system using 2D-3D registration. *Med. Image Anal.*, 19(1):137–148, Jan. 2015. doi: 10.1016/j.media.2014.10.001.

[28] S. S. Hsieh and L. W. Ng. Real-time tomosynthesis for radiation therapy guidance. *Med. Phys.*, 44(11):5584–5595, Sept. 2017. doi: 10.1002/mp.12530.

[29] K. P. Orcutt, B. Libby, L. L. Handsfield, et al. CT-on-rails-guided HDR brachytherapy: single-room, rapid-workflow treatment delivery with integrated image guidance. *Future Oncol.*, 10(4):569–575, Mar. 2014. doi: 10.2217/fon.13.239.

[30] C. Papalazarou, G. J. Klop, M. T. W. Milder, et al. CyberKnife with integrated CT-on-rails: System description and first clinical application for pancreas SBRT. 44(9):4816–4827, Aug. 2017. doi: 10.1002/mp.12432.

[31] A. W. Tucker, J. Lu, and O. Zhou. Dependency of image quality on system configuration parameters in a stationary digital breast tomosynthesis system. *Med. Phys.*, 40(3):031917, Mar. 2013. doi: 10.1118/1.4792296.

[32] S. Wells, P. Elangovan, D. R. Dance, et al. Modelling the use of stationary, rectangular arrays of x-ray emitters for digital breast tomosynthesis. In H. Bosmans and G.-H. Chen, editors, *Medical Imaging 2020: Physics of Medical Imaging*. SPIE, Mar. 2020. doi: 10.1117/12.2548438.

[33] L. Bertolaccini, A. Viti, C. Tavella, et al. Lung cancer detection with digital chest tomosynthesis: first round results from the SOS observational study. *Annals of Translational Medicine*, 3(5), 2015. doi: 10.3978/j.issn.2305-5839.2015.03.41.

[34] A. D. A. Maidment. Commentary on "Whole-body clinical applications of digital tomosynthesis," with response from Dr Machida and colleagues. *RadioGraphics*, 36 (3):750–752, May 2016. doi: 10.1148/rg.2016160028.

[35] S.-H. S. Chou, G. A. Kicska, S. N. Pipavath, and G. P. Reddy. Digital tomosynthesis of the chest: current and emerging applications. *RadioGraphics*, 34(2):359–372, Mar. 2014. doi: 10.1148/rg.342135057.

[36] S. Tongkum, P. Suwanpradit, S. Vidhyarkorn, et al. Determination of radiation dose and low-dose protocol for digital chest tomosynthesis using radiophotoluminescent (RPL) glass dosimeters. *Phys. Medica*, 73:13–21, May 2020. doi: 10.1016/j.ejmp.2020.03.024.

[37] K. Sato, T. Ohnishi, M. Sekine, and H. Haneishi. Geometry calibration between X-ray source and detector for tomosynthesis with a portable X-ray system. *Int. J. Comput. Ass. Rad.*, 12(5):707–717, Mar. 2017. doi: 10.1007/s11548-017-1557-x.

[38] J. M. Sabol. A Monte Carlo estimation of effective dose in chest tomosynthesis. *Med. Phys.*, 36(12):5480–5487, Nov. 2009. doi: 10.1118/1.3250907.

[39] X. Qian, A. Tucker, E. Gidcumb, et al. High resolution stationary digital breast tomosynthesis using distributed carbon nanotube x-ray source array. *Med. Phys.*, 39(4):2090–2099, Mar. 2012. doi: 10.1118/1.3694667.

[40] J. Shan, A. W. Tucker, Y. Z. Lee, et al. Stationary chest tomosynthesis using a carbon nanotube x-ray source array: a feasibility study. *Phys. Med. Biol.*, 60(1): 81–100, Dec. 2014. doi: 10.1088/0031-9155/60/1/81.

[41] C. R. Inscoe, E. Platin, S. M. Mauriello, et al. Characterization and preliminary imaging evaluation of a clinical prototype stationary intraoral tomosynthesis system. *Med. Phys.*, 45(11):5172–5185, Oct. 2018. doi: 10.1002/mp.13214.

[42] C. Söderman, S. Asplund, Å. A. Johnsson, et al. Image quality dependency on system configuration and tube voltage in chest tomosynthesis-A visual grading study using an anthropomorphic chest phantom. *Med. Phys.*, 42(3):1200–1212, Feb. 2015. doi: 10.1118/1.4907963.

[43] T. G. Primidis, S. G. Wells, V. Y. Soloviev, and C. P. Welsch. 3D chest tomosynthesis using a stationary flat panel source array and a stationary detector: a Monte Carlo proof of concept. *Biomed. Phys. Eng. Express*, 8(1):015006, Nov. 2021. doi: 10.1088/2057-1976/ac3880.

[44] GE VolumeRAD™Digital Tomosynthesis. URL https://www.gehealthcare.co.uk/products/radiography-systems/advanced-applications/volumerad. Accessed 14 May 2021.

[45] C. Söderman, Å. A. Johnsson, J. Vikgren, et al. Detection of pulmonary nodule growth with chest tomosynthesis: a human observer study using simulated nodules. *Acad. Radiol.*, 26(4):508–518, Apr. 2019. doi: 10.1016/j.acra.2018.05.004.

[46] Canon Medical Components U.S.A. CXDI-50RF digital radiography system. URL https://mcu.canon/internet/portal/vi/home/products/details/digital-radiography-fluoroscopy/digital-detectors/cxdi-50rf/cxdi-50rf-digital-radiography-system. Accessed 14 May 2021.

[47] I. Sechopoulos and C. Ghetti. Optimization of the acquisition geometry in digital tomosynthesis of the breast. *Med. Phys.*, 36(4):1199–1207, Mar. 2009. doi: 10.1118/1.3090889.

[48] H. Machida, T. Yuhara, M. Tamura, et al. Whole-body clinical applications of digital tomosynthesis. *RadioGraphics*, 36(3):735–750, May 2016. doi: 10.1148/rg.2016150184.

[49] A. Galea, A. Durran, T. Adlan, et al. Practical applications of digital tomosynthesis of the chest. *Clin. Radiol.*, 69(4):424–430, Apr. 2014. doi: 10.1016/j.crad.2013.10.019.

[50] M. Geijer, E. Gunnlaugsson, S. Götestrand, et al. Tomosynthesis of the thoracic spine: added value in diagnosing vertebral fractures in the elderly. *Eur. Radiol.*, 27 (2):491–497, May 2016. doi: 10.1007/s00330-016-4392-5.

[51] A. W. Tucker, J. Calliste, E. M. Gidcumb, et al. Comparison of a stationary digital breast tomosynthesis system to magnified 2d mammography using breast tissue specimens. *Acad. Radiol.*, 21(12):1547–1552, Dec. 2014. doi: 10.1016/j.acra.2014.07.009.

[52] Y. Z. Lee, C. Puett, C. R. Inscoe, et al. Initial clinical experience with stationary digital breast tomosynthesis. *Acad. Radiol.*, 26(10):1363–1372, Oct. 2019. doi: 10.1016/j.acra.2018.12.026.

[53] C. Puett, J. Gao, A. Tucker, et al. Visualizing microcalcifications in lumpectomy specimens: an exploration into the clinical potential of carbon nanotube-enabled stationary digital breast tomosynthesis. *Biomed. Phys. Eng. Express*, 5(4):045040, July 2019. doi: 10.1088/2057-1976/ab3320.

[54] G. Lee, Y. J. Jeong, K. I. Kim, et al. Comparison of chest digital tomosynthesis and chest radiography for detection of asbestos-related pleuropulmonary disease. *Clin. Radiol.*, 68(4):376–382, Apr. 2013. doi: 10.1016/j.crad.2012.05.022.

[55] A. Galea, P. Dubbins, R. Riordan, et al. The value of digital tomosynthesis of the chest as a problem-solving tool for suspected pulmonary nodules and hilar lesions detected on chest radiography. *Eur. J. Radiol.*, 84(5):1012–1018, May 2015. doi: 10.1016/j.ejrad.2015.02.007.

[56] S. G. Langer, B. D. Graner, B. A. Schueler, et al. Sensitivity of thoracic digital tomosynthesis (DTS) for the identification of lung nodules. *J. Digit. Imaging*, 29 (1):141–147, Sept. 2015. doi: 10.1007/s10278-015-9818-0.

[57] C.-N. Son, Y. Song, S.-H. Kim, et al. Digital tomosynthesis as a new diagnostic tool for assessing of chronic gout arthritic feet and ankles: comparison of plain radiography and computed tomography. *Clin. Rheumatol.*, 36(9):2095–2100, June 2017. doi: 10.1007/s10067-017-3710-x.

[58] Y. H. Roh, S. Lee, J. A. Ryu, et al. Digital tomosynthesis versus conventional radiography for evaluating osteonecrosis of the femoral head. *Korean J. Radiol.*, 22 (12):2026, 2021. doi: 10.3348/kjr.2021.0058.

[59] A. Fassò, A. Ferrari, J. Ranft, and P. R. Sala. Fluka: A multi-particle transport code (program version 2005), 2005.

[60] S. Agostinelli, J. Allison, K. Amako, et al. Geant4—a simulation toolkit. *Nucl. Instrum. Meth. A*, 506(3):250–303, July 2003. doi: 10.1016/s0168-9002(03)01368-8.

[61] V. Y. Soloviev, K. L. Renforth, C. J. Dirckx, and S. G. Wells. Meshless reconstruction technique for digital tomosynthesis. *Phys. Med. Biol.*, 65(8):085010, Apr. 2020. doi: 10.1088/1361-6560/ab7685.

[62] D. Kim, D. W. Kim, J. Yun, et al. Spatial resolution and blurring artifacts in digital X-ray tomosynthesis. *IEEE Transactions on Nuclear Science*, 65(5):1180–1186, May 2018. doi: 10.1109/tns.2018.2820744.

[63] T. Primidis, V. Soloviev, and C. P. Welsch. FLUKA and Geant4 Monte Carlo simulations of a desktop, flat panel source array for 3D medical imaging. In *Proc. IPAC'21*, pages 2483–2486. JACoW Publishing, Geneva, Switzerland, Aug. 2021. ISBN 978-3-95450-214-1. doi: 10.18429/JACoW-IPAC2021-TUPAB409.

[64] V. Vlachoudis. FLAIR: a powerful but user friendly graphical interface for FLUKA. In *Proc. Int. Conf. on Mathematics, Computational Methods & Reactor Physics (M&C 2009), Saratoga Springs, New York*, volume 176, 2009.

[65] Epoxy composition. URL `https://www.phenix.bnl.gov/~suhanov/ncc/geant/rad-source/src/ExN03DetectorConstruction.cc`. Accessed 14 May 2021.

[66] F. Salvat, M. Fernandez-Varea, J., E. Acosta, and J. Sempau. *PENELOPE 2018: A code system for Monte Carlo simulation of electron and photon transport*. OECD, Sept. 2019. doi: 10.1787/32da5043-en.

[67] RTI Group. URL https://rtigroup.com. Accessed 14 May 2021.

[68] Radcal. URL https://radcal.com. Accessed 14 May 2021.

[69] AMPTEK. URL https://www.amptek.com. Accessed 14 May 2021.

[70] A. H. Narten and H. A. Levy. Liquid water: molecular correlation functions from x-ray diffraction. *J. Chem. Phys.*, 55(5):2263–2269, Sept. 1971. doi: 10.1063/1.1676403.

[71] M. E. Poletti, O. D. Gonçalves, and I. Mazzaro. X-ray scattering from human breast tissues and breast-equivalent materials. *Phys. Med. Biol.*, 47(1):47–63, Nov. 2001. doi: 10.1088/0031-9155/47/1/304.

[72] D. E. Peplow and K. Verghese. Measured molecular coherent scattering form factors of animal tissues, plastics and human breast tissue. *Phys. Med. Biol.*, 43(9):2431–2452, Sept. 1998. doi: 10.1088/0031-9155/43/9/001.

[73] G. Paternò, P. Cardarelli, M. Gambaccini, and A. Taibi. Comprehensive data set to include interference effects in Monte Carlo models of x-ray coherent scattering inside biological tissues. *Phys. Med. Biol.*, 65(24):245002, Dec. 2020. doi: 10.1088/1361-6560/aba7d2.

[74] A. Tartari, A. Taibi, C. Bonifazzi, and C. Baraldi. Updating of form factor tabulations for coherent scattering of photons in tissues. *Phys. Med. Biol.*, 47(1):163–175, Dec. 2001. doi: 10.1088/0031-9155/47/1/312.

[75] G. Poludniowski, P. M. Evans, and S. Webb. Rayleigh scatter in kilovoltage x-ray imaging: is the independent atom approximation good enough? *Phys. Med. Biol.*, 54(22):6931–6942, Nov. 2009. doi: 10.1088/0031-9155/54/22/012.

[76] T. G. Primidis, V. Y. Soloviev, and C. P. Welsch. Accuracy of the independent atom approximation in digital tomosynthesis Monte Carlo simulations. *Biomed. Phys. Eng. Express*, 7(5):055016, Aug. 2021. doi: 10.1088/2057-1976/ac1987.

[77] ICRP, 2010. *Conversion coefficients for radiological protection quantities for external radiation exposures. ICRP Publication 116*, volume Ann. ICRP 40(2-5). ISBN 9781455728589.

[78] G. J. Royle and R. D. Speller. Quantitative X-ray diffraction analysis of bone and marrow volumes in excised femoral head samples. *Phys. Med. Biol.*, 40(9):1487–1498, Sept. 1995. doi: 10.1088/0031-9155/40/9/008.

[79] B. W. King, K. A. Landheer, and P. C. Johns. X-ray coherent scattering form factors of tissues, water and plastics using energy dispersion. *Phys. Med. Biol.*, 56(14):4377–4397, June 2011. doi: 10.1088/0031-9155/56/14/010.

[80] D. R. White. Tissue substitutes in experimental radiation physics. *Med. Phys.*, 5 (6):467–479, Nov. 1978. doi: 10.1118/1.594456.

[81] G. Paternò, P. Cardarelli, A. Contillo, et al. Geant4 implementation of inter-atomic interference effect in small-angle coherent X-ray scattering for materials of medical interest. *Phys. Medica*, 51:64–70, July 2018. doi: 10.1016/j.ejmp.2018.04.395.

[82] R. H. T. Bates and T. M. Peters. Towards improvements in tomography. *New Zealand J. Sci.*, 14:883–896, 1971.

[83] H. W. Engl, M. Hanke, and A. Neubauer. *Regularization of inverse problems.* Springer Netherlands, 1996. ISBN 0792341570. URL https://www.ebook.de/de/product/4046405/heinz_werner_engl_martin_hanke_a_neubauer_regularization_of_inverse_problems.html.

[84] FreeCAD (Version 0.19.2) [Computer Software]. URL https://freecadweb.org/.

[85] ICRP, 2020. *Adult mesh-type reference computational phantoms. ICRP Publication 145*, volume Ann. ICRP 49(3). ISBN 9781529742213.

[86] M. Bath, A. Svalkvist, A. von Wrangel, et al. Effective dose to patients from chest examinations with tomosynthesis. *Radiat. Prot. Dosim.*, 139(1-3):153–158, Mar. 2010. doi: 10.1093/rpd/ncq092.

[87] ICRP, 2007. *The 2007 recommendations of the International Commission on Radiological Protection. ICRP Publication 103*, volume Ann. ICRP 37(2-4). ISBN 9780702030482.

[88] ICRP, 2002. *Basic anatomical and physiological data for use in radiological protection: Reference Values. ICRP Publication 89*, volume Ann. ICRP 32(3/4). ISBN 0080442668.

[89] U.S. Food & Drug Administration. *21 CFR 1020 - Performance standards for ionizing radiation emitting products.* 2020. URL https://www.govinfo.gov/app/details/CFR-2011-title21-vol8/CFR-2011-title21-vol8-part1020/summary.

[90] European Commission. Directorate General for Energy. *Criteria for acceptability of medical radiological equipment used in diagnostic radiology, nuclear medicine and radiotherapy.* Publications Office, 2012. doi: 10.2768/22561.

[91] Y. Zhang, X. Li, W. P. Segars, and E. Samei. Comparison of patient specific dose metrics between chest radiography, tomosynthesis, and CT for adult patients of wide ranging body habitus. *Med. Phys.*, 41(2):023901, Jan. 2014. doi: 10.1118/1.4859315.

[92] T. Primidis, V. Soloviev, S. Wells, and C. Welsch. Design and optimisation of a stationary chest tomosynthesis system with multiple flat panel field emitter arrays: Monte Carlo simulations and computer aided designs. In *Proc. IPAC'22*,

pages 3034–3037. JACoW Publishing, Geneva, Switzerland, June 2022. doi: 10.18429/JACOW-IPAC2022-THPOMS033.

[93] H. Machida, T. Yuhara, T. Mori, et al. Optimizing parameters for flat-panel detector digital tomosynthesis. *RadioGraphics*, 30(2):549–562, Mar. 2010. doi: 10.1148/rg.302095097.

[94] G. Voronoi. Nouvelles applications des paramètres continus à la théorie des formes quadratiques. premier mémoire. sur quelques propriétés des formes quadratiques positives parfaites. *Journal für die reine und angewandte Mathematik (Crelles Journal)*, 1908(133):97–102, Jan. 1908. doi: 10.1515/crll.1908.133.97.

[95] G. Voronoi. Nouvelles applications des paramètres continus à la théorie des formes quadratiques. deuxième mémoire. recherches sur les paralléllo̊edres primitifs. *Journal für die reine und angewandte Mathematik (Crelles Journal)*, 1908(134):198–287, July 1908. doi: 10.1515/crll.1908.134.198.

[96] K. V. von Steyern, I. M. Björkman-Burtscher, P. Höglund, et al. Description and validation of a scoring system for tomosynthesis in pulmonary cystic fibrosis. *Eur. Radiol.*, 22(12):2718–2728, June 2012. doi: 10.1007/s00330-012-2534-y.